Carnegie Mellon

Department of Physics
Carnegie Mellon University
Pittsburgh, Pennsylvania 15213-3890

A Search for the $\xi(2230)$ Resonance in the $\bar{p}\,p \rightarrow K_S K_S$ channel at LEAR.

by

Jean Seydoux

A dissertation submitted in partial fulfillment
of the requirements for the degree of

Doctor of Philosophy
in the
Department of Physics
Carnegie Mellon University
Pittsburgh, Pennsylvania

February, 1990

A Search for the $\xi(2230)$ Resonance in the $\bar{p}\,p \rightarrow K_S K_S$ channel at LEAR.

DOE/ER/40315--173

DE90 010126

by

Jean Seydoux

A dissertation submitted in partial fulfillment
of the requirements for the degree of

Doctor of Philosophy
in the
Department of Physics
Carnegie Mellon University
Pittsburgh, Pennsylvania

February, 1990

Abstract

Seventeen measurements of differential and total cross sections of the $\bar{p}\,p \rightarrow K_S K_S$ reaction in the antiproton momentum range of 1.30 GeV/c to 1.57 GeV/c are presented. Most of these measurements are centered around the mass of the $\xi(2230)$ resonance first seen in the K^+K^- and $K_S K_S$ channel of the radiative decay of the J/ψ by the MARK III collaboration at SLAC. The trajectories of the charged decay products of the K_S particles are recorded by two stacks of drift chambers and a set of plastic streamer tube planes. The $\bar{p}\,p \rightarrow K_S K_S \rightarrow \pi^+\pi^-\,\pi^+\pi^-$ events are reconstructed by a computer program and undergo a full kinematic fitting. A branching ratio upper limit, $BR(\bar{p}p \rightarrow \xi) \cdot BR(\xi \rightarrow K_S K_S)$, on the presence of the resonance is calculated. The experiment was performed by the PS185 collaboration at the Low Energy Antiproton Ring (LEAR) at CERN.

PS185 Collaboration

P. D. Barnes, G. Diebold, G. Franklin, C. Maher, B. Quinn,
J. Seydoux, J. Szymanski, X. Yi.
Carnegie Mellon University.

W. Eyrich, R. v. Frankenberg, A. Hoffmann, M. Meyerhofer,
H. Ortner, F. Stinzing.
University of Erlangen

P. Birien, W. Dutty, J. Franz, N. Hamann, G. Harig,
E. Rössle, H. Schledermann, H. Schmitt.
University of Freiburg

E. Eisenstein, D. Hertzog.
University of Illinois

K.Kilian, W. Oelert, G. Sehl, T. Zeludziewicz.
Juelich KFA.

B. Bonner
Rice University

G. Ericsson, T. Johansson, S. Ohlsson.
Uppsala University

W. Breunlich, N. Naegele, P. Pawlek.
Osterr. Akad. Wissensch. Vienna

Table of Contents

I. Physics Motivation and Theory.

I.A. Introduction.

The discovery of the Mendeleev periodic table of elements was the first quantitative attempt at establishing the fundamental structure of matter. The proliferation of elements and the apparent systematics in the organization of the table suggested that a substructure was present.

The experimental effort in the first part of this century lead to the discovery of the proton and neutron (nucleon) which are held together by the nuclear force (strong force) to form nuclei. These particles are then bound with electrons through the electromagnetic force to produce the atoms of the chemical elements. The conversion of neutrons into protons by the weak force explains the radioactive β-decay of nuclei and the presence of antineutrinos. Unfortunately, the proton and neutron are only the lightest elements of a spectrum of more than one hundred strongly interacting fermion states ($p,n,\Lambda,\Sigma,\Xi,..$), called baryons. Likewise, an equal amount of strongly interacting bosons ($\pi,\rho,K,\omega,\eta,..$), called mesons, has also been discovered. The baryons and mesons are collectively called hadrons and differ from each other by the value of their spin (half integer and integer spin).

Like the periodic table of elements, the multiplicity of elementary hadrons hinted towards another substructure. The sequence of important discoveries in the past two decades firmly established the current building blocks of matter as shown in Table.I.A.1. Hadrons are not the elementary building block of matter; they join nuclei and atoms as one more manifestation of bound-state structures that exist in a world made of QUARKS and LEPTONS. The baryons are bound states of three quarks while the mesons are composed of a quark antiquark pair. Three generations of quark pairs are necessary to explain all the known hadron spectra. The lowest group of spin 1/2 baryons and spin 0 mesons are shown in Fig.I.A.1 with their corresponding quark configurations. The electron and neutrino are the lightest elements of a group of particles known as leptons. The number of leptons has not multiplied as the hadrons have and are still considered elementary point like particles.

The fundamental forces are then explained by the exchange of gauge bosons such as the photon, weak bosons and gluons among these elementary particles.

The electromagnetic force is characterized by the exchange of a massless photon between charged particles and is quantitatively described by the theory of electromagnetic interactions of charged particles and photons (QED).

The massive weak bosons such as the $W^{\pm}$ and the Z particles give the very short range effect of the weak interaction and when combined with the photon allows the unification of two fundamental forces, the electromagnetic and weak forces, in a model known as the electroweak theory.

Finally, in analogy with the electromagnetic theory, the theory of the strong force known as quantum chromodynamic (QCD) describes the exchange of gluons between quarks. A new charge called color is the source of the strong force between quarks, just as the electric charge acts as the source of the electromagnetic force between electrically charged particles. As the quarks carry both color and electric charges, they experience both the strong and electromagnetic forces, as well as the weak interaction. However, the color force is more complicated and requires three different color charges among which the force

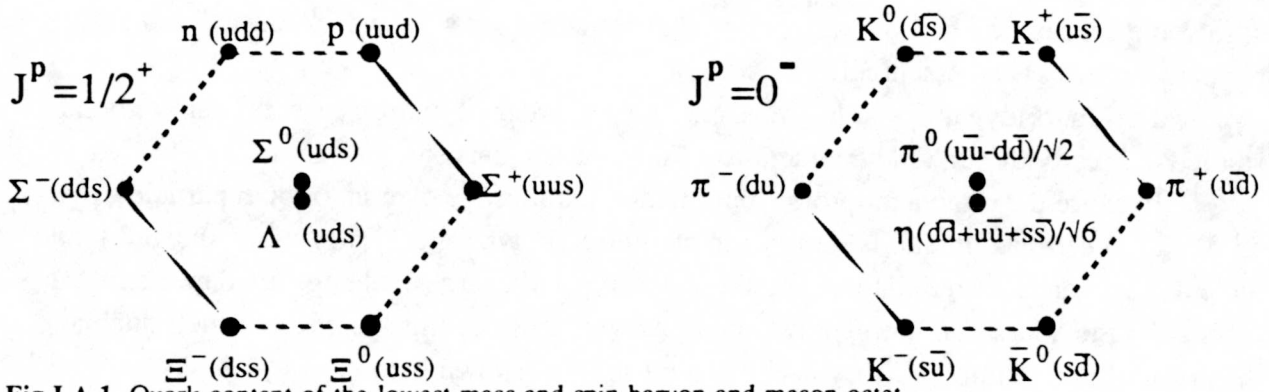

Fig.I.A.1. Quark content of the lowest mass and spin baryon and meson octet.

Table.I.A.1.

Building Blocks of Matter										
Name							Spin **S**	Baryon number **B**	Lepton number **L**	Charge **Q**
Quarks	u	(up)	c	(charm)	t	(top)	1/2	1/3	0	+2/3
	d	(down)	s	(strange)	b	(bottom)	1/2	1/3	0	-1/3
Leptons	e	(electron)	μ	(muon)	τ	(tau)	1/2	0	1	-1
	ν_e	(neutrino)	ν_μ	(neutrino)	ν_τ	(neutrino)	1/2	0	1	0
Gauge bosons	γ	(photon)					1	0	0	0
	$W^{\pm}$,Z (weak bosons)						1	0	0	±1,0
	g_i (i=1,...,8 gluons)						1	0	0	0

must always be attractive at large distance. QCD does not enjoy the same quantitative success as QED. Because the strength of the quark and gluon coupling increases at large distance (low energy), perturbative techniques, as used in QED, prove to be very difficult to apply to QCD calculations at low energy. The study of quark and gluon dynamics at low energies is therefore necessary to understand the strong force better and is currently the object of an important theoretical and experimental effort.

I.B. $\bar{p}\,p \rightarrow \bar{M}\,M$ Studies.

No free quarks have been experimentally observed. This fact is a direct consequence of the increase of the strong force between quarks at large distance. All observed hadrons are color "singlets" or in other words the three color charges must be equally present in all hadrons. By keeping the "free" quarks confined in a "bag" volume roughly of the hadron size, the MIT bag model and its derivatives have been able to predict with some success the hadron masses and magnetic moments. However, these models are phenomenological and essentially static.

The quark dynamics at low energies (of the order of hadron masses) can only be studied indirectly through the interactions of mesons and baryons.

Because the proton antiproton annihilation requires the overlap of both particles, $\bar{p}\,p$ annihilation offers a unique laboratory to study quark dynamics. Early work showed that the cross sections for annihilation, elastic scattering, and charge exchange are dependent on the size of the quark confinement region. However, by selecting specific channels such as the $\bar{p}p$ annihilation into two baryons or two mesons, as shown below,

$$\bar{p}\,p \rightarrow \bar{B}\,B \qquad \text{where } B = (\,p,\, n,\, \Lambda,\, \Sigma..)$$
$$\bar{p}\,p \rightarrow \bar{M}\,M \qquad \text{where } M = (\,\pi,\, K,\, \rho,\, \phi..)$$

the annihilation rates are more likely to be dependent on the reaction dynamics and quark confinement properties. These channels are numerous at low energy because, through the particle antiparticle annihilation, more center of mass energy is available allowing a large number of reaction channels to be open. Also, these channels have the simplicity of the two body kinematics and make explicit model calculations easier.

In the case of the basic $\bar{p}\,p \rightarrow \bar{M}\,M$ process introduced above, a set of selection rules can be established from the parity and charge conjugation conservation. In Table.I.B.1 are listed all the possible low angular momentum $\bar{p}\,p$ states. The selection rules for the $\bar{p}\,p \rightarrow \bar{M}\,M$ reactions are shown in Table.I.B.2. Two important conclusions can be discussed.

First, the $\bar{p}\,p$ initial state can only be in a spin triplet state because of parity conservation, with the parity of the boson pair defined as $(-1)^J$, $L_{\bar{p}p} = J\pm1$. Therefore, the $\bar{p}\,p$ annihilation can not proceed through the $^1S_0$ state to produce kaon and pion pairs but this state can yield 5π or 3π states. The absence of the centrifugal barrier for the $^1S_0$ states will then account for the dominance of these odd π final states in the $\bar{p}\,p$ annihilation.

Table.I.B.1.

Possible $\bar{p}$ p States		$^{2I+1,2S+1}L_J$ PCG		
		J=0	J=1	J=2
I=0	S=0	$^{1,1}S_0$ $^{-++}$	$^{1,1}P_1$ $^{+--}$	$^{1,1}D_2$ $^{-++}$
	S=1	$^{1,3}P_0$ $^{+++}$	$^{1,3}S_1$ $^{---}$ $^{1,3}P_1$ $^{+++}$ $^{1,3}D_1$ $^{---}$	$^{1,3}P_2$ $^{+++}$ $^{1,3}D_2$ $^{---}$ $^{1,3}F_2$ $^{+++}$
I=1	S=0	$^{3,1}S_0$ $^{-+-}$	$^{3,1}P_1$ $^{+-+}$	$^{3,1}D_2$ $^{-+-}$
	S=1	$^{3,3}P_0$ $^{++-}$	$^{3,3}S_1$ $^{--+}$ $^{3,3}P_1$ $^{++-}$ $^{1,3}D_1$ $^{--+}$	$^{3,3}P_2$ $^{++-}$ $^{3,3}D_2$ $^{--+}$ $^{3,3}F_2$ $^{++-}$
$P = (-1)^{L+1}$		$C = (-1)^{L+S}$	$G = (-1)^{L+S+I}$	$CP = (-1)^{S+1}$

Table.I.B.2.

Selection Rules for $\bar{p}\,p \rightarrow \bar{M}\,M$				
$\bar{p}$ p states (I=0,1) $^{2S+1}L_J$ ($^3P_0$, $^3S_1$, $^3D_1$, $^3P_2$, $^3F_2$...)				
$\pi^0\,\pi^0$	$\pi^-\,\pi^+$	$K^-\,K^+$	$K_S\,K_L$	$K_S\,K_S$,$K_L\,K_L$
Even J , I=0	Even J, I=0 Odd J, I=1	Even J, I=0,1 Odd J, I=0,1	Odd J, I=0,1	Even J, I=0,1

Secondly, because of CP conservation, the production of K_SK_S and K_LK_L pairs can only take place with even angular momenta and positive parity. The K_S and K_L defined below as

$$K_S = \frac{1}{\sqrt{2}} \left(\mid K^0 > \; - \mid \bar{K}^0 > \right)$$

$$K_L = \frac{1}{\sqrt{2}} \left(\mid K^0 > \; + \mid \bar{K}^0 > \right)$$

are CP eigenstates and therefore the K_SK_S and K_LK_L pairs are also CP eigenstates with eigenvalues of $(-1)^{L=J}$. These eigenvalues must then be compared with those from the $\bar{p}$ p system in a spin triplet states whose CP eigenvalue is +1. This selection rule is important for the determination of the possible spin of the ξ resonance under investigation in this thesis if this resonance is seen in the $\bar{p}$ p $\rightarrow$ K_SK_S channel .

The $\bar{p}$ p $\rightarrow$ $\bar{M}$ M calculations can be described either by the conventional baryon exchange model or directly by quark antiquark annihilation and rearrangement models. In both cases, initial and final state interactions must be taken into account in order to get reasonable quantitative results.

In the baryon exchange model, a p,n,Λ or Σ is exchanged between the proton and antiproton with the direct emission of the meson antimeson pair, as seen in Fig.I.B.1a. This model was first applied by Moussallam[I.MOUSSALAM.83] and seems to give an acceptable account of the limited amount of experimental data, especially for the $\pi^+\pi^-$ channel. This calculation, however, suffers from the uncertainty in the knowledge of meson-baryon coupling constants, a common problem in baryon exchange model calculations.

In the calculation of Girija and Tabakin[I.GIRIJA.86], antiproton proton annihilation leading to K^+K^-, K_SK_S, and K_SK_L is analysed using the baryon exchange model with a Λ and Σ exchange. The initial state interaction is constrained to fit the $\bar{p}$ p elastic scattering data, while the $\bar{K}K$ final state interaction (strength and range) is varied to fit the $\bar{p}$ p $\rightarrow$ K^+K^- data. In order to have satisfactory agreement with the differential cross section data for the K^+K^- production, resonances such as the ξ, ρ, and ϵ had also to be included. The K_SK_S and K_SK_L cross sections are then predicted. This is the only available calculation pertaining to the $\bar{p}$ p $\rightarrow$ K_SK_S reaction under investigation in this thesis.

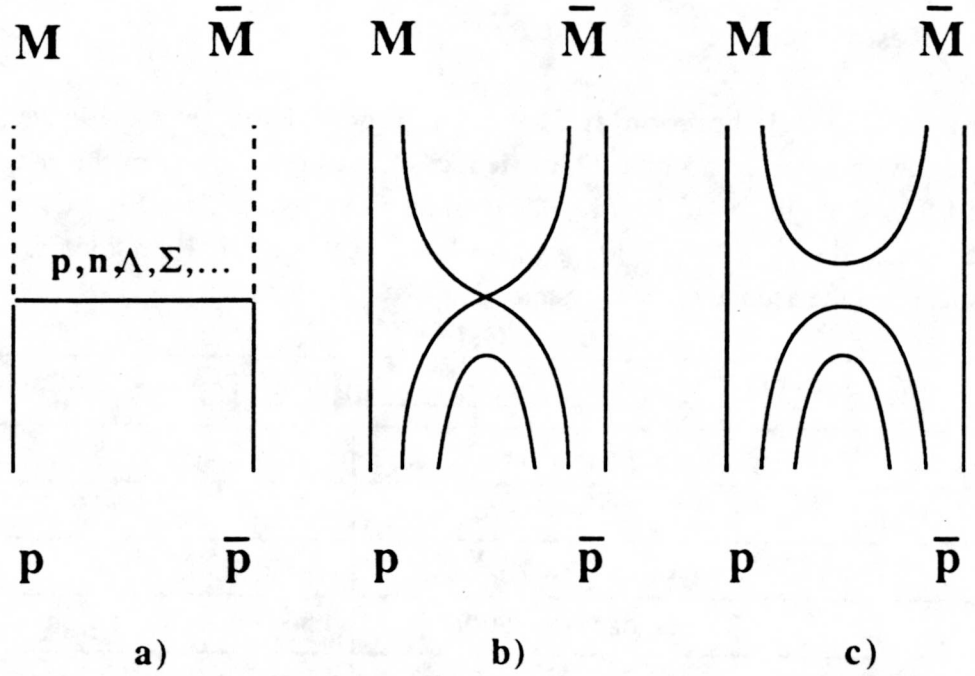

Fig.I.B.1. $\bar{p}$ p annihilation into two meson via a) nucleon exchange, b) annihilation of a single $\bar{q}$ q pair and rearrangement, c) two $\bar{q}$ q annihilations and a single $\bar{q}$ q creation.

In the quark model, one can follow the scheme of the quark rearrangement model[I.RUBINSTEIN.66] which takes on two versions. In the $^3S_1$ model, one of the $\bar{p}p$ quark antiquark pairs annihilates into a gluon to create a $s\bar{s}$ pair in the $^3S_1$ state, as seen in Fig.I.B.1b. These calculations can be found in the following references [I.KOHNO.85,I.KOHNO.86,I.HENLEY.86,I.NISKANEN.85,I.MARUYAMA.87]. In the $^3P_0$ model, the annihilation involves the production of a $\bar{s}s$ pair with the quantum numbers of the vacuum (more than one gluon are exchanged), as seen in Fig.I.B.1c. This model has been treated by Green, Niskanen, and Wycech[I.GREEN.84], Dover and Fishbane[I.DOVER.84] as well as Maruyama, Furui, and Faessler[I.MARUYAMA.87].

As a conclusion, the annihilation to two mesons is a good source for getting information on quark gluon dynamics in the non pertubative region. While this annihilation to two mesons is just a minor fraction of the total $\bar{p}p$ annihilation cross section, specific channels combined with strong selection rules offer the best chance to look for resonances, including the $\xi(2230)$ which is discussed in detail in the next section.

I.C. $\xi(2230)$ Resonance.

The MARK III collaboration at SLAC has reported the first evidence of a surprisingly narrow resonance around 2230 MeV/c^2. It was discovered in the radiative decays of the J/Ψ in both the K^+K^- and K_SK_S invariant mass spectra, see Fig.I.C.1a. The resonance parameters (I.BALTRUSA.86) are given below in Table.I.C.1 where the first error given is statistical and the second error is systematic.

Table.I.C.1.

MARK III $\xi(2230)$ resonance parameters		
	$J/\Psi \rightarrow \gamma\xi \rightarrow K_SK_S$	$J/\Psi \rightarrow \gamma\xi \rightarrow K^+K^-$
Mass	$2232 \pm 7 \pm 7$ MeV/c^2	$2230 \pm 6 \pm 14$ MeV/c^2
Width	$18\ ^{+23}_{-15} \pm 10$ MeV/c^2	$26\ ^{+20}_{-16} \pm 17$ MeV/c^2
Significance	3.6 standard deviations	4.5 standard deviations
Reaction Branching Ratio	$3.2 \pm 1.7 \times 10^{-5}$	$4.2 \pm 2.9 \times 10^{-5}$

The presence of a K_SK_S final decay state channel limits the allowed quantum numbers to the even series $J^{PC}=0^{++},2^{++},4^{++},..$ as discussed in the previous section. The 0^{++} was later ruled out by a further analysis of the MARK III group. The remarkable feature of this resonance is its narrow width upper limit which is less than 40 MeV/c^2 at the 95% confidence level, and more importantly, consistent with the detector resolution. Because the radiative decay of the J/Ψ is a gluon rich process, Fig.I.C.1b, the discovery of the resonance led to a wide range of speculations about its possible origin from the exotic glueball or the elusive Higgs scalar to the more homely $s\bar{s}$ bound meson.

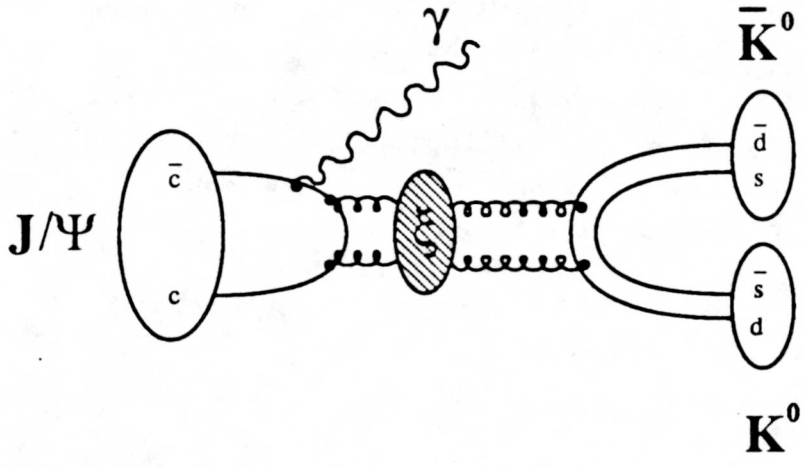

Fig.I.C.1b. Diagram of the $J/\Psi \rightarrow \gamma\xi \rightarrow K^0\,\bar{K}^0$ reaction. The radiative decay of the J/Ψ is a gluon rich channel.

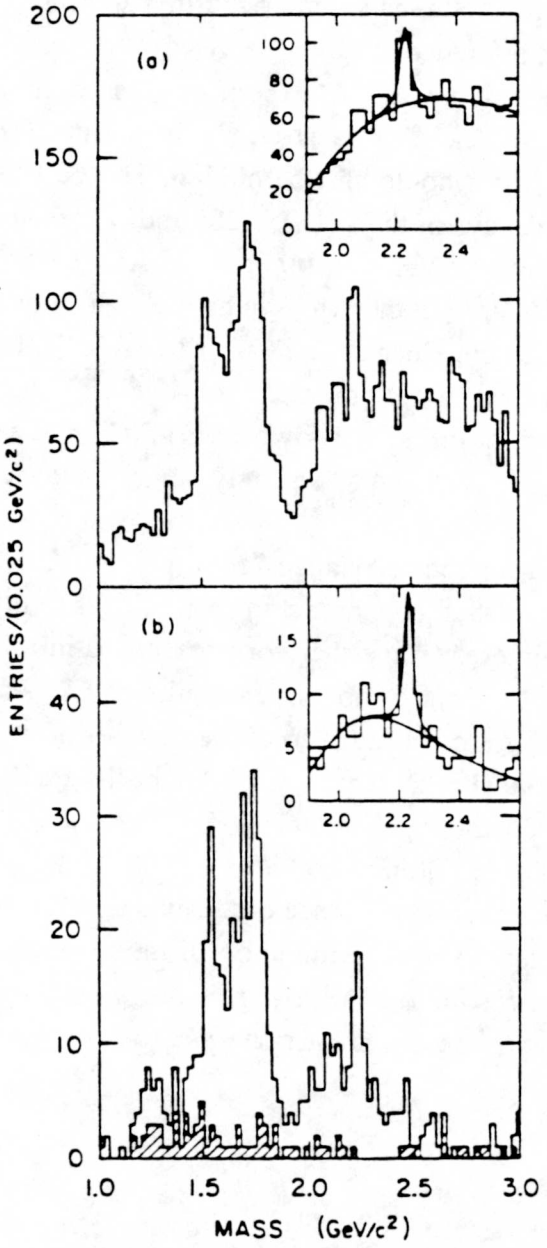

$$J/\Psi \rightarrow \gamma\,\xi \rightarrow K^{+}K^{-}$$

$$J/\Psi \rightarrow \gamma\,\xi \rightarrow K_S K_S$$

Fig.I.C.1a. MARK III collaboration data showing the invariant mass spectrum of the radiative J/Ψ decays into the K^+K^- (TOP) and K_sK_s (BOTTOM) final states. The structure at 2.23 GeV/c^2 is designated as the ξ.

The MARK III results immediately stimulated several experimental efforts to search for this resonance. The present experimental status is summarized in Table.I.C.2 together with the corresponding reactions used and references.

In a search similar to the MARK III collaboration, the DM2 experiment did not find any evidence for the resonance, as seen in Fig.I.C.2a. Only a structure of about 200 MeV/c^2 was found around 2.2 GeV/c^2 in which the ξ could still be hidden. The CLEO collaboration searched for the narrow state in the decays of the $\Upsilon(1S)$,$\Upsilon(2S)$ and B mesons but have statistics too low to show an enhancement. On the other hand, the LASS experiment reports a resonance at about 2220 MeV/c^2 in the $\Lambda K_S K_S$ channel with poor statistics. The GAMS collaboration has seen by far the clearest sign, after MARK III, of the resonance. By using the $\pi^- p \rightarrow \eta\,\eta'\,n$ reaction at two π^- momenta of 40 GeV/c and 100 GeV/c, a clear peak is seen in the invariant $\eta\,\eta'$ mass, as shown in Fig.I.C.2b. The width is not well determined but the fact that it decays to $\eta\,\eta'$ strongly suggest that its isospin is zero.

Finally two sets of experiments searched for the resonance in the $\bar{p}\,p \rightarrow K^+K^-$ channel. Neither experiment observed the resonance but gave branching ratio limits to the reactions. These last two results are of special interest since the work presented in this thesis is done in the $\bar{p}\,p \rightarrow K_S K_S$ channel. In fig.I.C.2c are shown the results of E789 at Brookhaven. No evidence for the structure can be found in the ratio of the number of $\bar{p}\,p \rightarrow K^+K^-$ to the number of $\bar{p}\,p \rightarrow \pi^+\pi^-$ events. A similar search at LEAR in the PS170 experiment, Fig.I.Cd, gave a similar result. Both experiments suffer from a high background $\bar{p}\,p \rightarrow K^+K^-$ cross section of the order of 50μb.

In conclusion, about half of the experiments report evidence of the existence of the ξ resonance but, the situation is still far from clear. The determination of the resonance width and mass are still limited by experimental resolution. All experiments which have seen evidence for the resonance seem to agree that the spin is greater or equal to two.

Table.I.C.2.

$\xi(2230)$ Experimental Situation						
Experiment (Laboratory)		Reaction used	Mass (MeV/c^2)	Width (MeV/c^2)	Spin J	References
MARK III	*seen*	$J/\Psi \rightarrow \gamma K^+K^-$	2230 ± 6	26^{20}_{-16}	≥ 2	I.BALTRUSA.86
(SLAC)	*seen*	$\rightarrow \gamma K_SK_S$	2232 ± 7	18^{23}_{-15}	≥ 2	
DM2	*not seen*	$J/\Psi \rightarrow \gamma K^+K^-$				I.AUGUSTIN.88
(Orsay)	*not seen*	$\rightarrow \gamma K_SK_S$				
CLEO	*not seen*	$\Upsilon(1S) \rightarrow \gamma K^+K^-$				I.BEHRENDS.84
(CESR)		$\Upsilon(2S) \rightarrow \gamma K^+K^-$				
		$B \rightarrow \gamma K^+K^-$				
LASS	*evidence*	$K^-p \rightarrow \Lambda K^+K^-$				I.ASTON.87
(SLAC)	*evidence*	$\rightarrow \Lambda K_SK_S$	~2230	<100	≥ 2	
GAMS	*seen*	$\pi^-p \rightarrow \eta\eta' n$	2220 ± 10	<120	≥ 2	I.ALDE.86
(CERN-IHEP)					(I=0)	
IHEP	*seen*	$\pi^-p \rightarrow K_SK_S n$	2220 ± 20	80 ± 30	≥ 2	I.BOLONKIN.87
(Serpukhov)						
E789	*not seen*	$\bar{p}p \rightarrow K^+K^-$				I.SCULLI.87
(Brookhaven)						
PS170	*not seen*	$\bar{p}p \rightarrow K^+K^-$				I.BARDIN.87
(LEAR)						

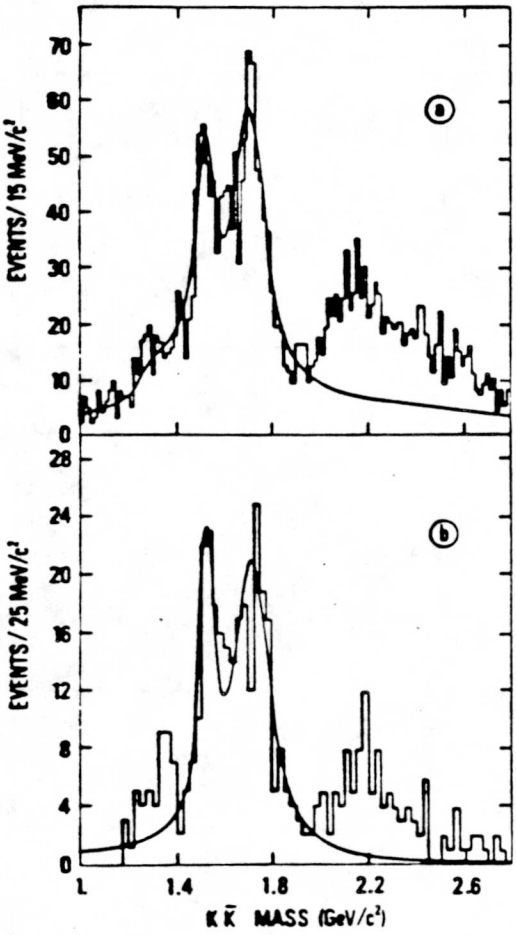

Fig.I.C.2a. DM2 invariant K^+K^- a) and K_sK_s b) mass distribution spectra obtained from the radiative decays of the J/Ψ .

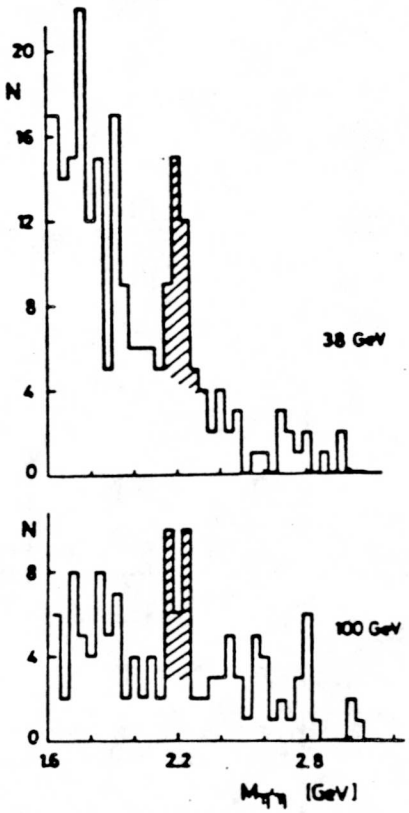

Fig.I.C.2b. GAMS invariant mass spectra of η η' events produced by 38 GeV/c and 100 GeV/c π^- on proton from the $\pi^- \rightarrow \eta\,\eta'\,n$ reaction. The bin width is 40 MeV/c^2.

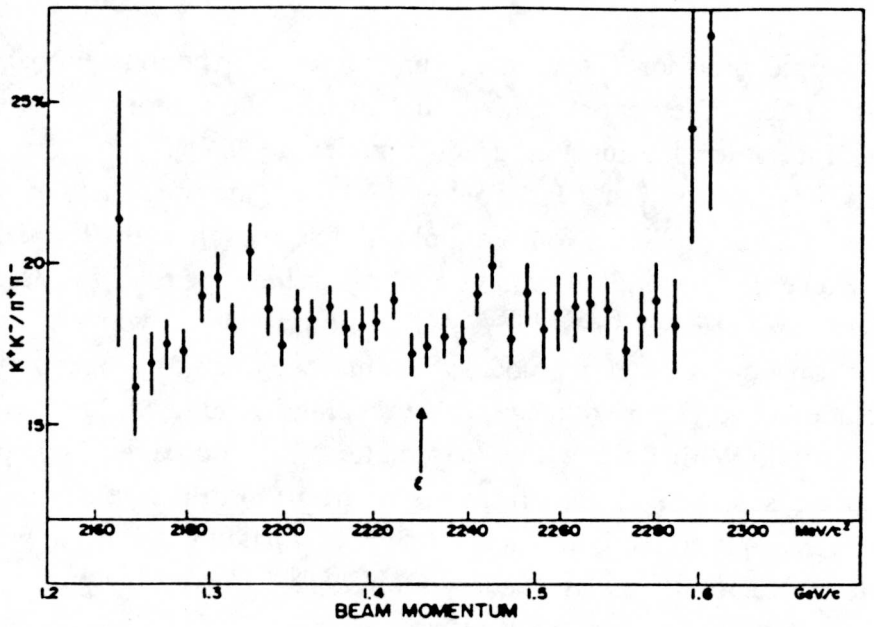

Fig.I.C.2c. E789 ratio of the numbers of $\bar{p}\,p \rightarrow K^+K^-$ to $\bar{p}\,p \rightarrow \pi^+\pi^-$ events plotted in 3.5 MeV/c^2 mass bins

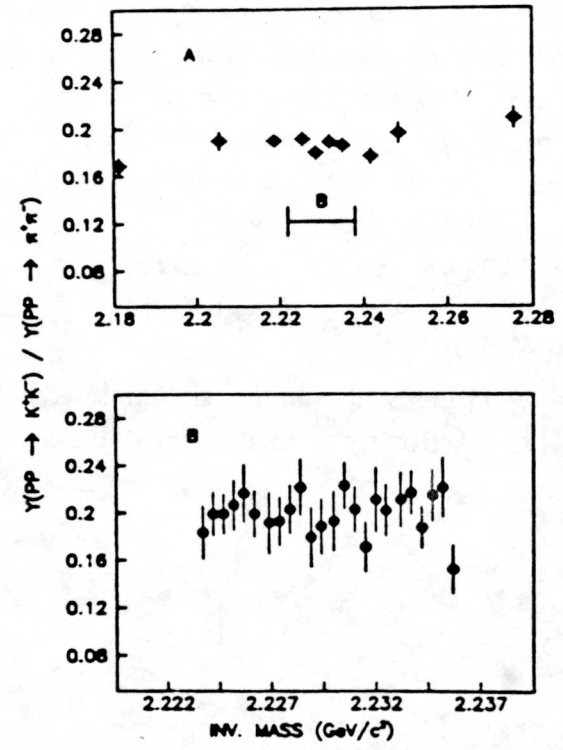

Fig.I.C.2d. PS170 ratio of the numbers of $\bar{p}\,p \rightarrow K^+K^-$ to $\bar{p}\,p \rightarrow \pi^+\pi^-$ events for invariant mass bins of 3.6 MeV/c^2 (A) and 0.6 MeV/c^2 (B).

The theoretical interpretations of this resonance are numerous. The most probable ones are shown in Table.I.C.3. The second and third columns show those different experimental results which speak for or against the specific model.

According to Godfrey, Kokoski and Isgur (I.GODFREY.84), the properties of the $\xi(2230)$ are consistent with those predicted for a simple L=3 $s\bar{s}$ meson with $J^{PC}=2^{++}$. Their finding is based on an extensive and impressive analysis of the spectroscopy, decay widths, and other properties of mesons (I.GODFREY.85) in a quark model which uses a relativized version of the usual quark potential model with chromodynamics, Appendix E. This quark potential includes a one-gluon exchange with a running coupling constant and a linear confinement potential. With only a few parameters, the model leads to an understanding of the spectroscopy of mesons from the lightest (π) to the heaviest (Υ) known. The mass of the $\xi(2230)$ is correctly predicted but the calculated width is too wide (~60 MeV/c^2). A similar calculation for a $s\bar{s}$ state by Ono (I.ONO.87) yields a width in excess of 300 MeV/c^2, much larger than Godfrey's results.

A more exotic interpretation of the ξ resonance in terms of a glueball bound state has been proposed by Chanowitz(I.CHANOWITZ.83) and Ward(I.WARD.85). In the radiative decay of the J/Ψ, fig.I.C.1, the $c\bar{c}$ quark pair annihilates into two gluons. Because of the non-Abelian nature of the strong force, two gluons can interact and form a bound state called a glueball. The signature for a glueball is, unfortunately, difficult to uncover. A glueball looks a lot like an ordinary meson with similar quantum numbers. Some resonances such as the i(1440) and $\theta(1700)$ which can be seen in the MARK III and DM2 spectra are prime candidates as glueball states. Calculations using the MIT bag model shows that glueball masses can be in the region of the observed resonance, although the predicted width seems too high (of the order of 100 MeV/c^2).

As an alternative to the glueball hypothesis, $q\bar{q}g$ hybrid particles called meikton, are also possible (I.CHANOWITZ.83,I.CHAO.88). A meikton will preferably decay into strange particles and have a mass below 2.5 GeV/c^2.

Other interpretations such as Higgs scalar and $s\bar{s}s\bar{s}$ states have lost their appeal because they require a $J^{PC}=0^{++}$ which is strongly contradicted by all experiments.

Table.I.C.3.

$\xi(2230)$ Theoretical Interpretation			
Interpretation	Evidence for	Evidence against	References
$^3F_2$ ($s\bar{s}$) meson	$J^{PC}_{\xi} = 2^{++}$ $2210 \leq M_{\xi} \leq 2270$ MeV/c^2 $\xi \rightarrow \pi\pi$ suppressed ω like partner at 2100 MeV/c^2 found	$\Gamma_{\xi} \geq 60$ MeV/c^2	I.GODFREY.84 I.ONO.87
Glueball	$J^{PC}_{\xi} = 2^{++}$ M_{ξ} in range $\xi \rightarrow KK$ enhanced	$\xi \rightarrow \pi\pi$ not observed $\Gamma_{\xi} > 100$ MeV/c^2	I.CHANOWITZ.83 I.WARD.85
Meikton $q\bar{q}$ g	narrow width Mass in range 2^{++} possible	$\xi \rightarrow \phi\omega, K^*K^*$ not seen	I.CHAO.88 I.CHANOWITZ.83
Higgs scalar	Γ_{ξ} very narrow $Y \rightarrow \xi\gamma$ not seen	$J^{PC}_{\xi} = 0^{++}$ $M_{\xi} << 7$ GeV/c^2	I.SHATZ.84 I.WEINBERG.76 I.HABER.84 I.WILLEY.84
Exotic $s\bar{s}s\bar{s}$	narrow width	$J^{PC}_{\xi} = 0^{++}$	I.PAKVASA.84

I.D. Search of the $\xi(2230)$ Resonance in the $\bar{p}\,p \rightarrow K_S K_S$ Channel.

During the last six years, the PS185 collaboration at CERN (European Center for Nuclear Research) has been conducting an extensive study of the $\bar{p}\,p \rightarrow \bar{\Lambda}\,\Lambda$ reaction near threshold(I.MAHER.86,I.BARNES.87A,I.BARNES.87B,I.FRANKENBERG.87,I.DUTTY.88). Because of the similarities of the reactions, a search for the $\xi(2230)$ resonance in the $K_S K_S$ channel is a natural extension of the PS185 experiment. Both the Λ and K_S are neutral particles which decay primarily to two charged particles with comparable lifetimes of 263ps and 89ps. Therefore, with a relatively minor change of the experimental apparatus, a scan in the mass region of the resonance is possible.

The $\bar{p}\,p \rightarrow K_S K_S$ cross section is not very well known as shown in Fig.I.D.1. The world data set consists of about 100 events measured in bubble chamber experiments. No differential cross sections are available. The measurement of this cross section by the PS185 collaboration represents, therefore, the first real measurement of the proton antiproton annihilation into two K_S.

Because of the expected low $\bar{p}\,p \rightarrow K_S K_S$ non-resonant cross section in the 2 μb range (0.01% of the $\bar{p}\,p$ total cross section), this measurement offers the best possibility to determine the mass and width of the ξ resonance as well as its spin, through the determination of the differential cross section. If the resonance can not be seen in this channel, the limit on the product of the branching ratios $BR(\bar{p}p \rightarrow \xi).BR(\xi \rightarrow K_S K_S)$ set by the PS170 and E789 experiments and which are in the 10^{-4} range, see Table.VII.1, is expected to be lowered.

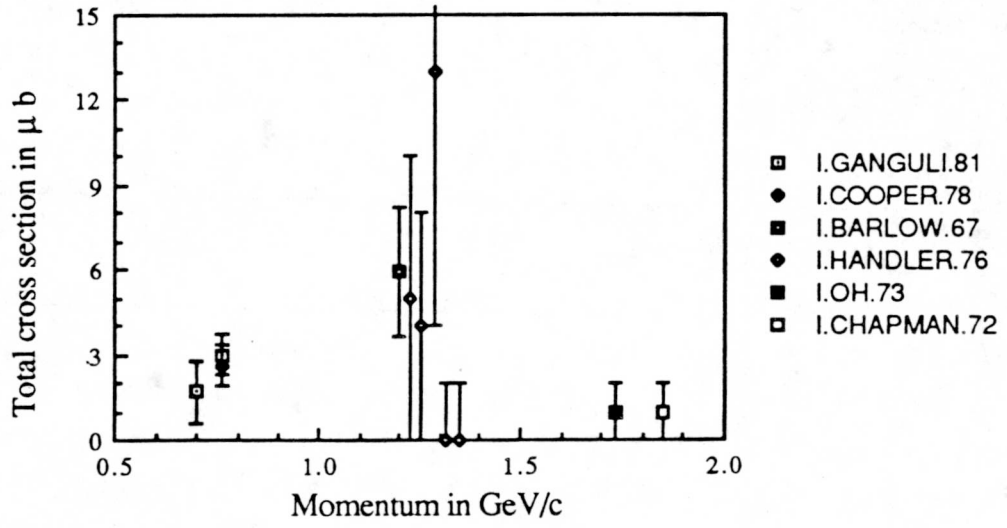

Fig.I.D.1. World cross section of the $\bar{p}\,p \rightarrow K_S K_S$ reaction.

The kinematics of the $\bar{p}\,p \rightarrow K_S K_S$ reaction is very different from the $\bar{p}\,p \rightarrow \bar{\Lambda}\,\Lambda$ reaction. There are no maximum laboratory angles at which the K_S is emitted. Fig.I.D.2a shows the momentum of the K_S as a function of its laboratory polar angle θ. Because of the "open" kinematics of K_S reaction, we also have a one to one and almost linear relation between the laboratory and center of mass θ angle as seen in Fig.I.D.2b. This "open" kinematics is not surprising if we remember that the antiproton momentum range here is well away from the $K_S K_S$ threshold. For the same reason, the K_S kinematics is essentially the same over the momentum range near the $\xi(2230)$ peak.

There are two additional kinematic characteristics which are of importance for the experimental design and the data analysis. First, Fig.I.D.2c shows the momentum distribution of the backward and forward moving pions for isotropically distributed K_S. Second, the opening angle distribution of the decay pions with respect to the K_S is shown in Fig.I.D.2d. Because the K_S momentum does not exceed 2 GeV/c in the laboratory, small opening angles of the decay pions ($< 23°$) are not as probable as the middle range of angles and are the object of a cut in the later part of the analysis (section III.D).

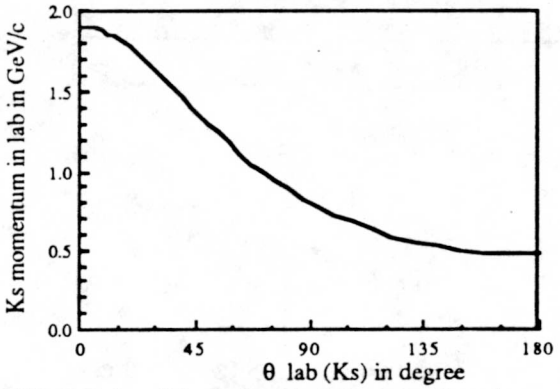

Fig.I.D.2a. Momentum of K_S as a function of its laboratory polar angle θ_{lab}.

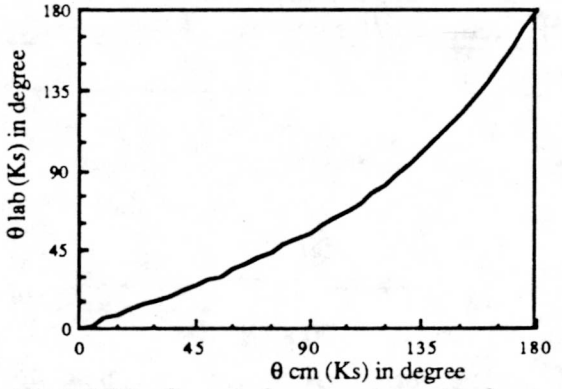

Fig.I.D.2b. Center of mass polar angle θ_{cm} as a function of laboratory polar angle θ_{lab} for K_S.

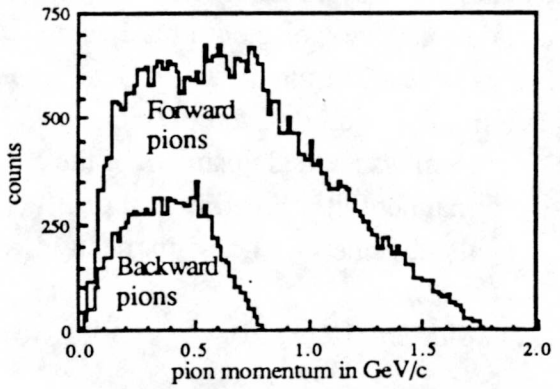

Fig.I.D.2c. Distribution of the decay pion momentum for forward pions with $\theta_{lab} < 90°$ and backward pions with $\theta_{lab} > 90°$.

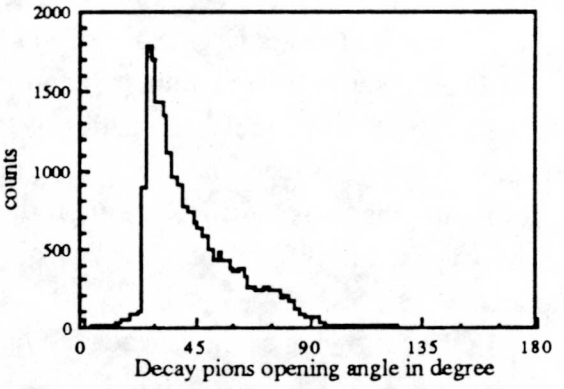

Fig.I.D.2d. Distribution of the decay pions opening angle.

II. Experimental Set Up and Data Taking.

II.A. Experimental Set Up.

II.A.1. Overview.

The search for the $\xi(2230)$ was performed at the Low Energy Anti proton Ring (LEAR) at CERN in the summer of 1986. LEAR is a small storage and time stretcher synchroton which uses stochastic cooling to offer an antiproton beam of exceptional quality as shown in Table.II.A.1.

Table.II.A.1

LEAR beam definition	
Intensity	.3 to 2 x 10^6 $\bar{p}$/s
Momentum range	100 MeV/c to 2 GeV/c
Beam size (at PS185 target)	.7 x 1.2 mm^2 (II.FRANKENBERG.88)
Momentum definition	$\Delta\bar{p}/\bar{p} \sim 10^{-3}$
Contamination	pure (no π)

The production and accumulation of antiprotons are done by the CERN accelerator complex. These antiprotons are then injected into LEAR at .6 GeV/c where they are accelerated or decelerated and extracted in continuous forty five minutes spills to the different experiments including our experiment. The quality and flexibility of the LEAR beam allowed us to do a very precise search around the $\xi(2230)$ resonance.

The same PS185 experimental set up which has been used since 1983 to map the $\bar{p}\,p \rightarrow \bar{\Lambda}\,\Lambda$ reaction near threshold was used to measure the $\bar{p}\,p \rightarrow K_sK_s$ reaction. This detector arrangement is shown in Fig.II.A.1. The PS185 detection system consists of four main components. First, a target system and a hodoscope define the experiment's hardware trigger. Then, a set of drift chambers record the trajectories (tracks) of the decay products. Also, because of the "wide" kinematics of the K_sK_s reaction compared to the previously measured $\bar{p}\,p \rightarrow \bar{\Lambda}\,\Lambda$ reaction, a new streamer detection system was added upstream of the target to track the backward K_s decay products. Finally, a magnet with three internal drift chambers is used to differentiate the $\bar{\Lambda}$ from the Λ by analysing the charge of its decay products.

In the following sections, each components will be further discussed.

PS185 Detection System

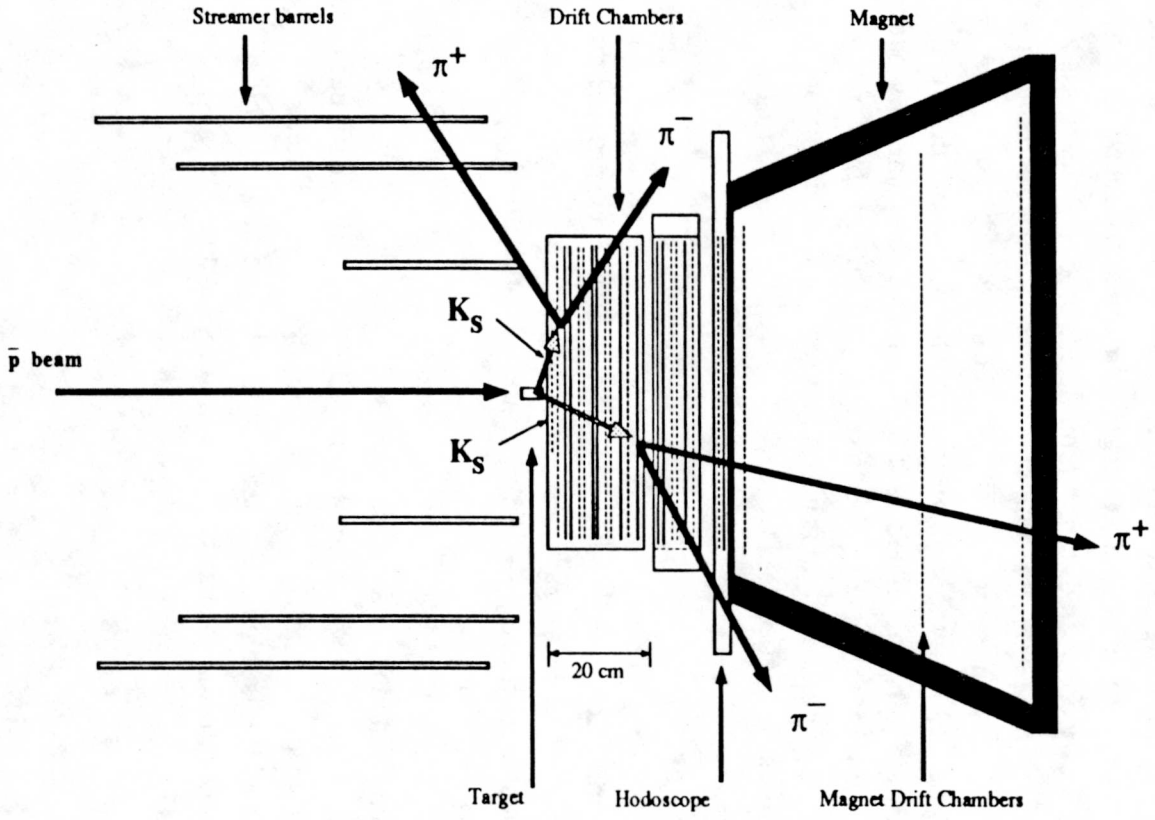

Fig.II.A.1. Scale Drawing of the PS185 detector. The Target system and the Hodoscope define the trigger for two neutral particles. The Magnet and its internal Drift Chambers determine the baryon numbers of the decay products. The streamer planes can be moves upstream to allow easy access to the target. Note that the second stack of Drift Chambers is rotated by 14° to help resolve track ambiguities.

II.A.2. Target.

In order to efficiently kinematically reconstruct both neutral particle decays from four charged particles, the $\bar{p}$ p interaction point must be constrained to a small volume. The use of a small target system of five cells combined with the LEAR anti proton beam size offer such a function.

The target system, Fig.II.A.2, developed by the University of Erlangen group consists of five cylindrical cells of 2.5 mm diameter. Each target cell is separated by two 0.1 mm thick beam scintillators (S3's) and surrounded by a 1 mm thick barrel scintillator (S2). The latter is used to reject any charged particles produced in that cell. These scintillators are optically connected to photomultiplier tubes by plexiglass light guides. A neutral event, such as $\bar{p}\,p \rightarrow K_sK_s$ happening in the third cell for example, requires S1a.S1 to define an antiproton reaching the target (or BEAM EVENT), S31.S32.$\overline{S33}$.$\overline{S34}$.$\overline{S35}$ to know that an antiproton stopped in the third cell, $\overline{S21}$.$\overline{S22}$ to ensure that the beam is fully collimated, and $\overline{S23}$ to make sure that only neutral particles have come out of the third target cell. The first four cells are made of polyethylene CH_2, while the last cell is a graphite cell and is used to correct for the carbon contamination of the CH_2 cells, as discussed in section IV.D.1.

II.A.3. Hodoscope.

The hodoscope, combined with the target neutral trigger, provide the experiment's fast trigger on the charged decay particles. The hodoscope is designed to provide a 100% trigger level acceptance for the $\bar{p}\,p \rightarrow \bar{\Lambda}\,\Lambda$ reaction over the LEAR momentum range and must subtend a large solid angle.

Built by the Carnegie-Mellon Medium Energy Group[II.MAHER.86], the hodoscope has two orthogonal (X and Y) planes, each of which consists of twenty one 0.4 cm x 62 cm x 3 cm scintillator slabs, as shown in Fig.II.A.3. Photomultiplier tubes on both ends of each slab are used to detect the light output. The hodoscope frame is then bolted to the solenoid magnet used to distinguish the decay products (p and $\bar{p}$) of the $\Lambda \rightarrow p\,\pi^-$ and $\bar{\Lambda} \rightarrow \bar{p}\,\pi^+$. The magnet information has not been used in this analysis.

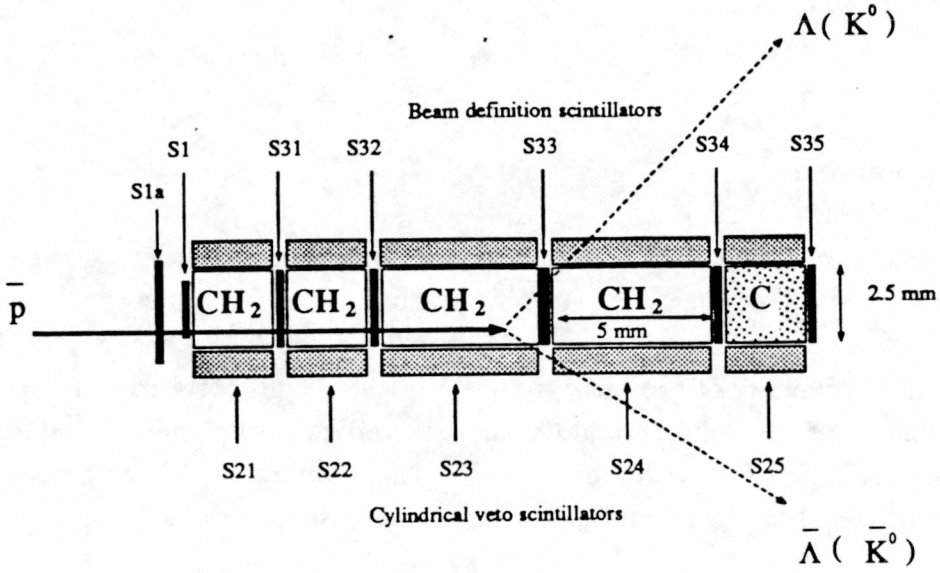

Fig.II.A.2. Side view of the cylindrical target arrangement.

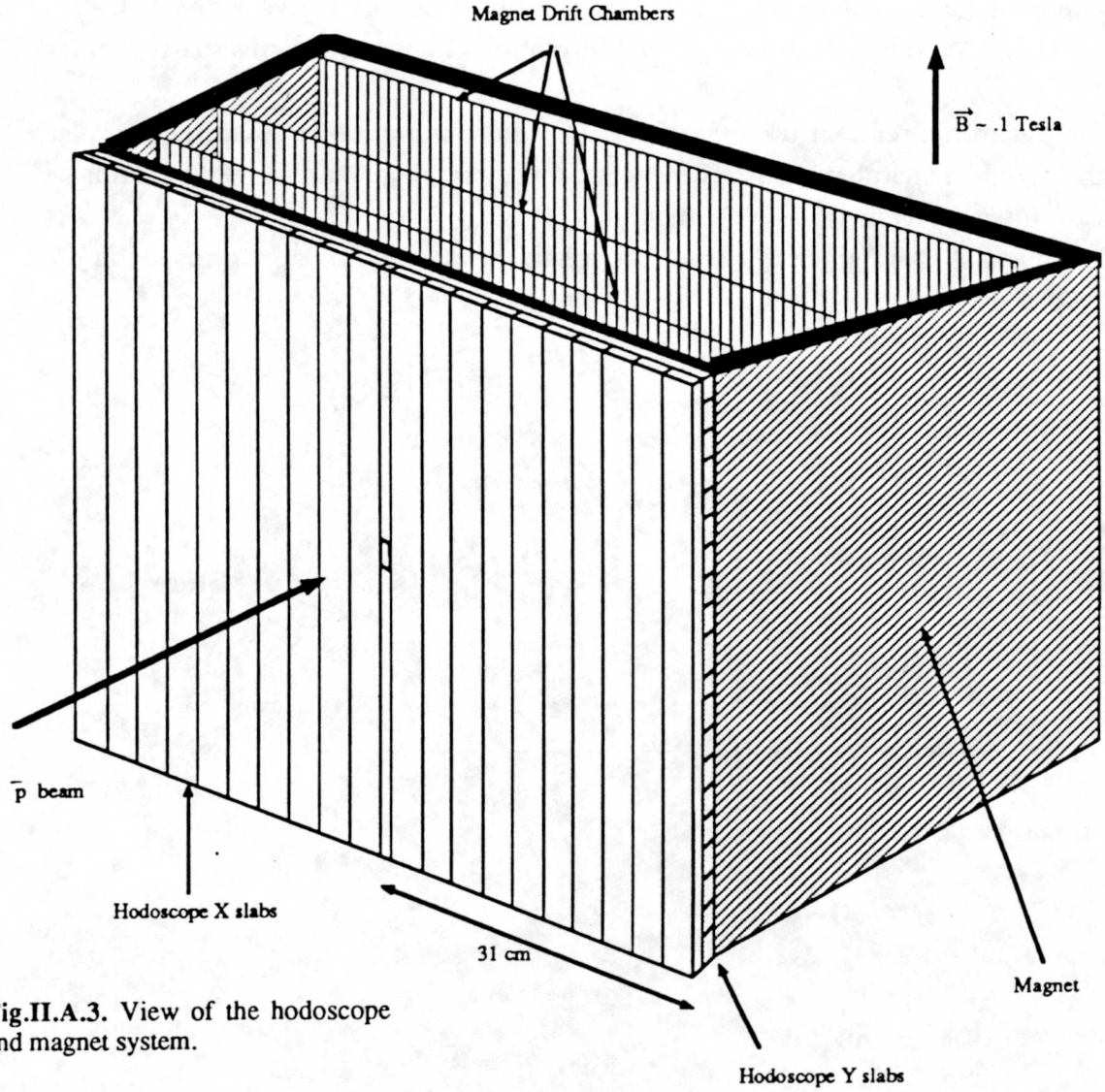

Fig.II.A.3. View of the hodoscope and magnet system.

II.A.4. Drift Chambers.

The downstream drift chamber stacks allow an almost complete geometrical acceptance (95% to 99%) of the $\bar{p}\ p \rightarrow \bar{\Lambda}\ \Lambda$ reaction. The $\bar{\Lambda}$ and Λ particles are kinematically constrained in a forward cone of less than 25° at the energy range studied.

Built by the University of Freiburg group[II.ULMER.87], the forward drift chamber stack (DC13) consists of seven horizontal (X) and six vertical (Y) planes. An additional drift chamber stack (DC6) of three X' and three Y' planes rotated by 16° with respect to DC13 is added to resolve track ambiguities and increase the detector acceptance, Fig.II.A.4b.

Each plane has fourteen cells (28 sense wires) as shown in Fig.II.A.4a and an active area of 56 x 56 cm^2. The gas used is a mixture of 30% Isobutane, 67.6% Argon, and 2.4% Methylal. High voltages applied to the sense wires (1900 V), the field wires (-3300 V) and the field shaping wires (graded from 0 to 3000 V) give a constant drift velocity of 50 mm/μs over the cell length and resolution of about 200 μm at particle track angles of 0°.

The electronic readout uses the Nevis Lab System and takes less than 10 μs to process the 516 drift chamber wires. The raw drift chamber data consists of wire numbers and cell drift times given in 1.5 ns increment.

In Table.II.A.2 are given the list of drift chamber planes and their corresponding Z positions along the beam.

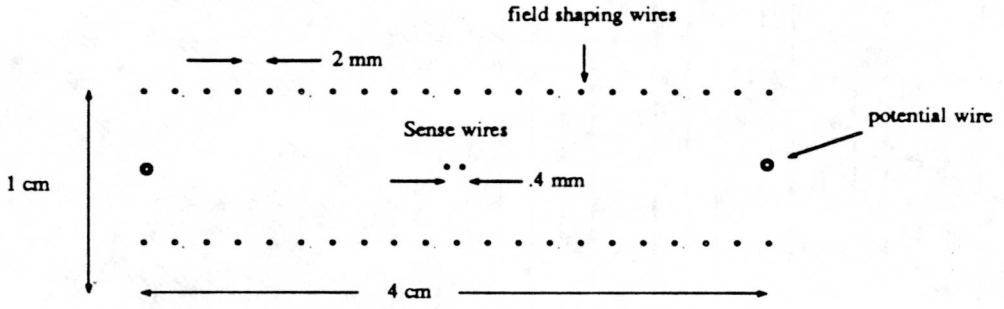

Fig.II.A.4a. Drift chamber drift cell.

Table.II.A.2

Drift Chamber Plane Definition			
Plane number	Z position (cm)	Projection	Stack
1	0.9943	X	DC13
2	1.9886	X	
3	3.6800	Y	
4	4.6743	Y	
5	6.3657	X	
6	7.3600	X	
7	9.0514	Y	
8	10.0457	Y	
9	11.7371	X	
10	12.7314	X	
11	14.4229	Y	
12	16.1143	X	
13	17.8057	Y	
14	21.9557	Y'	DC6
15	22.9557	Y'	
16	24.6557	X'	
17	25.6557	X'	
18	27.3557	Y'	
19	29.0557	X'	

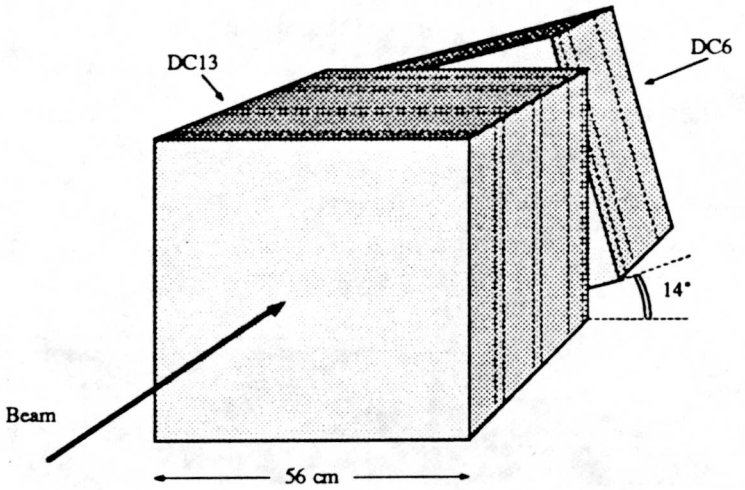

Fig.II.A.4b. Drift chamber stack DC13 and DC6 rotated by 14°.

II.A.5. Streamer Chambers.

An additional upstream detector is needed to measure the "backward" decay pions from the reaction $\bar{p}\,p \rightarrow K_S K_S$. Plastic streamer tubes operated in a limited streamer mode[II.BATTISTONI.80,II.BATTISTONI.83] offer a relatively simple and inexpensive solution to the increase of solid angle acceptance of our total detector.

The streamer tube arrangement has been built using the CHARM II experiment production line[II.DEWULF.86] and consists of three concentric barrels fixed on a frame which can be moved along the beam direction to facilitate access to the target and to the stack chambers. Each barrel has four planes and covers an azimuthal angle of nearly 360 degrees, as seen in Fig.II.A.5b.

In Fig.II.A.5a is shown a cross section of one of the streamer planes. The base of the streamer tube is an open PVC profile coated with graphite (cathode) in which eight 100 μm Cu-Be wires (anode) are strung. Two profiles are then inserted in a sheath of plastic to allow a sixteen wire gas tight system. The gas used is a mixture of 75% Isobutane and 25% Argon. High voltage in the range of 4200 to 4500 V is applied on the graphite. This system, besides its simplicity, has three main advantages : a large anode signal (~50mV/50Ω), a fast rise time (<5ns) and a wide high voltage range. Because of a fairly long recovery time, the streamer tubes are best suited for low count rate which is easily fulfilled by our setup. When a particle traverses a cell, it produces a pulse on the anode wire as well as an induced pulse on the pick up strip shown in Fig.II.A.5a allowing a " X Y " readout on each plane.

The signal is then digitalised by a Lecroy 4200 STOS card and shifted via four busses to an encoder. Approximatively 500 μs are necessary to read the 1408 channels. Also, a fast OR output is used as part of the trigger. Raw hits are then encoded into wire numbers and cluster sizes defined by the number of contiguous wires or strips which fired.

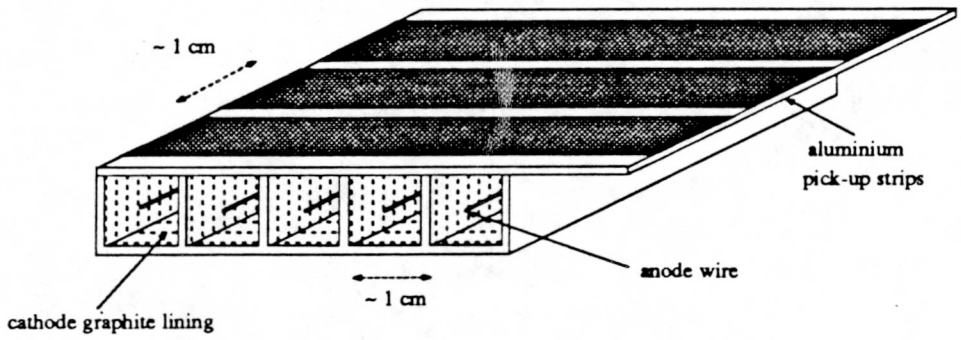

Fig.II.A.5a. Part of a X and Y streamer plane

Table.II.A.3.

Streamer Chamber Definition				
Plane number	Plane position from beam (cm)	Bin width (cm)	Plane type	Quadrant
1	-23.7	1.0375	inner wire	LEFT
2	-23.7	1.2	inner strip	
3	-42.7	1.0375	center wire	
4	-42.7	1.2	center strip	
5	-52.8	1.2	outer strip	
6	-52.8	1.0375	outer wire	
7	23.7	1.0375	inner wire	RIGHT
8	23.7	1.2	inner strip	
9	42.7	1.0375	center wire	
10	42.7	1.2	center strip	
11	52.8	1.2	outer strip	
12	52.8	1.0375	outer wire	
13	23.7	1.0375	inner wire	BOTTOM
14	23.7	1.2	inner strip	
15	42.7	1.0375	center wire	
16	42.7	1.2	center stip	
17	52.8	1.2	outer strip	
18	52.8	1.0375	outer wire	
19	-23.7	1.0375	inner wire	TOP
20	-23.7	1.2	inner strip	
21	-42.7	1.0375	center wire	
22	-42.7	1.2	center strip	
23	-52.8	1.2	outer strip	
24	-52.8	1.0375	outer wire	

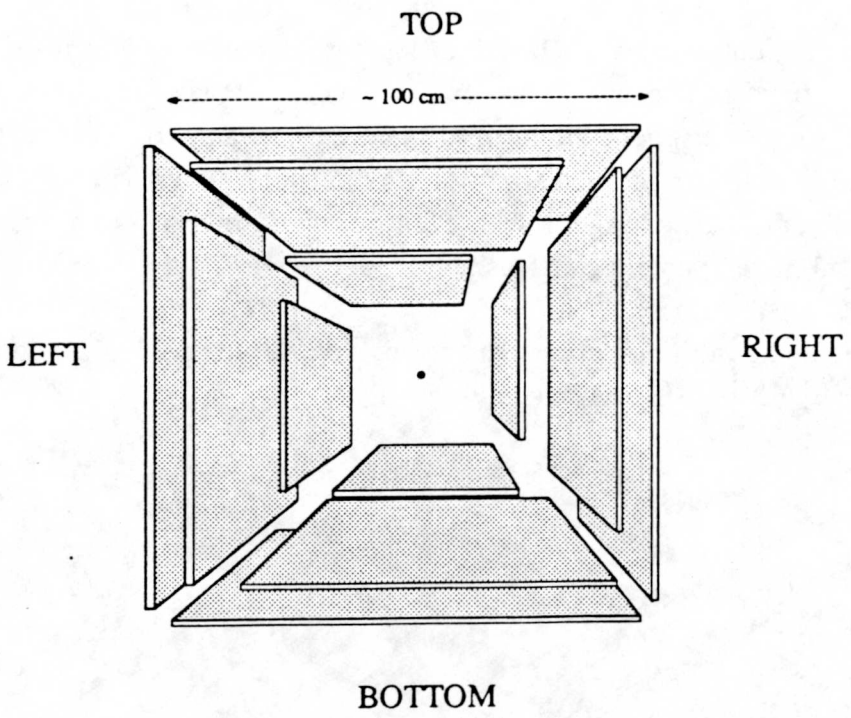

Fig.II.A.5b. View of the streamer detector in the direction of the beam.

II.A.6. Data Acquisition and Trigger Logic.

A data acquisition system is needed to control the data flow of the experiment from gathering information from the different detector hardwares (through the CAMAC system) to event logging and monitoring (through a μVAX II computer). A special purpose microcomputer, the MBD-11 Microprogrammed Branch Driver, serves as an interface between the CAMAC system and the μVAX II q bus, see Fig.II.A.6.

In the CAMAC crates are the ADC's and TDC's into which are recorded the pulse height and time information of the target and hodoscope scintillator signals. The CAMAC crates also include the scalers, the special TDC NEVISLAB system used to decode the drift chamber hits, and the STOS system for the streamer plane decoding.

The MBD-11 then gathers the information from the CAMAC system and performs a direct memory access data transfer to the μVAX II. The transfer is done by using the program DATAQ which is downloaded from the μVAX.

Finally in the μVAX II itself are five programs, each of them working concurrently, controlling and monitoring the data flow.

As shown in Fig.II.A.6, the program CONTROL receives the data from the MBD-11 and distribute it to the other programs. CONTROL also does a rudimentary analysis on a portion of the incoming data. TAPEIT writes the data to magnetic tapes, SCREAD reads the scaler information of the experiment. Finally HISTO and TRAIL allow us to display useful histogram information and visualize events in the different detector components.

Three kind of event triggers can be defined and written to tape. The main trigger is the neutral trigger defined as a neutral event from the target and at least one X and one Y hit in the hodoscope. Another trigger , the beam trigger, defines an antiproton reaching the target first cell and used to correct the antiproton flux in each cell, as will be discussed in section IV.B. Finally, the elastic trigger selects events of the form $\bar{p}\ p \rightarrow \bar{p}\ p$ and is used in the calibration of the drift chambers. This last trigger requires a beam event associated with at least one X and Y hodoscope hit.

A more detailed description of the data acquisition and trigger logic is found in the thesis of C. Maher (II.MAHER.86) and R. von Frankenberg(II.FRANKENBERG.88).

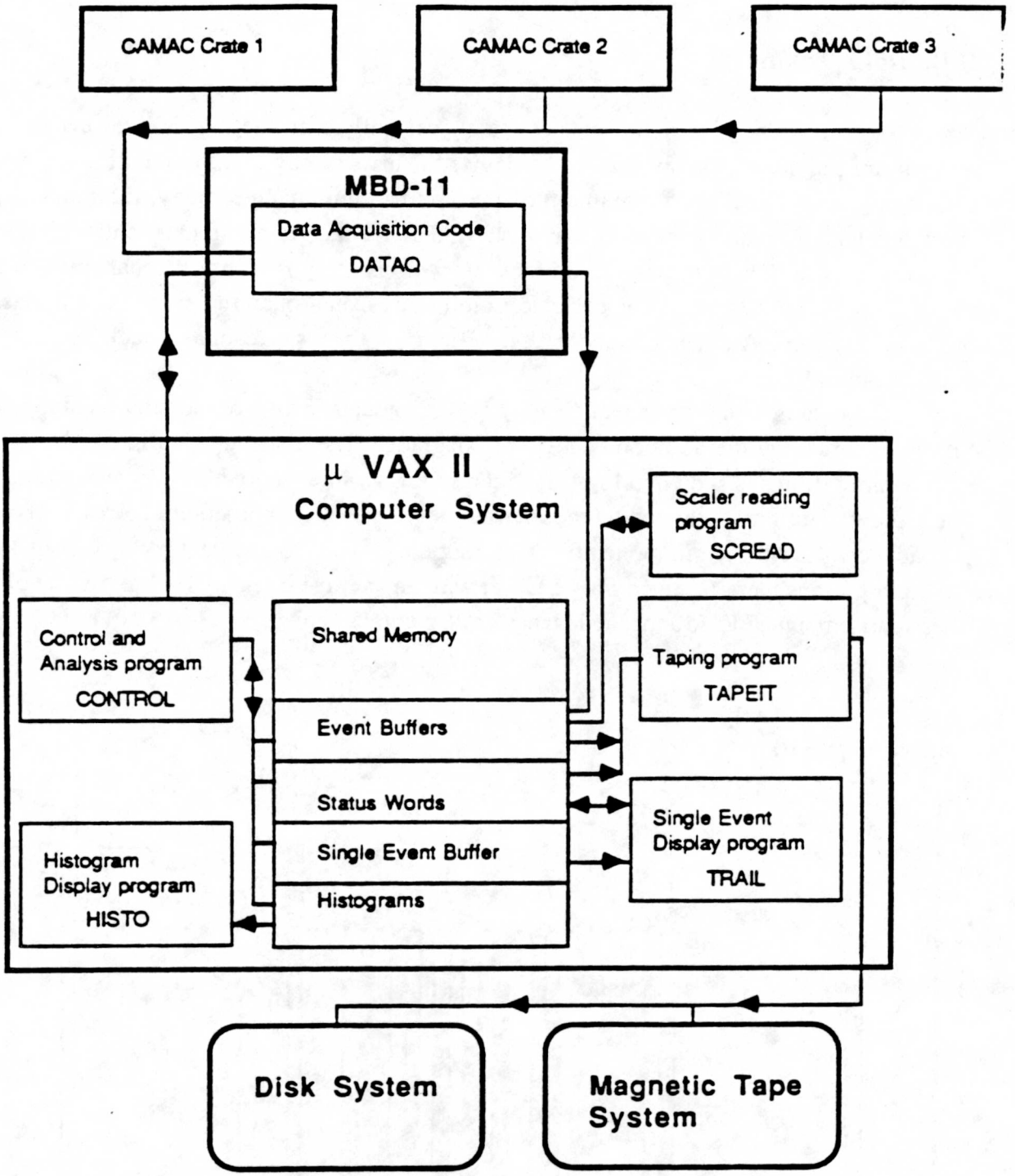

Fig.II.A.6. Data acquisition diagram[II.MAHER.86].

II.B. Data Taking.

In order to maximize our chances to successfully map the $\xi(2230)$ resonance, a momentum scanning strategy had to be devised. This strategy had to take into account LEAR constraints such as a maximum of two momentum changes a day, the relatively short data taking time of twelve days and the MARK III uncertainty in mass and width, as seen in Fig.I.C.1. This uncertainty in mass as well as the possibility if a narrow width required a broad and, as much as possible, continuous scan around the invariant $\bar{p}$ p mass of 2230 MeV/c^2. Also, a precise measurement of the non-resonant background is indispensable.

The data is then extracted at eleven LEAR momenta. Seven of these momenta were further extended by the addition of a 1.5 cm degrader. The distribution of the seventeen momentum settings is shown in Fig.II.B.1; the settings with a degrader are shown in dark. The $\bar{p}$ p invariant mass scanned by the four target cells at each momentum corresponds to 3.2 MeV/c^2 (4.5 MeV/c^2 in momentum). During the eleven days of data taking, about 1.5 10^{11} anti protons were received on the target with an average intensity of 3 to 4 x 10^5 $\bar{p}$/s. These data amounted to 150 magnetic tapes written at 6250 bpi.

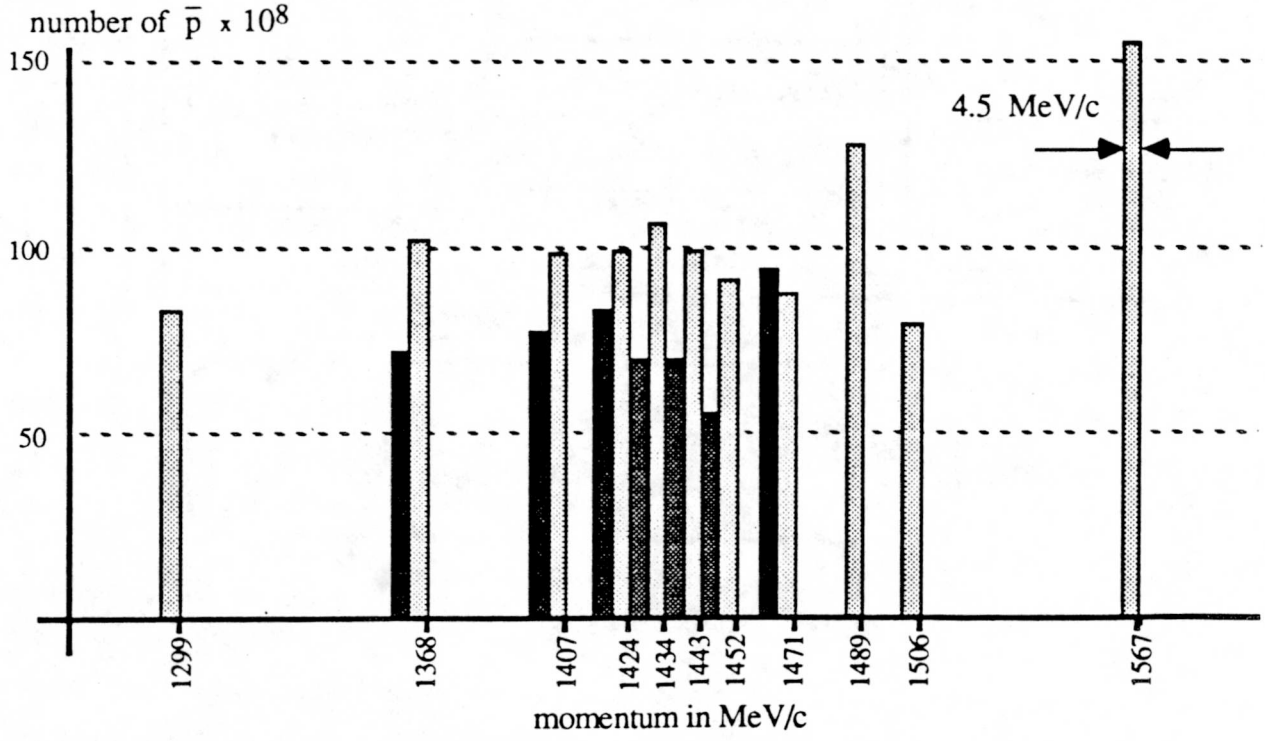

Fig.II.B.1. Number of anti protons received on the target at each momentum. The darker bins are the runs in which the degrader was used.

III. Data Analysis and Data Reduction.

III.A. Overview.

Of the 36 million events written to tape, less than 0.01% of these raw events are expected to correspond to the $\bar{p}\,p \rightarrow K_S\,K_S \rightarrow \pi^+\,\pi^-\;\pi^+\,\pi^-$ or $\bar{p}\,p \rightarrow \bar{\Lambda}\,\Lambda \rightarrow \;\bar{p}\,\pi^+\;p\,\pi^-$ reactions. In order to extract these events, an extensive computer analysis has been developed in which the raw experimental data are scanned in a series of steps, each step leading to an enriched data sample (reduction). In both reactions, the antiproton and proton annihilate into two neutral particles which in turn decay into two charged particles. Hence we look for a four prong signature whose corresponding tracks are straight lines (no magnetic field present) and whose simple kinematics can be decomposed into a series of two body reactions, Fig III.A.1.

Before undertaking a detailed study of the data analysis, a brief overview of the analysis program is presented. A simplified diagram, as in Fig III.A.2, illustrates the main components of the analysis and also defines terms which will be used in this chapter.

The data analysis consists of four main parts, each roughly corresponding to a basic reduction step:

1) First, the raw data are decoded and transformed into hits or coordinates. In each projection of the drift chamber stacks and streamer tube barrels, tracks are found (2D track) and combined to form three dimensional tracks (3D track).

2) Each combination of three dimensional tracks (1V) is checked to see if their distance of closest approach is small enough to undergo a vertex fit.

3) From a combination of two independent vertices (2V), a kinematical estimate (guess) is generated. In other words, we see that the candidate "grossly" obeys the kinematical constraint of the reaction. A "good" event will have successfully undergone a χ^2 minimization procedure subject to the two body kinematical constraint. For $\Lambda\,\bar{\Lambda}$ events near threshold, the kinematics is sufficiently unique to discriminate against possible background. Unfortunately, in the K_SK_S case, because of the limitation of the detector (streamers having only three planes of limited efficiencies and resolution), unwanted background cannot be eliminated completely and therefore reduces the discrimination power of the χ^2 procedure.

4) Finally, in order to link the analysis to physics measurements such as cross section and differential cross section, a simulation of the reaction is made to determine the response (acceptance) of the detector and allow a credible normalization.

The first three steps are discussed in more detail in the following sections. The normalization is topic of Chapter IV.

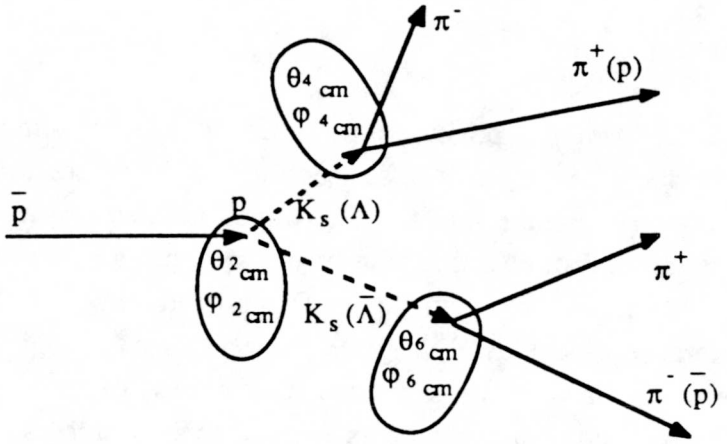

Fig.III.A.1. The $\bar{p}\,p \rightarrow K_S\,K_S$ and $\bar{p}\,p \rightarrow \bar{\Lambda}\,\Lambda$ reactions as a series of three two-body reactions.

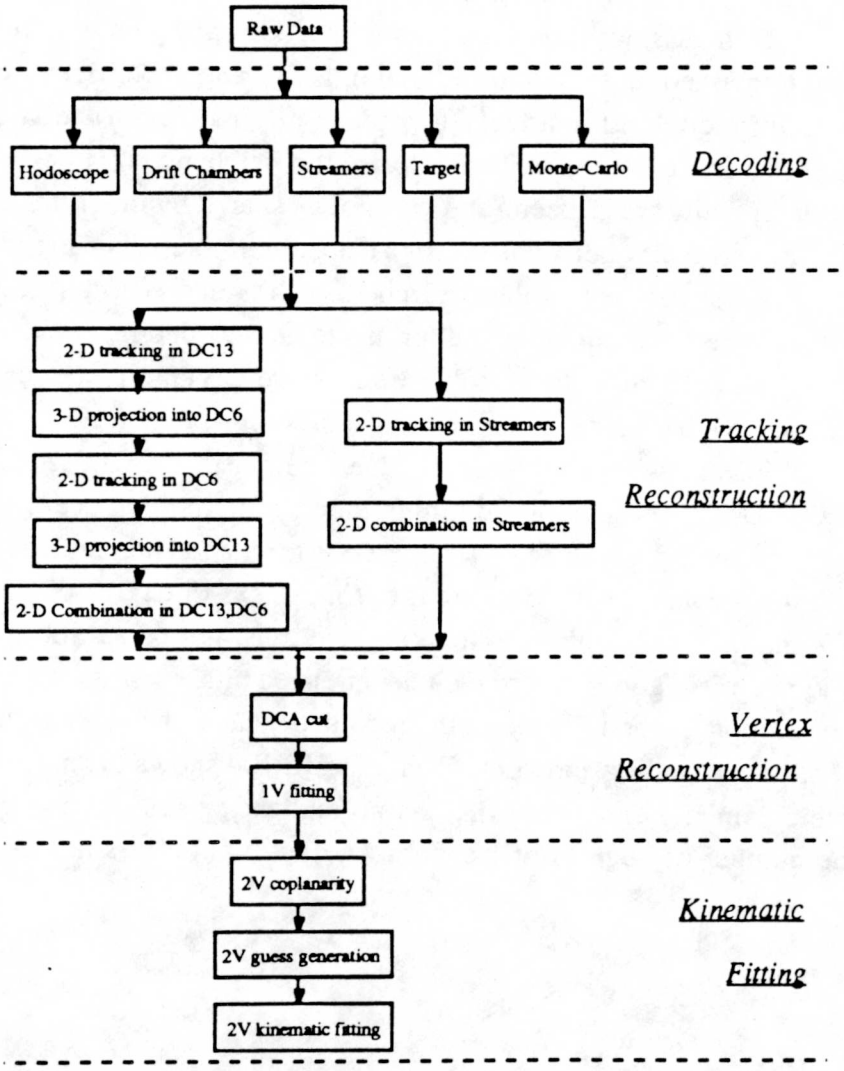

Fig.III.A.2. Flow diagram of the analysis program.

III.B. Track Reconstruction.

The raw data do not have any position information, only wire numbers, drift times (drift chambers) and cluster size (streamers), see section II.A.4 and section II.A.5. While the coordinates for the streamer tube hits are determined uniquely by the wire number information, the generation of drift chamber coordinates requires a calibration of the drift distance as a function of drift time and track angle. This procedure is well defined and can be found in several references (III.DUTTY.88).

Once all coordinates have been generated, the process of reconstructing a two dimensional track (2D track) in the drift chambers and streamers chambers can be separated into the problem of track finding(pattern recognition) and track fitting. In the absence of a magnetic field, the association of the hits to particle track candidates is purely geometrical and will require the set of hits to lie on a straight line. The 2D tracking algorithm consists of several passes. In each pass, we look for tracks with a decreasing number of hits. Three hit tracks are the minimal length tracks considered in DC13 and DC6. Because of the low charged particle multiplicity and relatively low plane efficiencies in the streamers, the remaining streamer hits are further combined to form all possible two hit tracks. If a track is found, its corresponding hits are "frozen" and will not be shared by other tracks. To find a track, all combinations of hits between the most upstream and downstream plane are considered. Each plane in between is then searched for hits in a corridor defined by the starting combination.When searching a plane for hits to be included in a track candidate, a test quantity (TOL2D), defined as the number of standard deviations the hit is from the projection of the track on that plane, is calculated. This is illustrated in Fig.III.B.1. The hit with the lowest TOL2D and within a tolerance value is retained. Fig III.B.2 shows the raw distribution of TOL2D, the vertical lines defining the maximum tolerance used. Once the track is complete, a linear fit with two parameters, slope and intercept, is performed. Fig III.B.3 shows the reduced χ^2 distribution for 7 hit tracks (5 degree of freedom). The cut on TOL2D is the only cut applied in tracking and must not be set too tightly or too loosely in order to not miss "good" hits or include unrelated hits.

The hit resolution (error assigned to the hits) depends on the angle of the track and is important in both track finding and track fitting. Fig III.B.4 shows the hit resolution as a function of angle obtained by requiring that the normalized χ^2 distribution peaks at $\frac{n_f-2}{n_f}$ where n_f is the number of degrees of freedom (a track with n hits has n-2 degrees of freedom).

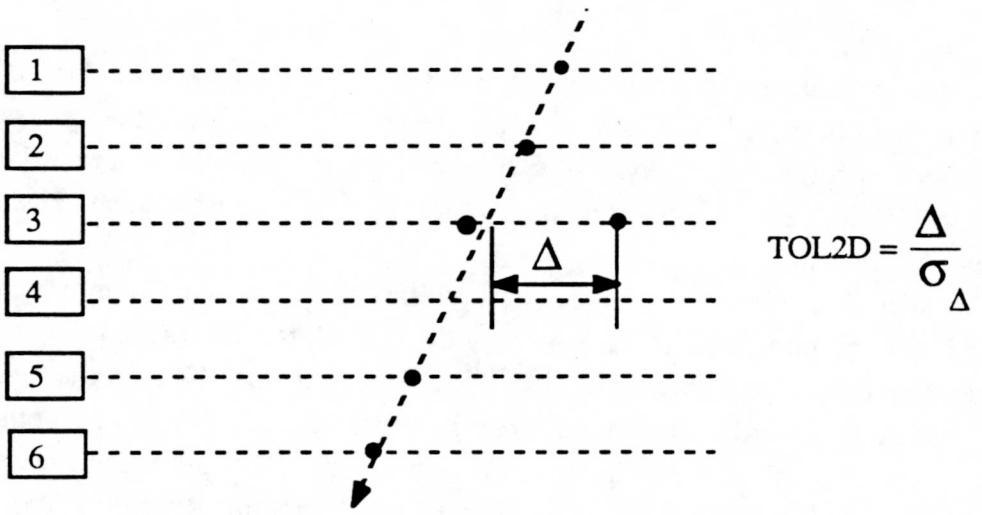

Fig.III.B.1. Two dimensional tracking algorithm.

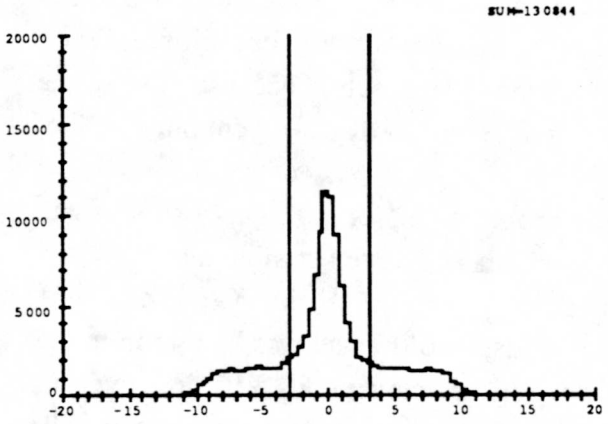

Fig.III.B.2. Raw TOL2D distribution with cut applied on TOL2D during tracking.

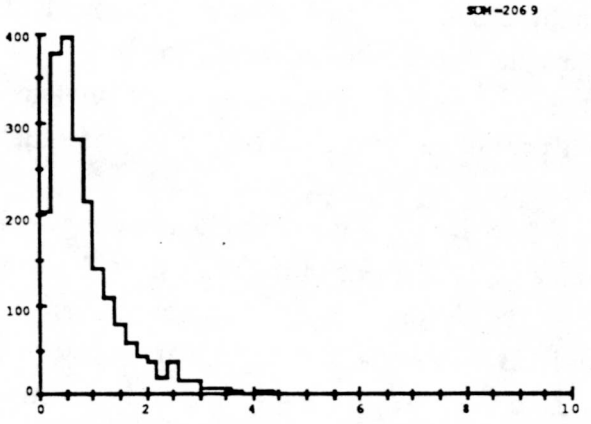

Fig.III.B.3. Reduced χ^2 distribution for seven hit tracks in DC13 (5 degrees of freedom).

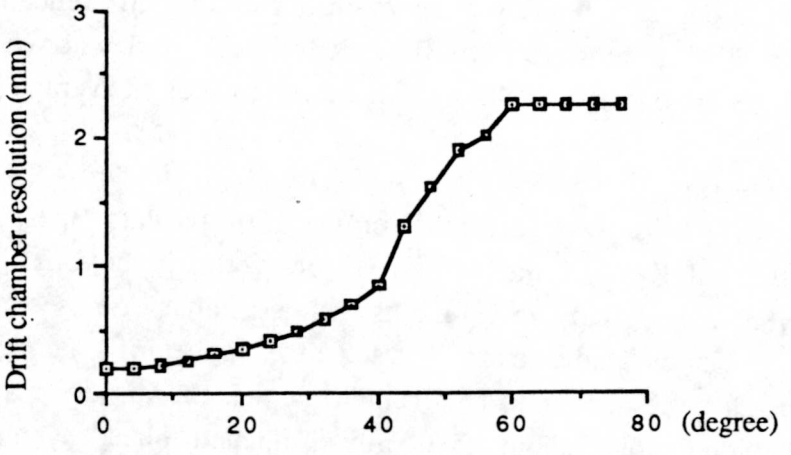

Fig.III.B.4. Error assigned to hits in mm as a function of track angle in degrees.

In order to construct particle tracks in three dimensions (3D track), two dimensional projections must be combined. While this procedure is simple , it does not necessarily always generate the "right" 3D tracks. For example, five particles will generate five 2D tracks in each projection. By combining them, twenty five track pairs must be considered of which only five are real.

In the drift chambers stacks , these ambiguities in the track assignment can be partially lifted by combining the 2D track pairs in DC13 with the 2D tracks pairs in DC6 whose projections (X',Y') are rotated by 14° with respect to the (X,Y) projections in DC13, see Fig.II.A.4b. In order to find the three dimensional tracks shared by both drift chamber stacks, each 3D TRACK pair in DC13 is projected into DC6 and each projection is searched for additional hits with the same two dimensional tracking algorithm. The same procedure is used to track pairs in DC6 (full six hits). They are projected back into the last two X and Y planes of DC13. To make full 3D tracks, the requirement that two hits have to be found in each projection ensures that real tracks are being found. When all shared 3D tracks have been found, the remaining 2D projections are simply combined. Track matching drastically reduces the track ambiguities for the $\Lambda\bar{\Lambda}$ reaction because most of the tracks are in the drift chamber stack. The situation is different for K_SK_S where only 20% of the events are completely in the stack.

While unphysical tracks are not a serious problem per se, too many of them will clutter the later levels of the analysis with unnecessary fits and vertex combinations .

High angle drift chamber tracks have been a concern in the K_SK_S analysis. Fig.III.B.5 shows a typical high angle track event. Clusters of hits start to appear in tracks whose angles are above 40° and come mostly from a non homogeneous drift time over the width of the drift cell. Tracking will then find an average of 4 to 5 "parallel" tracks. The distribution of the time difference (in 1.5 nsec time bins) between the first and second hit in the same cell shows a definite correlation, Fig.III.B.6. If the second hit would be randomly distributed, corresponding to a second real track passing through the same cell, the distribution would decrease linearly as function of the time difference. Second hits, which are less than 50 time bins from the first hit for track angles above 40°, are not considered; this results in no loss in tracking efficiency and yields an average of one to two "parallel" tracks.

First level reduction :

A first level reduction was performed on the 150 raw data tapes. Monte-Carlo simulations show that all K_SK_S events have at least one vertex in the drift chamber stack. Therefore, only events which had two 3D tracks with a distance of closest approach less than three standard deviations and an extra 3D track either in the drift chamber stack or the streamer tube barrels were retained. This reduction, which was done at CERN and amounted to a reduction factor of about 4.5, mainly eliminated "blank" events (no tracks) , straight through events (one track) and single vertex events (elastics).

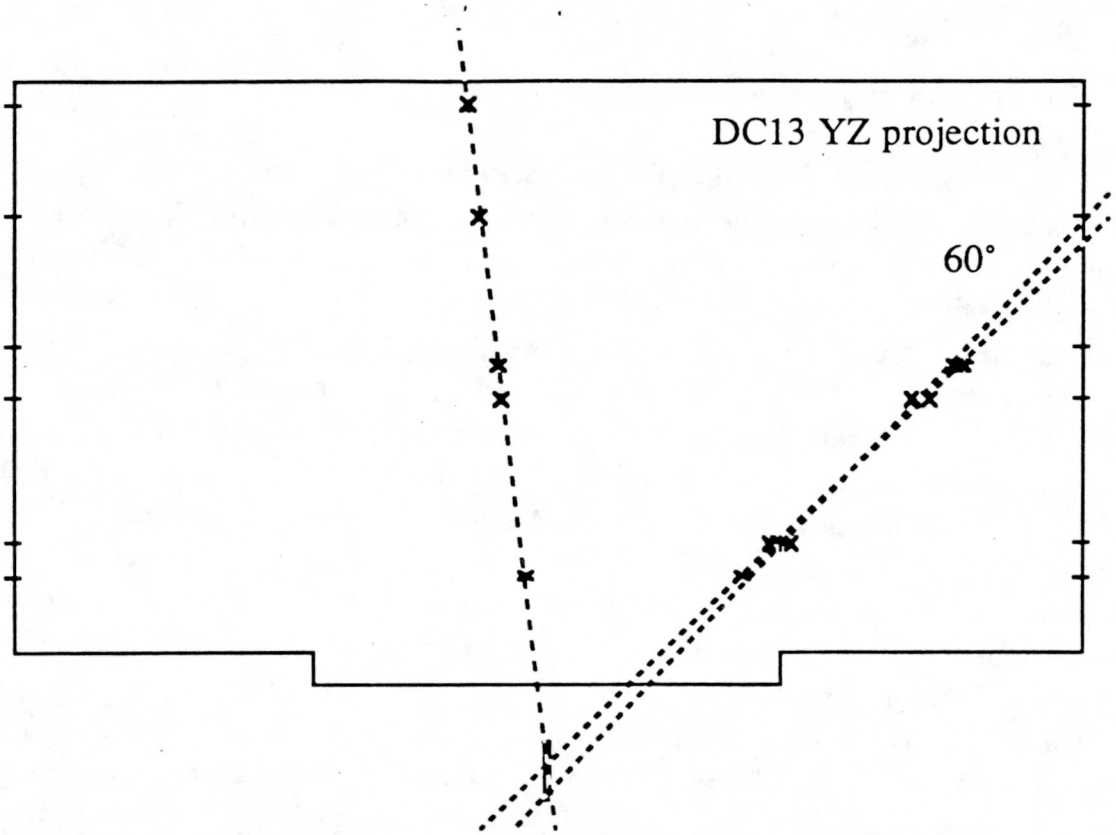

Fig.III.B.5. Typical high angle track in DC13 (Y projection).

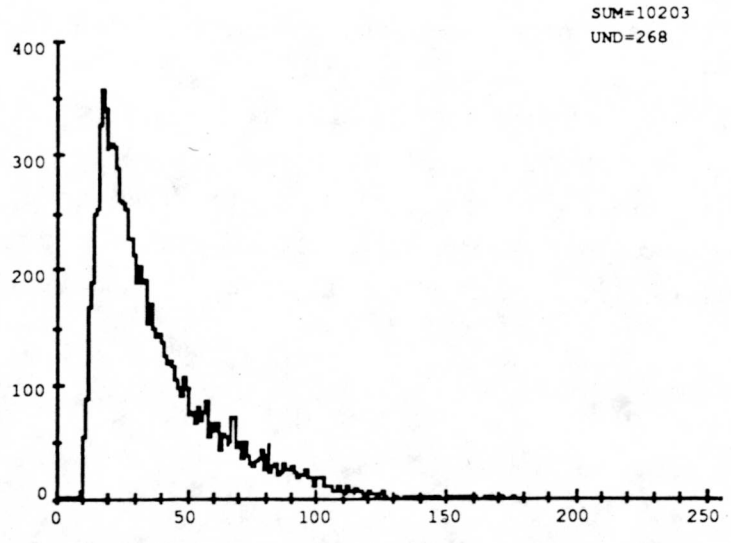

Fig.III.B.6. Distribution of the time difference between the first and second hit when both belong to the same drift cell (one bin = 1.5 ns)

III.C. Vertex Reconstruction.

Now that all possible three dimensional tracks have been found, the next step is to look for decay vertices whose plane must intercept the target, see Fig.III.C.1. This signals that a neutral particle moving away from the target (including a K_S or a Λ) has decayed into two charged particles.

Any pairs of three dimensional tracks whose distance of closest approach (DCA) is less than eight standard deviation defines a vertex candidate. Fig.III.C.2a shows the raw distribution of the distance of closest approach divided by its error (TOLDCA).

Once a vertex candidate has been found, it must be fitted with a vertex constraint. The χ^2 is minimized in a seven parameter space, Fig.III.C.1. For vertices entirely in the drift chamber stack, the χ^2 is quadratic in all parameters except in the Z coordinate of the vertex point. The χ^2 can then be numerically minimized along that parameter. However, vertex candidates with one or both of their arms in the streamers must undergo a full non-linear time consuming minimization.

The χ^2 distribution for the vertex fits is shown in Fig.III.C.3. Retaining vertices with $\chi^2 < 5$ allows one to set a "speed" cut on the distance of closest approach as seen in Fig.III.C.2b where TOLDCA for $\chi^2 < 5$ is shown. By requiring TOLDCA < 8 , no vertex with $\chi^2 < 5$ is lost while the number of combinations to be fitted is reduced by 30%.

Most of the vertices found in Fig.III.C.3 have their intersection point very close to the target region. These vertices are mostly charged particles which passed through the neutral trigger and also neutral particles decaying very close to the target (especially K_S) . For that reason, they can not be discarded even though they create a non-negligible number of vertex candidates. For example, suppose that four charged particles leave the target region. Of the eight two dimensional tracks generated, sixteen 3-D tracks will be reconstructed of which 25 good vertices will be fitted.

Therefore, in order to define a resonable reduction, a $\chi^2 < 5$ cut is not enough. Another more stringent requirement is necessary.

Another consequence of having a high number of vertices coming from the target, the requirement that the decay vertex plane intersects the target, while more effective for the Λ case, proved to be useless in the K_S case and was not used.

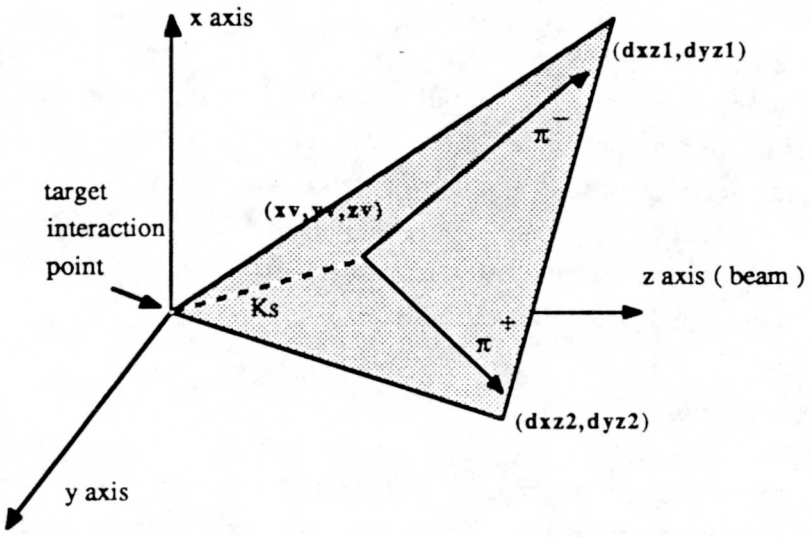

Fig.III.C.1. Vertex generated by a neutral decay.The plane defined by the vertex intersect the target. (xv,yv,zv,dxz1,dyz1,dxz2,dyz2) are the seven parameters used in the vertex fit.

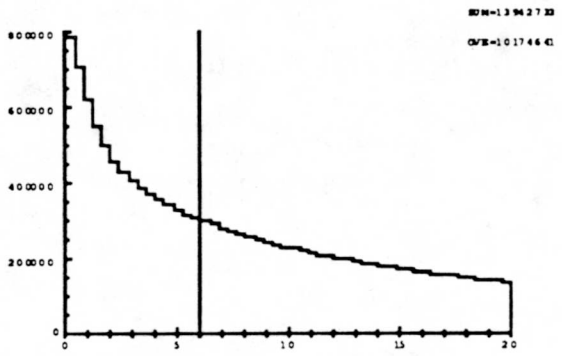

Fig.III.C.2a. Raw distribution of TOLDCA defined as the distance of closest approach divided by its error and the corresponding cut applied.

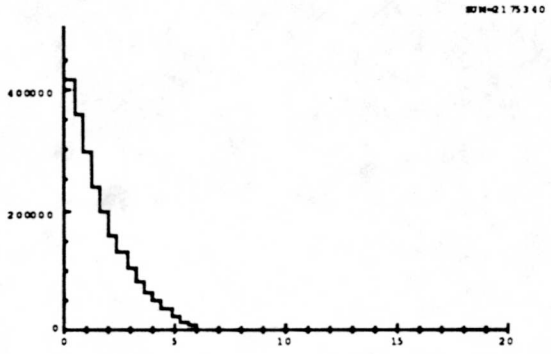

Fig.III.C.2b. TOLDCA distribution for vertices with $\chi^2 < 5$.

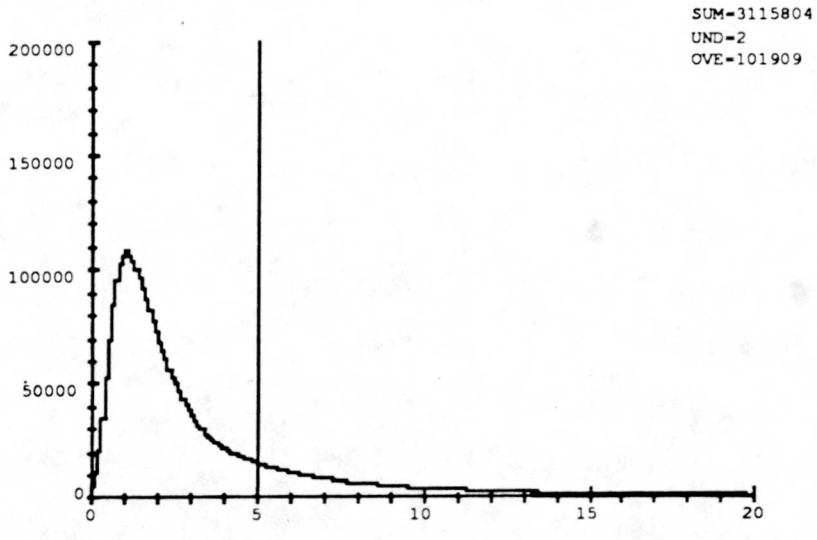

Fig.III.C.3. Reduced χ^2 distribution from the vertex fits with corresponding cut set at 5.

As mentioned before, the $\bar{p}$ p ->$K_S K_S$ and $\bar{p}$ p -> $\bar{\Lambda}$ Λ reactions are two body reactions. In other words, the $\bar{p}$ beam should be coplanar with the directions of the two neutral particles defined by the two vertex intersection points and the target, see Fig.III.4.a. Therefore, both decay vertex positions when projected in the direction of the beam must be collinear with the target, Fig.III.C.4b. Again, a quantity, TOLCOP, is defined as the distance from the target to the line joining the vertex points divided by its corresponding error. Fig.III.C.5 shows the TOLCOP distribution.

Second level reduction:

The second stage reduction (2V COPLANAR) was then performed keeping events having at least one vertex pair with TOLCOP < 2 and yielded an average reduction ratio of 4.2 . This TOLCOP cut was set wide enough so that no $K_S K_S$ and $\bar{\Lambda}$ Λ event were lost for the next reduction stage of the analysis.

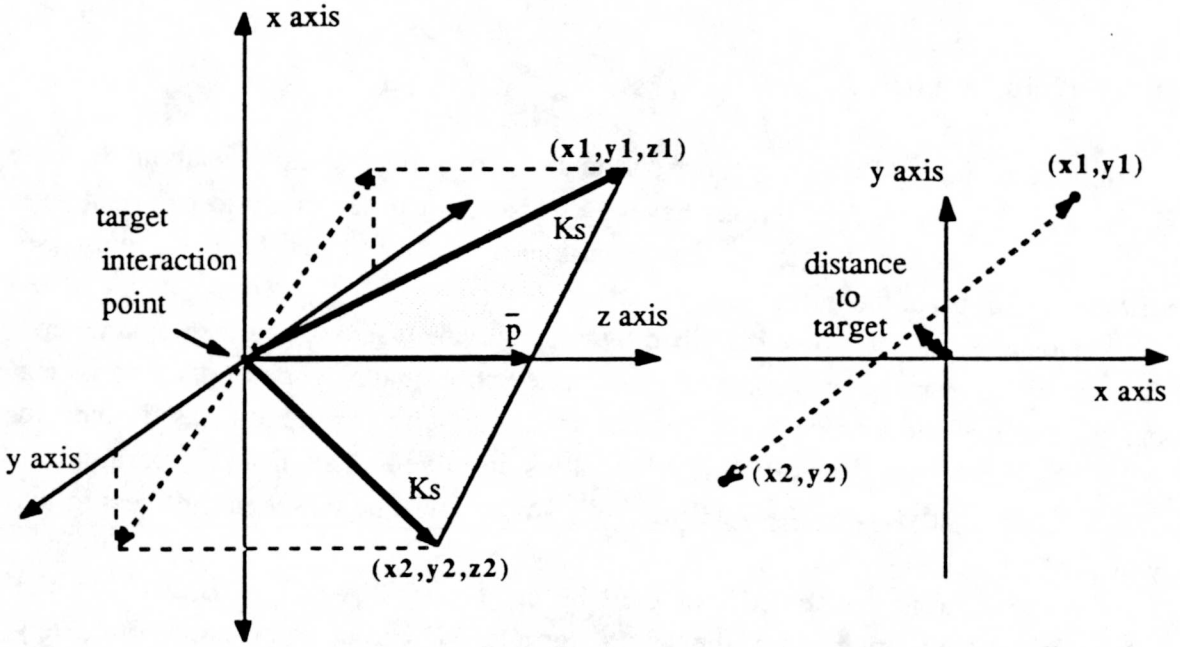

Fig.III.C.4. The $\bar{p}$ is coplanar with the two neutral particles. Projected along the beam(left), TOLCOP is the distance from the target to the line joining the vertex points divided by its corresponding error.

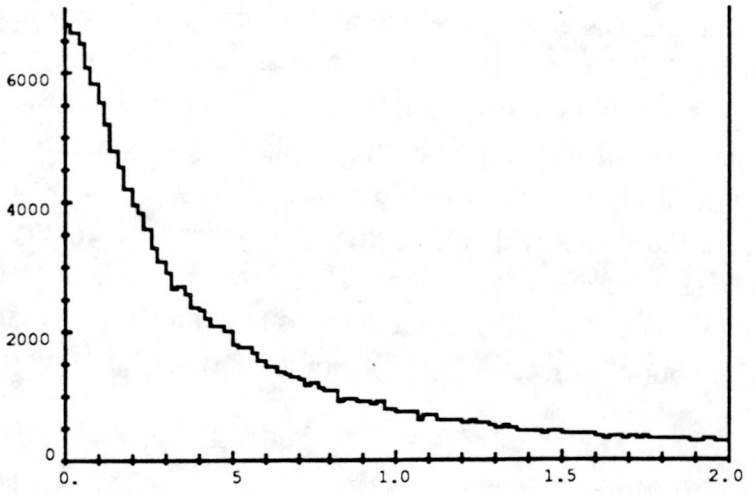

Fig.III.C.5. Raw distribution of TOLCOP with the corresponding cut applied at two.

III.D. Kinematic Fitting.

In the tracking and vertex reconstruction part, no direct assumptions about the $\bar{p}\ p \rightarrow K_S\ K_S$ and $\bar{p}\ p \rightarrow \bar{\Lambda}\ \Lambda$ reactions have been made. In order to try to extract these reactions from the reduced data, all combinations of vertices must be fitted with the kinematical constraint of the three 2-body reactions.

A two vertex event can be discribed by two equivalent sets of fourteen parameters. The first set (vertex parameters) consists of the vertex coordinates (vertex point and vertex slopes) for each of the vertices. The second set (kinematic parameters) as defined in Table.III.1 follows more closely the kinematics involved. The last six parameters (x_{int},y_{int},z_{int},dx_{beam},dy_{beam},p_{beam}) define the beam and will be of special interest in the study of the K_S reaction.

The kinematic constraint can then be seen as follows, Fig.III.D.1 : in the laboratory frame, the momentum of the neutral particle (P2) can be determined completely from the polar angles (θ_4,θ_5) of the decay products with respect to the direction of the neutral particle. This momentum (P2) must also agree with the momentum determined from the anti-proton beam (PBEAM) and the neutral particle polar angle (θ_2). The same constraint applies to the second vertex.

As for the vertex reconstruction process, the kinematic fitting consists of two main parts:

First , from the set of tracks obtained from the vertex fit, an initial guess to the kinematic parameters must be found. We want to see if the kinematic constraint is obeyed by the vertex combination. The effectiveness of this constraint will depend on the quality of the tracks (detector resolution) and the determination of the target to vertex direction (θ_2 or θ_3). For example, when a particle decays in the target region, as most of the K_S do, the determination of the neutral particle laboratory polar angle is much harder. Thus, the application of the kinematic constraint as illustrated above is not as valuable. In order to correct for this effect, the vertex which is further away from the target (primary vertex) is used to determined the laboratory polar angle of the second particle (secondary vertex). This allows a more meaningful application of the constraint and improves the K_S acceptance by about 20%. When both vertices originate from the target region, no reasonable guess can be made.

Table.III.D.1

Kinematic parameters definition	
$\theta_{2cm}, \varphi_{2cm}$	Polar and azimuthal angle of one of the neutral particle (K_s or Λ) in the $\bar{p}$ p rest frame.
$\theta_{4cm}, \varphi_{4cm}$	Polar and azimuthal angle of one of the decay particles (p or π) in the first neutral particle rest frame (PRIMARY VERTEX).
$\theta_{6cm}, \varphi_{6cm}$	Polar and azimuthal angle of one of the dcay particles (p or π) in the second neutral particle rest frame (SECONDARY VERTEX).
r_2, r_3	Laboratory decay distance of both neutral particles.
$x_{int}, y_{int}, z_{int}$	$\bar{p}$ p interaction point in target.
dx_{beam}, dy_{beam}	Slopes of the beam in the x and y projection.
p_{beam}	Beam momentum.

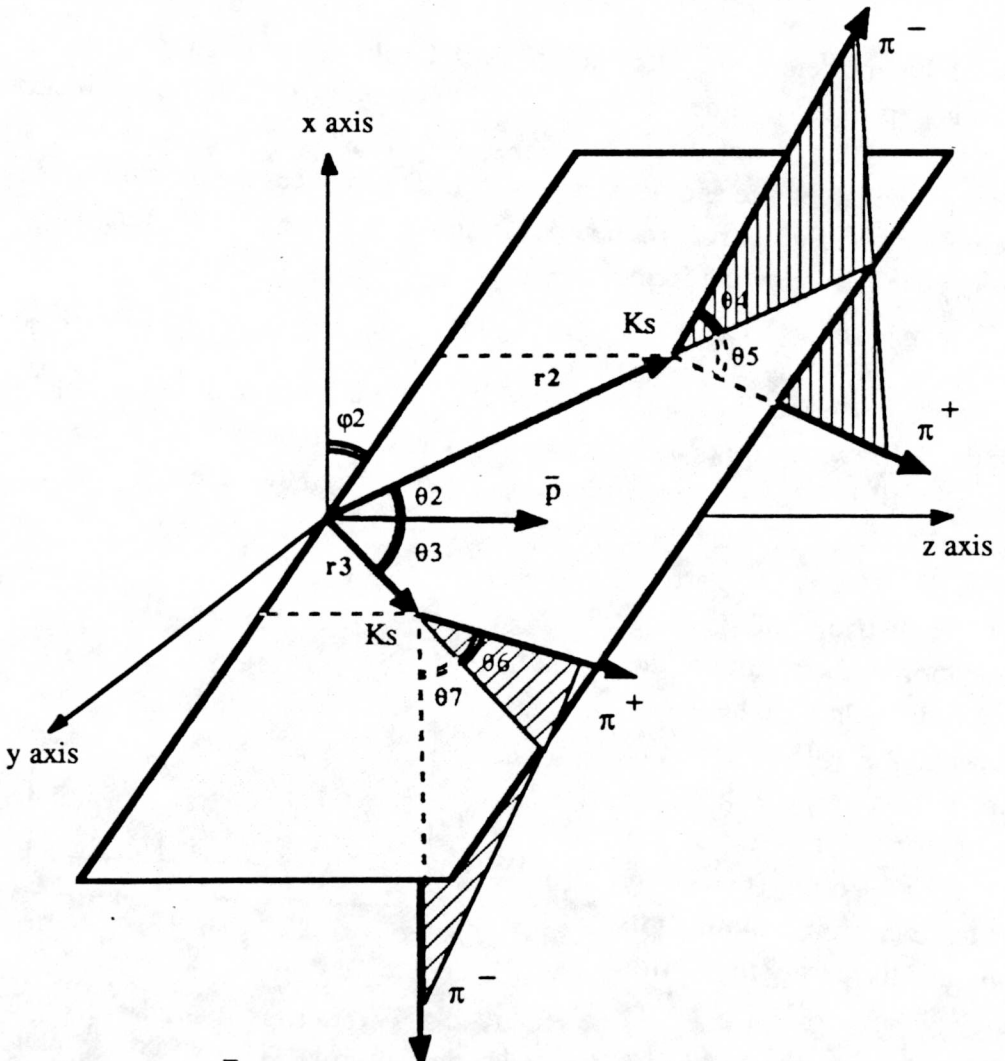

Fig.III.D.1. Full reaction $\bar{p}\,p \rightarrow Ks\ Ks \rightarrow \pi^+\pi^-\ \pi^+\pi^-$ when the direction of the beam is assumed colinear to the z axis.

In the second part, the corresponding vertex parameters are found from the initial kinematic parameters and used to calculate the predicted coordinates at each of the planes. By comparing the predicted and measured coordinates, a χ^2 is calculated according to the formula

$$\chi^2 = \sum_{i=1}^{n} \frac{1}{\sigma_i^2} [\, x_i - f_i(\theta_{2cm}, \varphi_{2cm}, \ldots\ldots p_{beam}) \,]^2$$

where n is the total number of planes with hits belonging to the vertex combination, x_i and σ_i^2 are the measured coordinate and the assigned error at plane i and f_i is the predicted coordinate corresponding to a specific set of kinematic parameters. By varying these parameters until a minimum for χ^2 is found, the most probable parameters are determined and the final reduced χ^2 is then a measure of the goodness of the fit of the tracks to the reaction.

Not all parameters are allowed to vary freely. The magnitude of the beam momentum is kept fixed (χ^2 depends only weakly on p_{beam}). Also the production point ($x_{int}, y_{int}, z_{int}$) and the beam direction (dx_{beam}, dy_{beam}) can only vary within limits consistent with the target size and beam divergence. This reduces the possibility of extreme values being assigned to these parameters. To implement these conditions, a penalty is added to the χ^2 in the following form

$$\chi^{2'} = \chi^2 + \chi_p^2(x_{int}) + \chi_p^2(y_{int}) + \chi_p^2(dx_{beam}) + \chi_p^2(dy_{beam})$$

where $\chi_p^2(x_{int})$ is defined in Fig.III.D.2. Δx_{int} is the range around the nominal value of the beam dx_{int}^n for which no penalty is applied. The three other penalties are defined the same way. Fig.III.D.3 shows the distributions obtained from the kinematic fitting of the $\bar{p}$ p -> $\bar{\Lambda}$ Λ at 1567 MeV/c for the four parameters of interest. The narrow width of the distributions gives a good indication of the quality of the kinematic fitting. On the other hand, as seen in Fig.III.D.4, the distributions from the $\bar{p}$ p -> K_S K_S analysis (for all momenta) are much wider and imply that more care has to be taken in handling this reaction, as discussed in section IV.F.1.

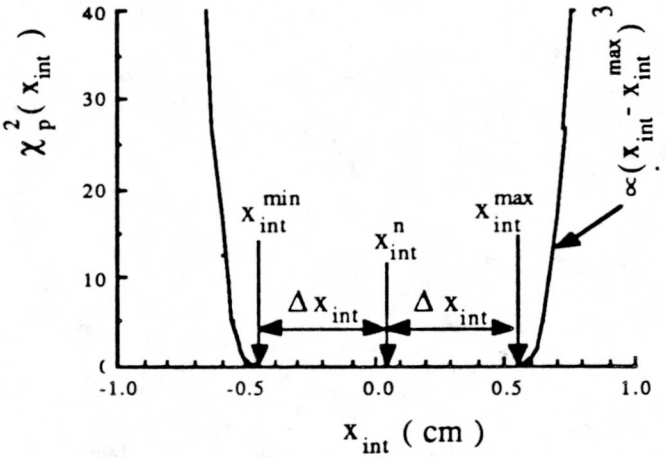

Fig.III.D.2. χ^2 penalty as a function of x_{int} where Δx_{int} is the range around the nominal value x_{int}^n of the beam for which no penalty is applied.

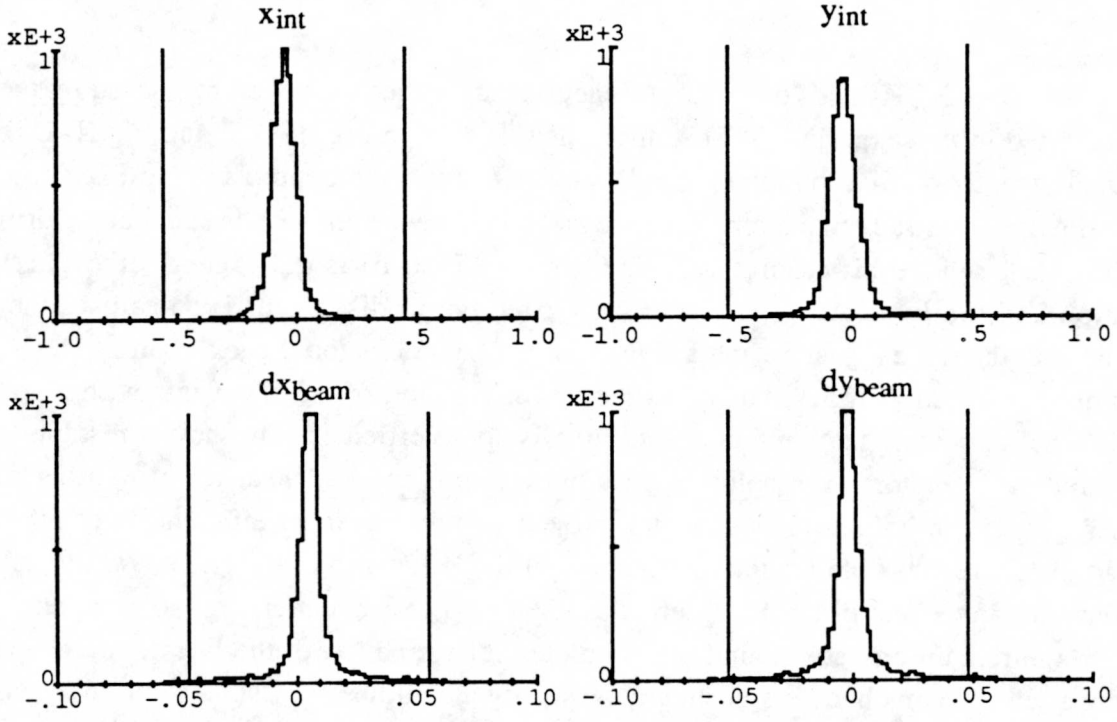

Fig.III.D.3. Interaction point (x_{int},y_{int}) and beam direction (dx_{beam},dy_{beam}) distributions from the $\bar{p}$ p -> Λ Λ analysis at 1567 MeV/c with wide penalties (vertical lines).

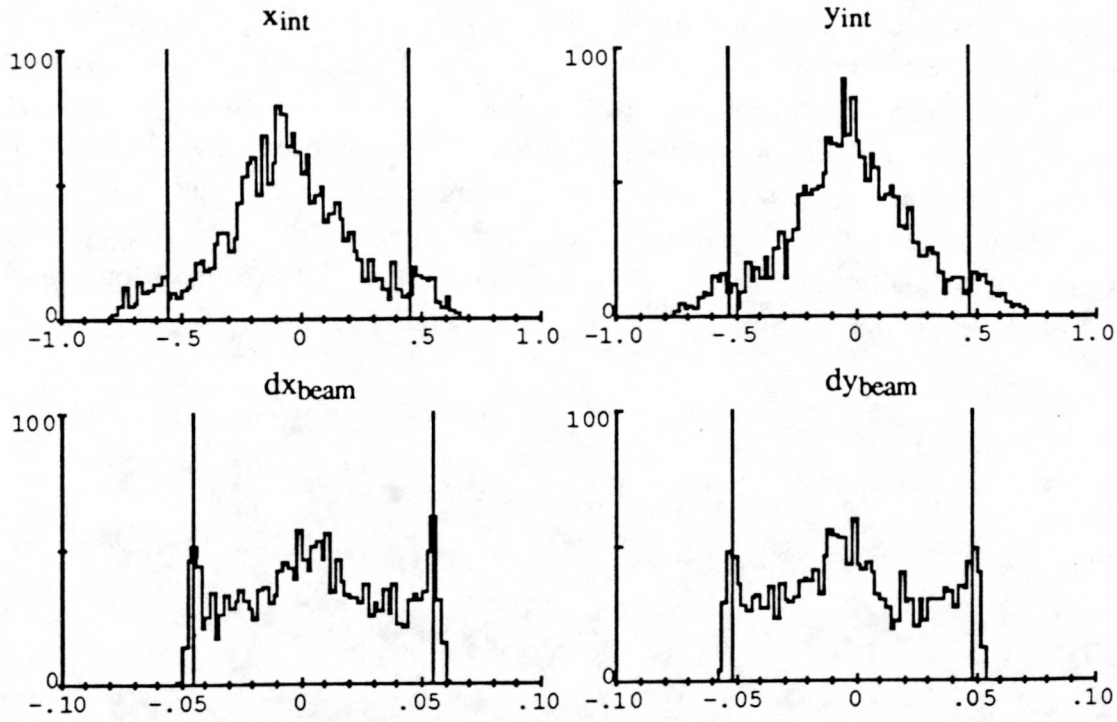

Fig.III.D.4. Interaction point (x_{int},y_{int}) and beam direction (dx_{beam},dy_{beam}) distributions from the $\bar{p}$ p -> K_S K_S analysis with wide penalties (vertical lines).

The $\bar{p}\,p \rightarrow K_S\,K_S$ and $\bar{p}\,p \rightarrow \bar{\Lambda}\,\Lambda$ reactions are not equally well measured by the apparatus used in this experiment. This difference is seen in Fig.III.D.5 and Fig.III.D.6. In the first case the χ^2 distribution of the $\bar{\Lambda}\,\Lambda$ events shows no appreciable tail. Because the $\bar{\Lambda}$ and Λ are constrained in a forward cone and therefore are entirely detected in the drift chamber stack whose hit resolution (~200μm to ~500μm) is quite good, the guess generation and the kinematic fitting are very effective in discriminating against other reactions with the same signature and against unwanted combinatorial background. The K_S case is quite different. Fig.III.D.6 shows the χ^2 distribution of the K_S events with a non negligible tail indicating that the kinematic fitter is not as efficient . The lack of resolution of the streamer detector (hit resolution of about 0.5 cm) and the insufficient number of streamer barrels (only three planes in each projection with average efficiencies of 80 to 90%) are partly responsible for the inefficiency of the kinematic analyser. But, above all, the discriminating effect of the K_S kinematics itself is not stringent enough to completely eliminate the remaining background. A complete determination of the beam parameters given by a set of beam chambers upstream of the target could be a possible solution to this problem.

The K_S χ^2 distribution shown in Fig.III.D.6 has already been improved by a series of cuts to partially correct for tracking deficiencies, mainly for wrong assignments of two dimensional track projections to the vertex combination arms. First, the hodoscope is used to require that any three dimensional track which intersects the hodoscope does have a hit within ±2 cm of the track projection in both planes of the hodoscope. Also, a K_SK_S event found to have an extra two dimensional track with at least five hits and coming from the target region are discarded. Finally, only K_SK_S events with $\pi^+\pi^-$ opening angles > 23° are kept. This cut eliminates events with small $\pi^+\pi^-$ opening angles which results mainly from a failure to match three dimensional tracks between the two drift chamber stack . These events are kinematically possible but not very probable (only 3% of the Monte-Carlo generated K_SK_S events) as seen in Fig.I.D.2d.

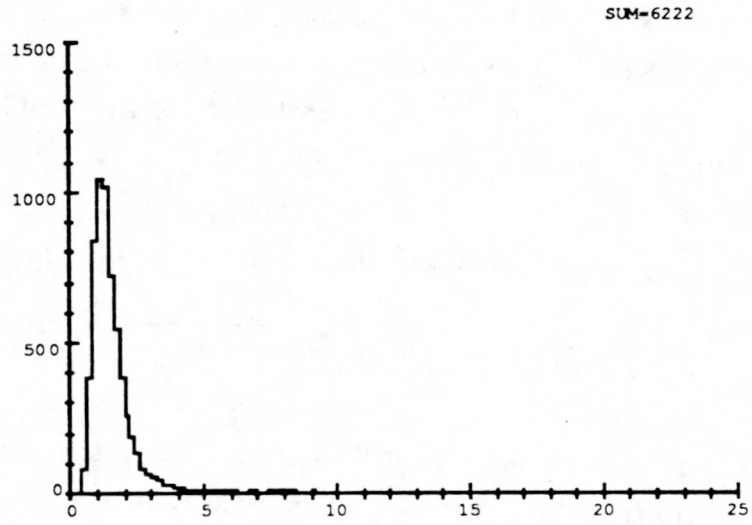

Fig.III.D.5. Reduced χ^2 distribution for $\bar{\Lambda}\,\Lambda$ events at 1567 MeV/c (wide penalties).

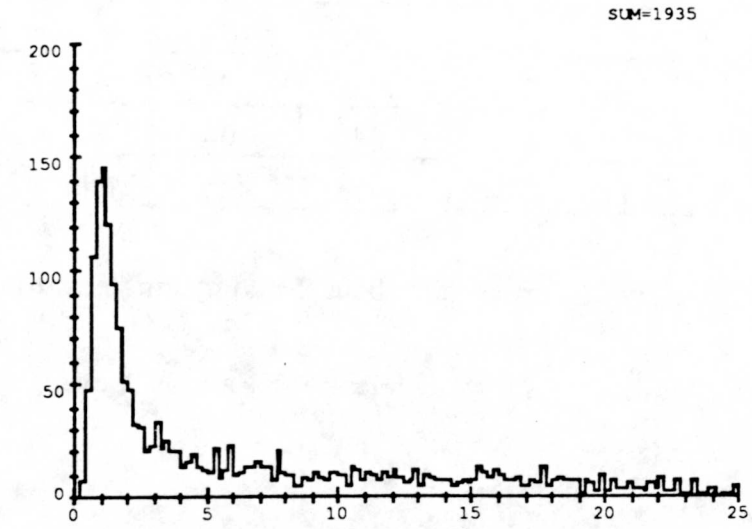

Fig.III.D.6. Reduced χ^2 distribution for $K_S\,K_S$ events for all momenta (wide penalties).

Third level reduction:

The third stage reduction (wide penalty kinfit) involved keeping only events with $\chi^2 < 25$ and with a loose χ^2 penalty setting of five, as explained in Table.III.D.1. This final reduction stage amounts to about 2000 K_sK_s events and 10000 $\bar{\Lambda}\ \Lambda$ events.

All subsequent K_sK_s and $\bar{\Lambda}\ \Lambda$ results are obtained from a final pass of the analysis program with the beam penalty setting of two (tight penalty kinfit). The justification of such a penalty setting will be explained in section IV.F.1

Table.III.D.1

Penalty Settings

Definition of the different penalty settings used in the K_sK_s and $\bar{\Lambda}\ \Lambda$ analysis where Δx_{int}, Δy_{int}, Δdx_{beam}, Δdy_{beam} are the ranges around the nominal values of the beam parameters x^n_{int}, y^n_{int}, dx^n_{beam}, dy^n_{beam} for which no penalty to the χ^2 is applied.

Penalty setting	Δx_{int} (cm)	Δy_{int} (cm)	Δdx_{beam}	Δdy_{beam}	
0	0	0	0	0	Fixed beam
1	.1	.1	.01	.01	
2	.2	.2	.02	.02	Final analysis pass
3	.3	.3	.03	.03	
4	.4	.4	.04	.04	
5	.5	.5	.05	.05	Third level reduction

In Appendix F are given more details about the computing effort involved in the data analysis.

Fig.III.D.7 and Fig.III.D.8 show a typical K_sK_s and $\bar{\Lambda}\ \Lambda$ event after kinematic fitting.

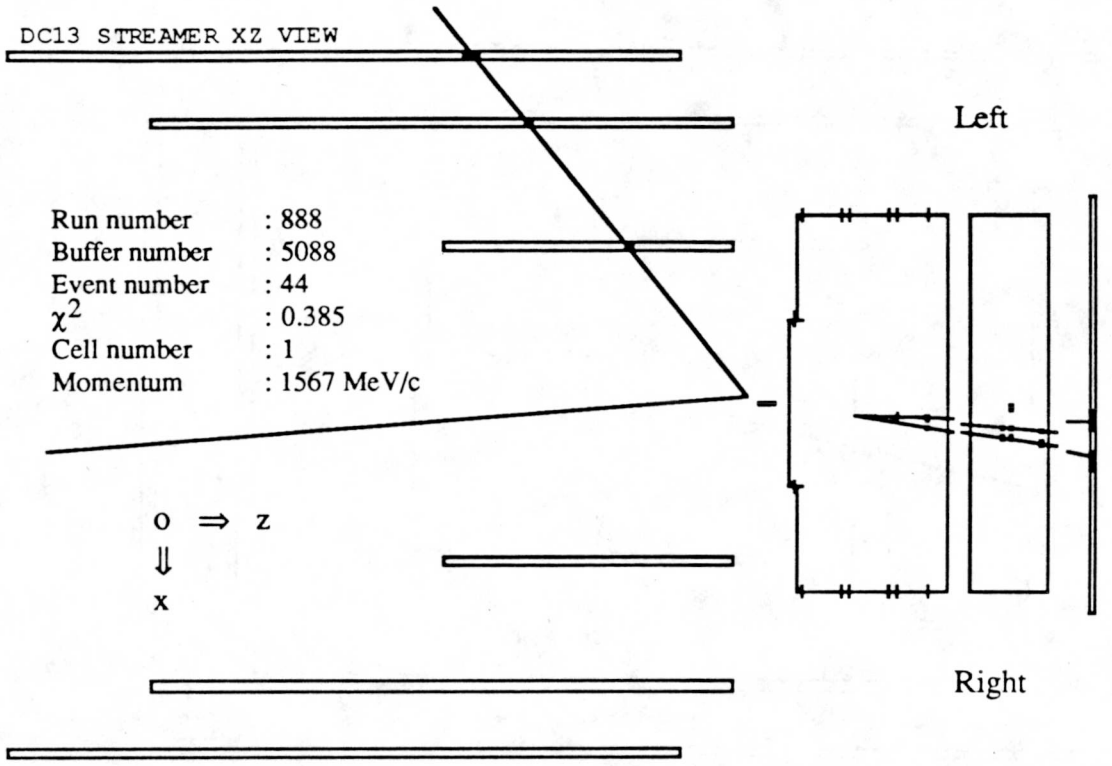

Fig.III.D.7a. Detector top view of a K_SK_S event with one vertex completely in the streamer barrels.

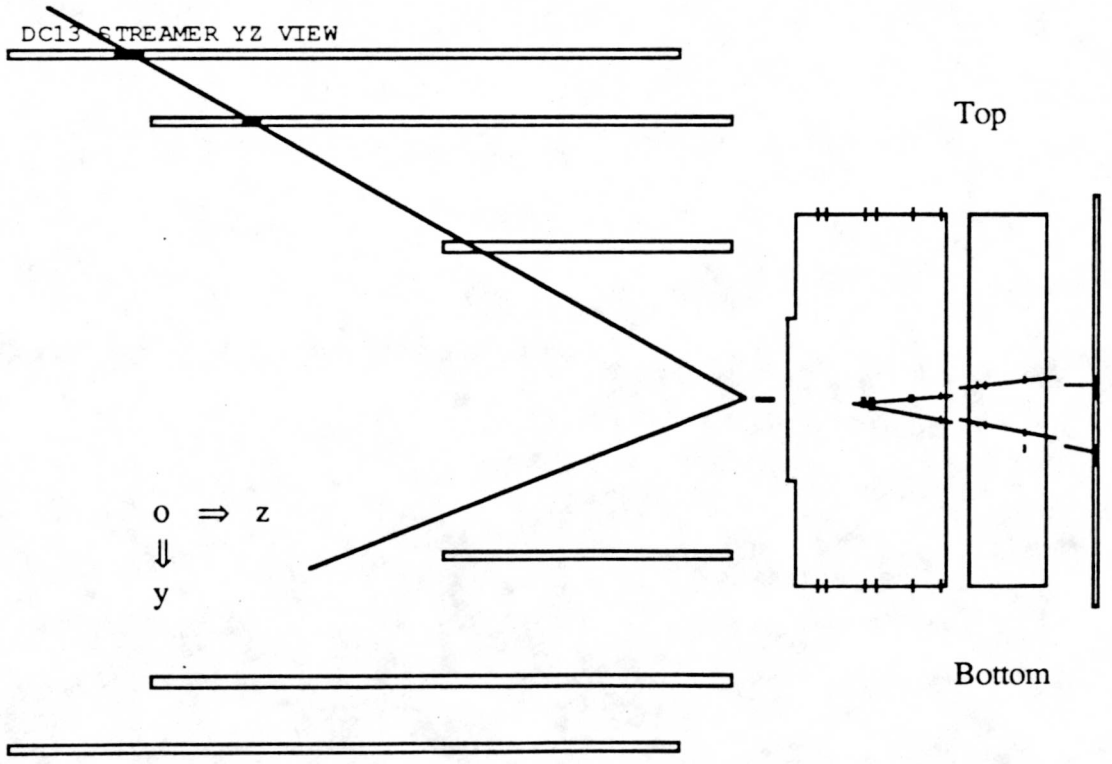

Fig.III.D.7b. Detector side view of a K_SK_S event with one vertex completely in the streamer barrels.

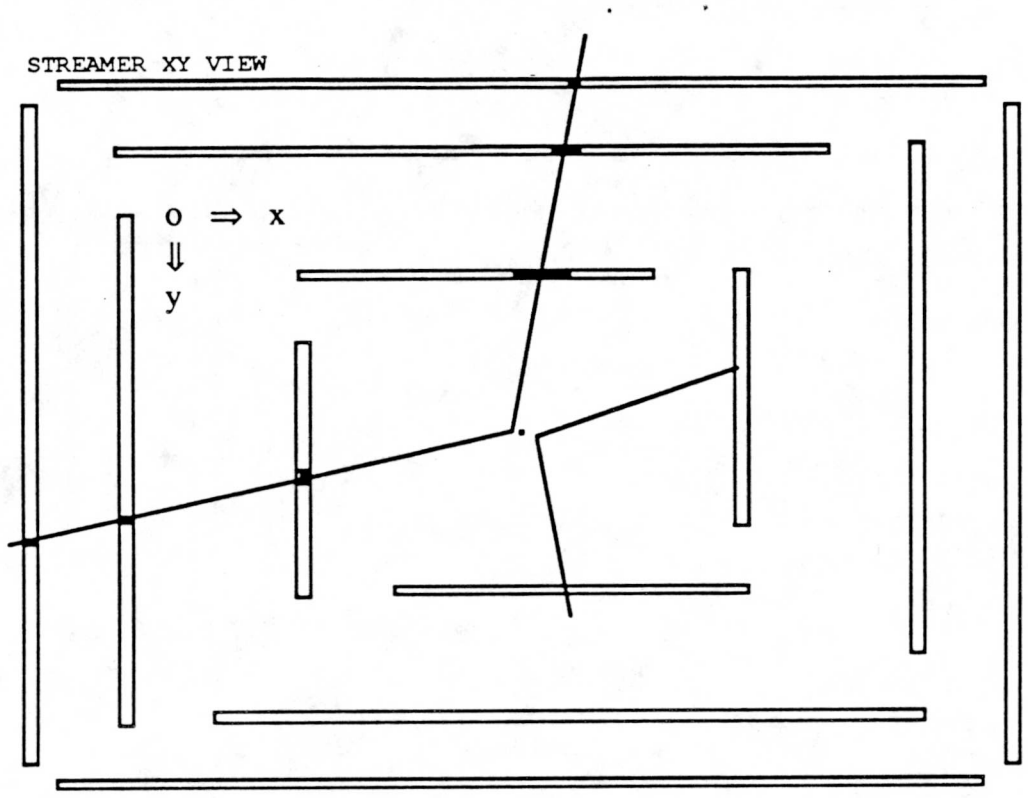

Fig.III.D.7c. Detector view in the direction of the beam of a $K_S K_S$ event with one vertex completely in the streamer barrels.

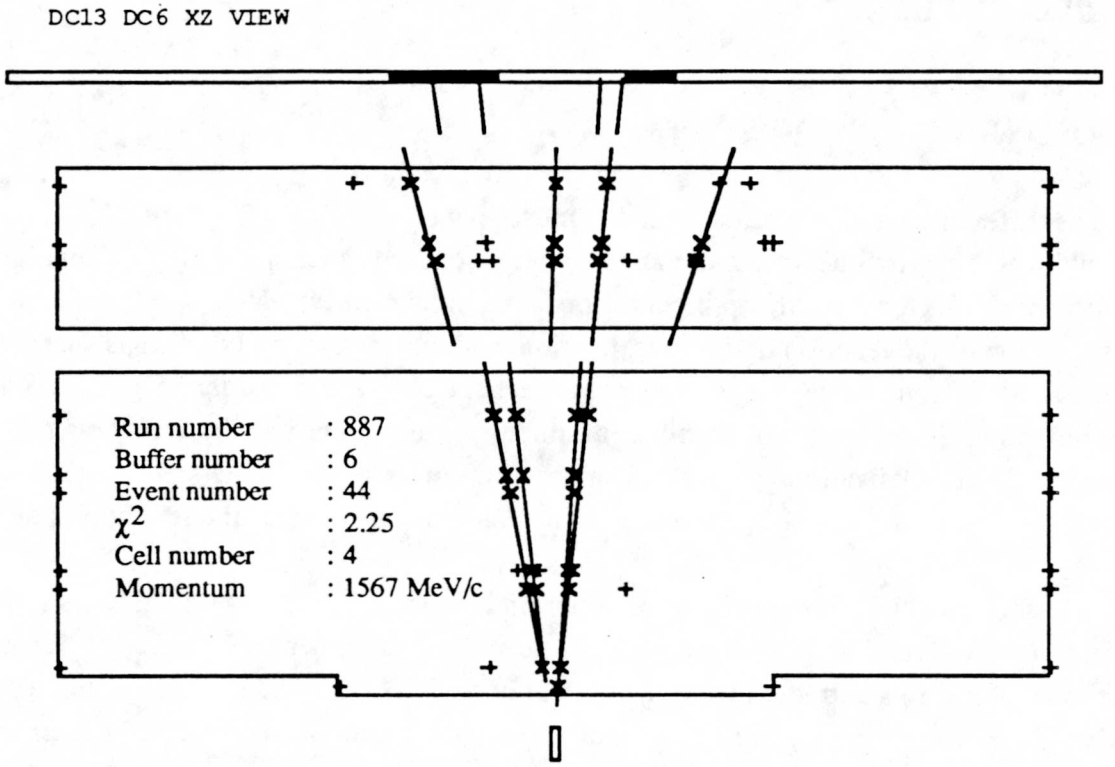

Fig.III.D.8a. Detector top view of a $\bar{\Lambda}\,\Lambda$ event.

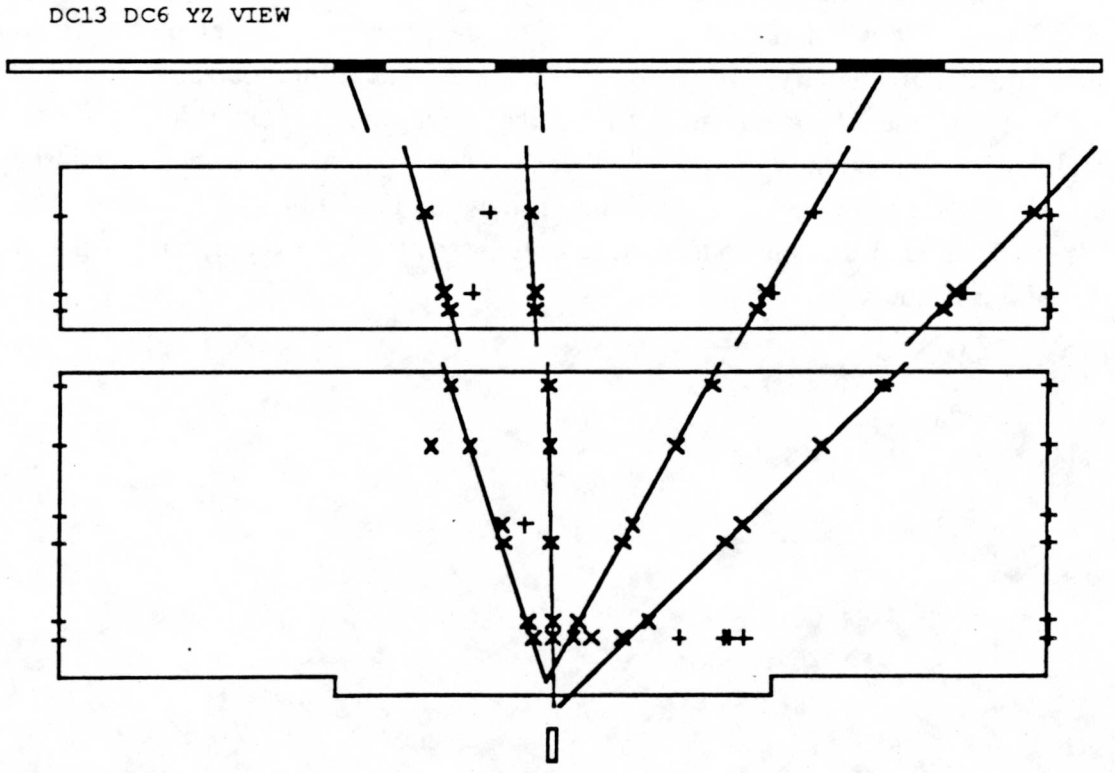

Fig.III.D.8b. Detector side view of a $\bar{\Lambda}\,\Lambda$ event.

IV. Normalization.

IV.A. Overview.

The differential and total cross sections must now be calculated from the K_SK_S and $\bar{\Lambda}\Lambda$ events which passed the kinematic analysis, as discussed in Chapter III. The angular distribution of the K_S (or Λ) in the $\bar{p}$ p center of mass, shown in Fig.IV.A.1, reflects both the cross section of the reaction under investigation and our measuring conditions such as the beam flux, detector acceptance, and possible backgrounds. In order to generate a differential cross section as an absolute number, the angular distribution must be normalized. The normalization procedure is a very important and delicate step in the data analysis and requires a good understanding of the detector response to the reaction under study.

The normalization procedure can be better understood if we look at the definition of the differential cross section for the $\bar{p}\ p \rightarrow K_SK_S$ reaction. As shown in Table.IV.A.1, the number of K_SK_S events extracted from the data at one of the momentum settings and at a particular cell is directly proportional to the differential cross section. Therefore, in order to determine the differential cross section, the angular distribution must be normalized for the integrated antiproton flux and the number of protons in the target (beam flux and target correction). Then, the detector acceptance must be taken into account and requires a Monte-Carlo simulation of the reaction to determine the response of the detector (detector acceptance correction). Finally, sources of background (background correction) must be subtracted including the carbon contamination of the target (the CH_2 target has two proton for one carbon atom) and other possible reactions which were not discriminated against by the analysis as hinted at by the K_S χ^2 distribution shown in Fig.III.D.6.

These three contributions to the normalization are now studied in more detail in the remainder of this chapter.

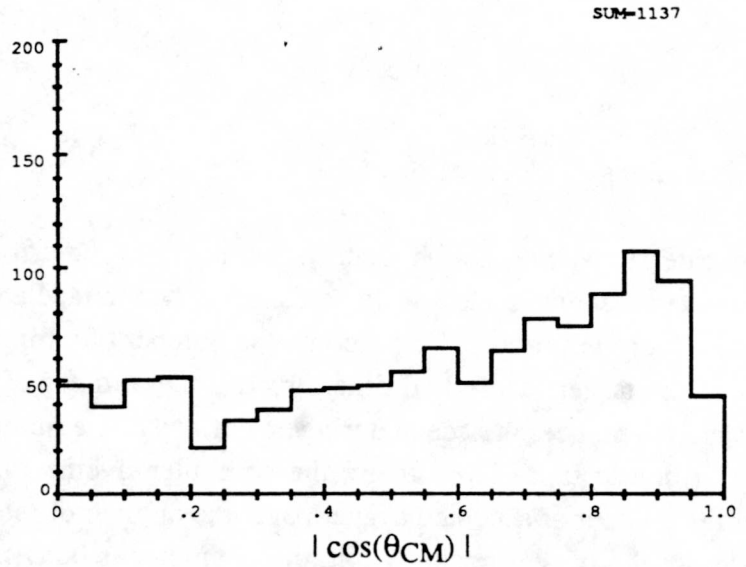

Fig.IV.A.1. Raw K_s angular distribution in the $\bar{p}$ p center of mass as a function of $|\cos(\theta_{CM})|$ for events with $\chi^2 < 5$ and summed over all momenta and cells.

Table.IV.A.1.

Differential Cross Section Definition		
$N_{KsKs}(ib,ic,im) = 2\pi \cdot \Delta_b \cdot \frac{n\,\bar{p}\,(im)}{f_c(ic,im)} \cdot n_{CH2} \cdot dl_{cell}(ic) \cdot \varepsilon_c \cdot \varepsilon_L(im) \cdot \varepsilon_d(ib) \cdot \left\{ \frac{d\sigma(ib,ic,im)}{d\Omega} + \frac{d\sigma_{back}(ib)}{d\Omega} \right\}$		
$N_{KsKs}(ib,ic,im)$		Number of KsKs events extracted from data at the momentum setting im , the cell position ic and the bin number ib in the center of mass distribution Δ_b is the bin width of the distribution.
Beam flux and target correction	$dl_{cell}(ic)$	Cell length in cm
	n_{CH2}	Number of target proton per cm^3
	$n\,\bar{p}\,(im)$	Integrated beam flux on the first cell
	$f_c(ic,im)$	Beam flux correction factor for each cell
Detector acceptance correction	$\varepsilon_d(ib)$	Apparatus and reconstruction acceptance
	$\varepsilon_L(im)$	Computer live time
	ε_c	Branching ratio to four charged particles (.470 for $K_SK_S \rightarrow \pi^+\pi^-\pi^+\pi^-$, .412 for $\bar{\Lambda}\,\Lambda \rightarrow \bar{p}\,\pi^+ p\,\pi^-$)
Systematic corrections	$\frac{d\sigma_{back}(ib)}{d\Omega}$	Background contribution to the differential cross section

IV.B. Beam Flux and Target Correction.

The raw data written to tape do not only consist of hits from the drift chamber and streamer detector. Every ten seconds, scalers were read and written to tape amidst the data. Three of these scalers are very important . One records the number of antiprotons passing through the first cell of the target, while two others record the number of total triggers found by the detector and the number of accepted triggers defined as the number of triggers which were actually written to tape. From them, the computer livetime $\varepsilon_L(im)$ can be defined as the ratio of the number of accepted triggers over the number of total triggers and is a measure of how often the trigger occurs while the computer is busy processing the previous trigger. In Table.IV.B.2 are shown the total number of antiprotons received by the target for each momentum setting as well as the corresponding live time. The third column gives the luminosity where the luminosity is defined in Table.IV.B.1 as the number of events (K_sK_s or $\bar{\Lambda}\,\Lambda$) per μb assuming 100% detector acceptance and 100% branching ratio into four charged particles.

Table.IV.B.1.

$$\text{Luminosity} = n_{\bar{p}}(im) \cdot n_{CH2} \cdot \sum_{ic=1}^{4} dl_{cell}(ic)$$

$$\text{where } n_{CH2} = \frac{n_p \cdot N_A \cdot \rho_{CH2}}{A}$$

n_p	= 2	number of proton per molecule of CH2
N_A	=6.022 10^{23}	Avogadro's number (number of molecules/mole)
ρ_{CH2}	=.916	density of the CH2 target cell (g/cm^3)
A	=14	Atomic number number (g/mole)
$\sum_{ic=1}^{4} dl_{cell}(ic)$	=1.5	total target length (cm)

A correction to the beam flux $f_c(ic,im)$, Table.IV.A.1, must also be considered for each target cell. This correction is due to misalignment in the target cells and to antiproton emission of δ rays whose energies are high enough to fire a S2 veto. The effective number of antiprotons in cell ic, $n_{\bar{p}}(im)/f_c(ic,im)$, is estimated by using beam events defined in section II.A.6, and by requiring that $\overline{S2}_1..\overline{S2}_{ic-1}.S3_1..S3_{ic-1}$ be true (IV.STINZIG.88). The correction coefficients $f_c(ic,im)$ are shown in Table.IV.B.3 for each cell ic and momentum setting im.

Table.IV.B.2.

Luminosity			
Momentum (MeV/c)	Number of $\bar{p}$ ($x10^8$) on target	Live time (%)	Luminosity (events/μb/4 cells)
1299	74.665	74.6	882.72
1364	69.204	72.7	818.15
1368	98.159	67.0	1160.47
1403	77.780	71.3	919.54
1407	97.823	66.1	1156.49
1420	75.511	68.5	892.72
1424	84.071	69.8	993.91
1430	69.625	75.1	823.12
1434	96.916	69.8	1145.76
1439	69.321	71.3	819.54
1443	98.720	69.3	1167.10
1448	47.224	72.2	558.30
1452	74.049	76.7	875.43
1467	94.243	69.7	1114.17
1471	87.002	65.6	1028.57
1489	110.276	72.4	1303.72
1567	134.215	63.5	1586.73

Table.IV.B.3.

Correction factor f_c					
Momentum	cell #1	cell #2	cell #3	cell #4	cell #5
1567	1.	1.0490	1.1640	1.2699	1.3358
1489	1.	1.0482	1.1643	1.2593	1.3322
1471	1.	1.0482	1.2072	1.3060	1.3760
1467	1.	1.0487	1.1746	1.2832	1.3491
1452	1.	1.0508	1.1685	1.2663	1.3284
1448	1.	1.0556	1.2070	1.3290	1.3868
1443	1.	1.0483	1.1662	1.2629	1.3233
1439	1.	1.0465	1.1744	1.2808	1.3412
1434	1.	1.0505	1.1695	1.2664	1.3392
1430	1.	1.0499	1.1897	1.2913	1.3586
1424	1.	1.0480	1.1718	1.2666	1.3291
1420	1.	1.0504	1.1862	1.2895	1.3642
1407	1.	1.0511	1.1740	1.2745	1.3432
1403	1.	1.0511	1.1740	1.2745	1.3432
1368	1.	1.0512	1.1564	1.2688	1.3271
1364	1.	1.0513	1.2087	1.3118	1.3935
1299	1.	1.0500	1.1600	1.2700	1.3400

IV.C. Detector Acceptance Corrections.

In order to determine the reconstruction acceptance of the detector, 30000 $K_S K_S$ and 80000 $\bar{\Lambda}\,\Lambda$ Monte-Carlo events are isotropically generated in the $\bar{p}$ p center of mass. Each event, once the charged particle tracks have been projected on each of the detector planes and converted into coordinates, follows the same analysis as the actual data. Besides the knowledge of the detector geometry such as plane positions and target positions, the simulation requires the determination of hit distributions and efficiencies of the streamer and drift chamber planes and the determination of the direction and size of the beam. The event reconstruction efficiency is then determined by dividing the number of reconstructed events by the number of generated events.

IV.C.1. Efficiency Determination of Drift Chambers.

A randomly distributed sample of 12 raw data tapes (~10% of the data) is used to determine the efficiencies of the drift chamber planes. Because the extraction of the drift chamber efficiencies requires unambiguous and well defined three dimensional tracks, only events with one three dimensional track in DC13 or one vertex (to get high angle tracks) are selected.

The generation of the DC6 efficiencies are done by requiring that a full track in DC13 (11 out of 13 planes firing and only one two dimensional track in each projection) be found. This track is then projected into DC6 and for projections within the detector boundaries, hits around a ±2 cm area of the track projection are searched. The number of times a hit has been found divided by the number of projections on that plane defines the efficiency.

In the DC13 stack, the efficiency p_i at plane i is calculated by the following formula:

$$p_i = \frac{N_{max}}{N_{max}+N_i}$$

where N_{max} is the number of times a track has no missing hits in all the planes it crosses, (for example, $N_{max} = 4$ for a high angle track crossing only four planes in one projection) and N_i is the number of times a track has no missing hits in all planes it crosses except plane i where no hit is found within a ±2cm region of the track projection.

Table.IV.C.1 shows the efficiencies obtained for all the planes for tracks between [0°, 24°], [24°, 48°] and [48°,80°]. Most of the inefficiencies come from a region around the field and sense wires. Fig.IV.C.1 shows a graphical display of the efficiencies as a function of the plane position. The efficiency fall at small z is real and is not an effect of the efficiency determination algorithm.

Table.IV.C.1.

Drift Chamber Efficiencies					
Plane number	Position (cm)	Efficiency (%) for [0°, 24°]	Efficiency (%) for [24°, 48°]	Efficiency (%) for [48°, 80°]	
1	1.0	87.0	79.6	80.1	
2	2.0	87.2	82.3	83.7	
3	3.7	89.1	87.7	88.8	
4	4.7	89.3	89.1	90.9	
5	6.4	92.3	90.4	93.0	
6	7.4	88.0	89.7	90.4	
7	9.1	93.3	93.1	93.6	DC13
8	10.0	94.9	94.1	94.9	
9	11.7	95.4	95.9	95.0	
10	12.7	96.3	97.2	97.0	
11	14.4	96.7	97.7	97.2	
12	16.1	94.2	96.1	96.6	
13	17.8	97.1	97.8	97.0	
14	22.0	96.5	97.3	91.0	
15	23.0	97.4	98.1	93.7	
16	24.7	96.4	96.5	88.1	DC6
17	25.7	96.0	95.9	87.7	
18	27.4	97.2	97.0	89.5	
19	29.1	96.7	96.1	87.6	

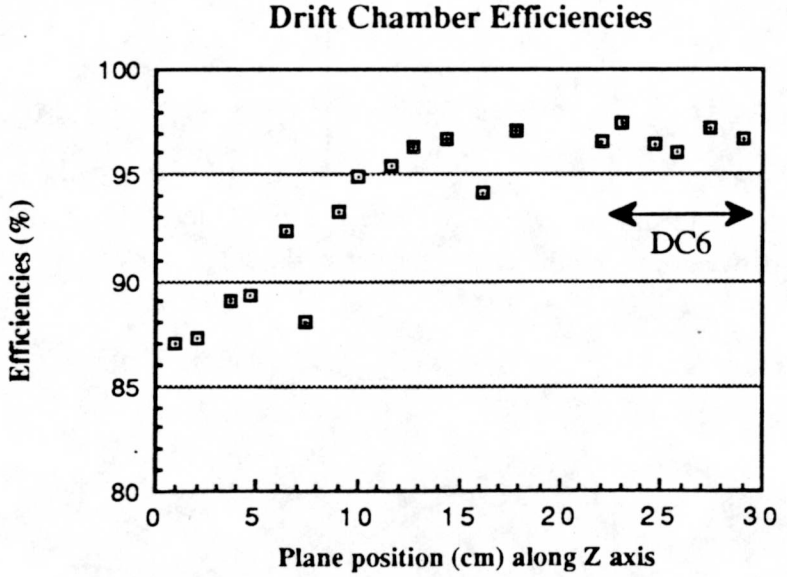

Fig.IV.C.1. Drift chamber plane efficiencies for [0°, 24°] track angles

Finally, in order to simulate as realistically as possible the hit distribution around the tracks, hits within a ±2 cm region of each track candidate are recorded into fourteen tables depending on the track angle. These tables are then used by the Monte-Carlo to generate the same distributions.

As a final test of the self-consistency of the method, efficiencies obtained from Monte-Carlo generated straight through tracks and vertices are found to be the same as the efficiencies obtained from data.

IV.C.2. Efficiency Determination of Streamers Chambers.

The method used to determine the efficiencies of the streamer planes is as follows. Two of the streamer barrels are used to define track candidates. These tracks are projected into the other barrel where the efficiency is calculated. Because only two planes in each projection of the streamer detector are used to define a track candidate, a realistic track candidate must further come from the target region and no hits within ±10 cm of this track should be present in both barrels. The streamer efficiencies are shown in Table.IV.C.2.

Tables of streamer hits are also generated at the same time and are used by the Monte-Carlo in a way similar to the drift chamber procedure explained in the last section.

The resolution of the streamer detector can be determined also from these track candidates. In Fig.IV.C.2, the hit distribution in each of the barrels is shown. Because each distribution is the convolution of the intrinsic resolution $\sigma_{intrinsic}$ of the streamer plane and the error from the projection of the track candidate, a value of 0.47cm for the intrinsic resolution can be extracted from the variances of the three barrel distributions $\sigma_{inner}, \sigma_{middle}, \sigma_{outer}$ according to the formulas

$$\sigma_{intrinsic} = \frac{2.(g^2-g+1)}{\sqrt{g^2+1}}\,\sigma_{inner} \quad \text{and} \quad \begin{cases} \sigma_{middle} = -g.\sigma_{inner} \\ \sigma_{outer} = (g-1).\sigma_{inner} \\ g = (d_{im}+d_{mo})/d_{mo} = 2.88 \end{cases}$$

where g is a geometry factor determined by the distance between the inner and middle barrel d_{im} and the distance between the middle and outer barrel d_{mo}.

Table.IV.C.2.

Streamer Chamber Efficiencies					
Plane number	Efficiency .> 1hit (%)	Efficiency 1 hit (%)	Efficiency 2 hits (%)	Efficiency 3 hits (%)	
1	83.0	80.6	2.1	0.2	Wire
2	92.6	90.3	2.2	0.1	Strip
3	86.0	81.5	3.7	0.4	Wire
4	90.1	87.8	2.3	0.1	Strip
5	89.7	83.1	5.1	1.0	Strip
6	91.4	83.6	6.2	1.0	Wire
7	86.9	84.2	2.4	0.2	Wire
8	92.1	90.5	1.6	0.0	Strip
9	90.9	85.6	4.3	0.5	Wire
10	91.8	89.0	2.6	0.1	Strip
11	89.6	81.1	6.9	1.2	Strip
12	86.2	79.5	5.2	0.9	Wire
13	89.9	85.9	2.9	0.5	Wire
14	90.3	88.7	1.6	0.1	Strip
15	83.7	77.2	4.9	0.9	Wire
16	90.8	88.3	2.4	0.1	Strip
17	92.0	83.1	7.2	1.2	Strip
18	89.2	77.5	8.6	1.9	Wire
19	85.2	82.6	2.3	0.2	Wire
20	93.0	90.8	2.1	0.1	Strip
21	90.4	86.2	3.7	0.3	Wire
22	93.0	90.4	2.4	0.1	Strip
23	90.0	84.0	4.9	0.8	Strip
24	85.8	78.9	5.5	0.9	Wire
Average efficiency for wire planes 87.4 %			Average efficiency for strip planes 91.2 %		

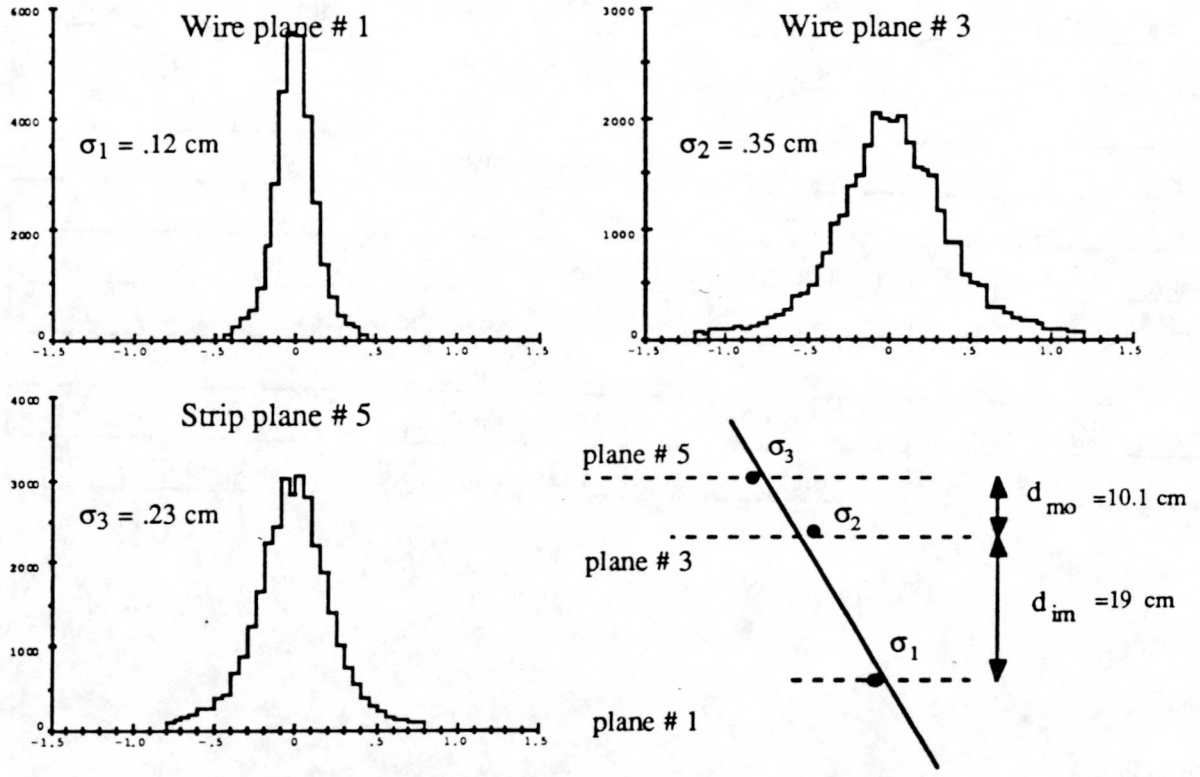

Fig.IV.C.2. Residual distributions for three hit tracks in the streamer projection XZ.

As a final result in the study of the streamer detector, Fig.IV.C.3 shows the cluster size distributions for both wire and strip planes. The intrinsic resolution $\sigma_{intrinsic}$ shows no dependance with respect to the track angle although the cluster size and track angle are definitively correlated.

IV.C.3. Beam determination.

The nominal beam parameters, as shown in Table.IV.C.3, are used to simulate the beam in the Monte-Carlo. Their values are determined in such a way that the $\bar{\Lambda}\,\Lambda$ Monte-Carlo analysis distributions mimic the ones obtained from the real data as seen for example in Fig.III.D.3. The $\bar{\Lambda}\,\Lambda$ reaction is used because the analysis is better defined and more events are available.

Table.IV.C.3.

Nominal Beam Definition Parameters		
dx_{beam}	.005	Beam slope in the x projection
dy_{beam}	-.002	Beam slope in the y projection
x_{int}	-.055 cm	Beam position in the x direction
y_{int}	-.025 cm	Beam position in the y direction
$z1_{int}$	-3.10 cm	z position of cell #1
$z2_{int}$	-2.70 cm	z position of cell #2
$z3_{int}$	-2.17 cm	z position of cell #3
$z4_{int}$	-1.58 cm	z position of cell #4
$z5_{int}$	-1.20 cm	z position of cell #5
$\Theta_{divergence}$	.28 °	Polar divergence of the beam
ρ_{beam}	.1 cm	radius of the beam
$\Delta1_{int},\Delta2_{int},\Delta5_{int}$	.25 cm	length of target cell #1,#2,#5
$\Delta3_{int},\Delta4_{int}$	.5 cm	length of target cell #3,#4

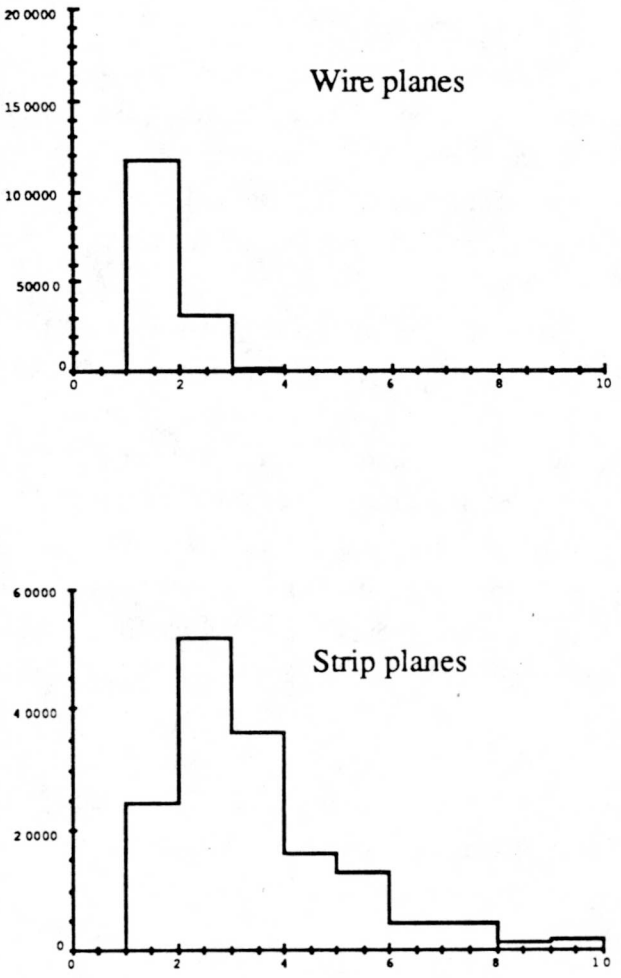

Fig.IV.C.3. Cluster size distributions of the streamer wire (top) and strip (bottom) planes.

IV.C.4. Detector Acceptance.

Now that we know the detector efficiencies and beam parameters, a full simulation of the reaction under investigation can be done. By dividing the number of Monte-Carlo events reconstructed by the analysis with the number of events generated, the reconstruction efficiencies as a function of $|\cos(\theta_{CM})|$ in the $\bar{p}$ p center of mass is calculated. These distributions are shown in Fig.IV.C.5 for the $\bar{\Lambda}\,\Lambda$ events at 1567 Mev/c and 1439 MeV/c and in Fig.IV.C.6 for K_SK_S events at 1435 MeV/c.

It is instructive to look at the underlying structure of the K_SK_S angular reconstruction efficiencies by separating the K_SK_S events in three categories. The events with all tracks in the stack (stack events) have a K_S center of mass angle close to 90°. On the other hand, the events with their second vertex entirely in the streamer detector (streamer events) correspond to both K_S emitted in the forward and backward direction. Finally, about half of the events have a shared vertex between the drift chamber stack and the streamer stack (shared events) and tend to be emitted around 45° . The streamer detector is extremely important and accounts for about 80% of the reconstructed events.

The systematic errors associated with the detector acceptance can be estimated from the dependance of the total K_S acceptance as a function of the drift chamber and streamer plane efficiencies as shown in Fig.IV.C.4 when all the planes efficiencies are increased or decreased by a same percentage. An uncertainty of 1% in the determination of the plane efficiencies (from bias of the efficiency determination method) will translate into a 2.5% uncertainty in the total K_S acceptance and a 2.5% systematic error related to the cross section.

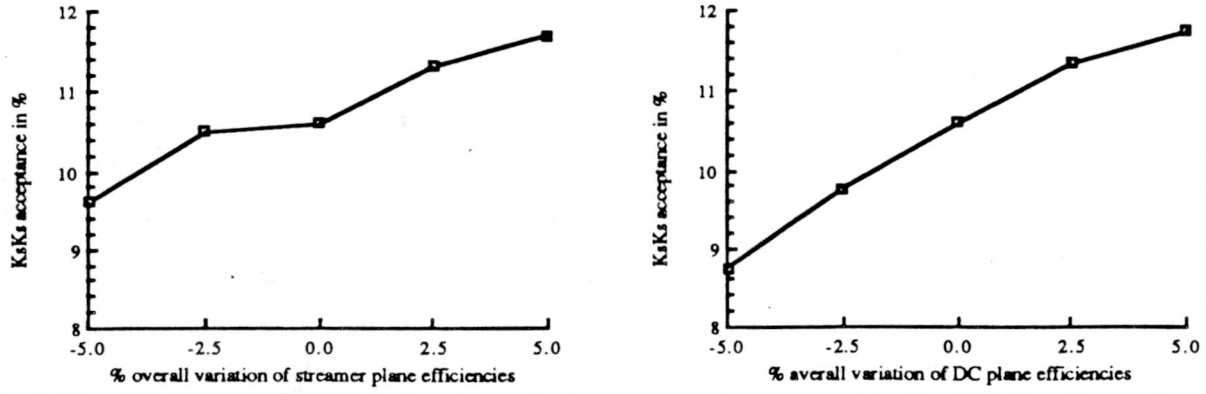

Fig.IV.C.4. Detector acceptance dependance as a function of streamer overall efficiencies (left) and drift chamber overall efficiencies (right). The efficiencies are varied around the efficiencies found in section IV.C.

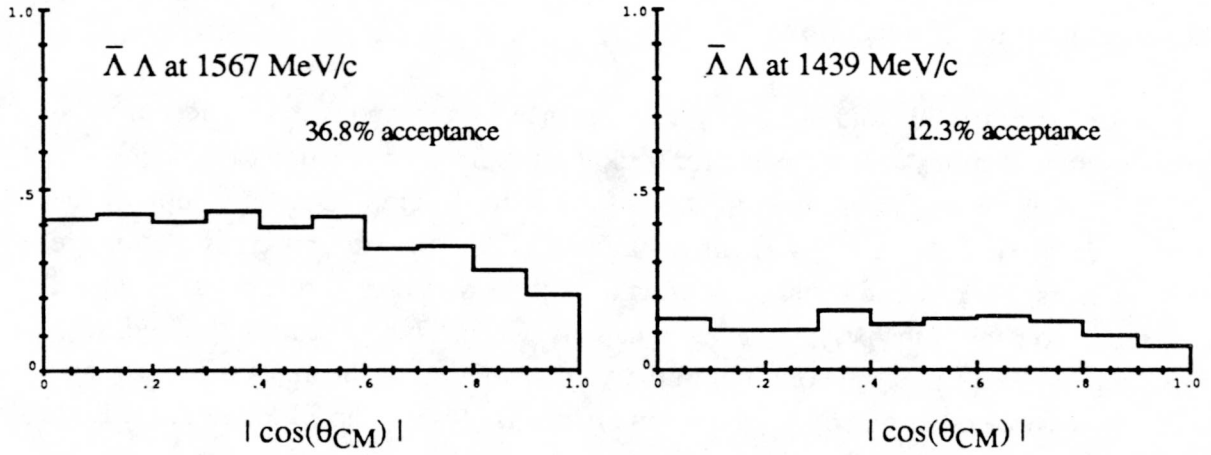

Fig.IV.C.5. $\bar{\Lambda}\,\Lambda$ reconstruction efficiencies at 1567 and 1439 MeV/c

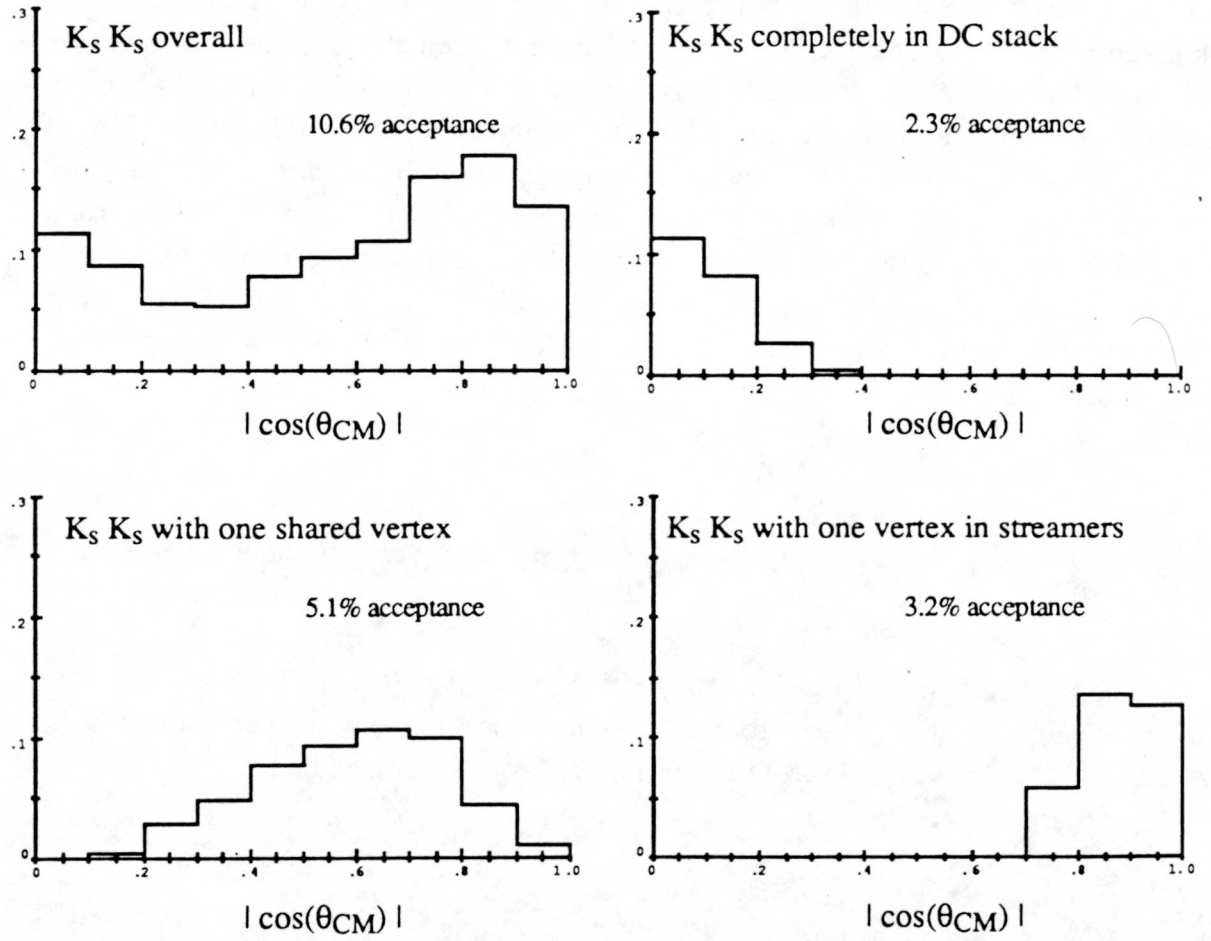

Fig.IV.C.6. $K_S\,K_S$ reconstruction efficiencies for all momenta with the different DC stack and streamers contributions

IV.D. Background Corrections.

Once the beam flux and the detector acceptance have been taken into account, the differential cross sections (not corrected for background) for both reactions are calculated. Fig.IV.D.1 shows the results of the evaluation of the K_SK_S differential cross section by the formula given in Table.IV.A.1. Two main background corrections to this cross section are present. The first background source, common to both K_SK_S and $\bar{\Lambda}\,\Lambda$ reactions, is caused by the carbon content of the polyethylene target cells (CH_2). The second background, seen in Fig. III.D.6 by the presence of a tail in the χ^2 distribution of the analysed K_S events, arises from possible other reactions whose kinematics is close to the K_S kinematics. Both backgrounds are difficult to reproduce through a Monte-Carlo simulation and must be estimated from actual data.

V.D.1 Carbon subtraction.

In order to estimate the carbon background contamination of the K_SK_S sample, a fifth graphite cell has been added to the target. This extra cell allows measurement of the $\bar{p}$ p/C $\rightarrow$ K_SK_S (or $\bar{\Lambda}\,\Lambda$) contribution cross section, as shown in Fig.IV.D.2a, where an antiproton interacts with a proton inside the carbon nucleus (not a two body reaction) to create two K_S (or Λ) whose kinematics is very close to the reaction studied. Only thirty nine K_SK_S events are found in the graphite cell for all momenta. The carbon contribution cross section is then assumed to be independent of the $\bar{p}$ momentum and is determined according to the formula shown in Table.IV.A.1 and Table.IV.B.1. The number of target protons (n_{CH2}) must then be replaced by the number of target carbon atoms n_{CAR} defined as

$$n_{CAR} = \frac{N_A \cdot \rho_{CAR}}{A}$$

where

$N_A = 6.022\ 10^{23}$: Avogadro's number
$\rho_{CAR} = 2.265$ g/cm^3 : Graphite density
$A = 12$: Atomic number of C

The total carbon contribution cross section amounts to $0.19 \pm .05$ μb or about 15% of the total number of K_SK_S events found. The same procedure must also be applied to the $\bar{\Lambda}\,\Lambda$ analysis as is shown in Fig.III.D.2b for the 1567 MeV/c momentum.

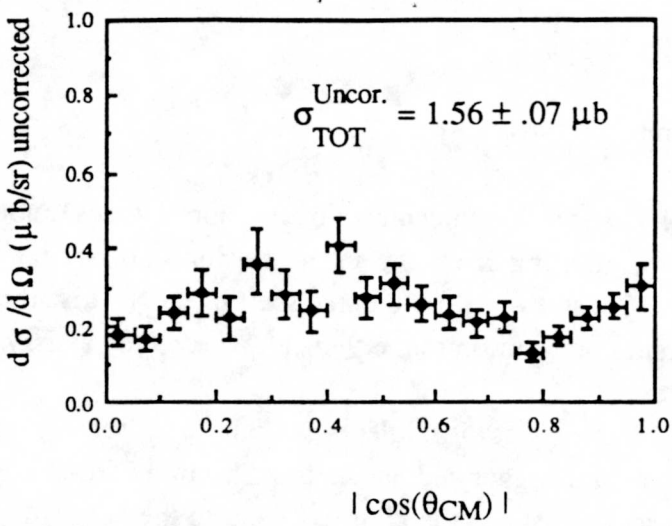

Fig.IV.D.1. Uncorrected K_sK_s differential cross section for all momenta.

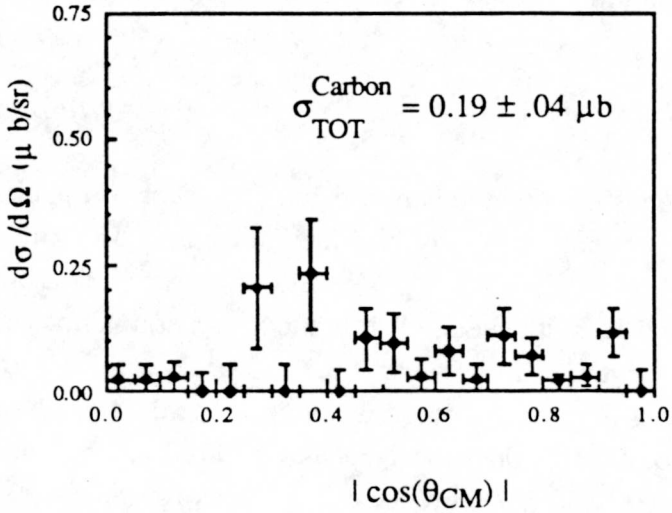

Fig.IV.D.2a. Carbon contribution to the $\bar{p}\,p \rightarrow K_sK_s$ differential cross section.

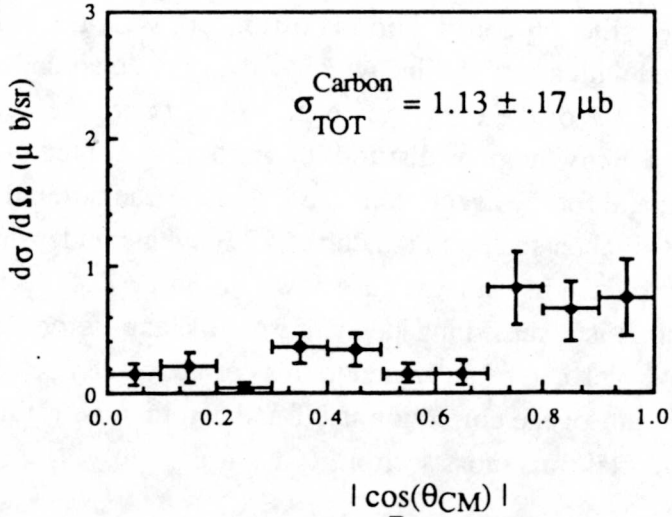

Fig.IV.D.2b. Carbon contribution to the $\bar{p}\,p \rightarrow \bar{\Lambda}\,\Lambda$ differential cross section.at 1567 MeV/c

IV.D.2 χ^2 Tail subtraction.

Besides the $\bar{p}\,p \rightarrow K_S K_S$ events which occur in the carbon nucleus, another type of event with tracks primarily originating from the target region can not be completely eliminated by the K_S analysis. These events are clearly seen in the χ^2 distribution tail of Fig.IV.D.3 and are an important contribution to the χ^2 peak where they satisfy exactly the same kinematics as the $K_S K_S$ events.

The $K_S K_S \pi^0$ and $K_S K^*$ events as possible background sources are an obvious choice. They satisfy the same neutral trigger and have a cross section 25 to 50 times greater than the expected $K_S K_S$ cross section. When the π^0 is collinear to the beam, the three body $K_S K_S \pi^0$ events are kinematically very close to the two body $K_S K_S$. If this tail consists mostly of $K_S K_S \pi^0$ events, it should be seen in a $K_S K_S X$ missing mass spectrum defined as

$$m_X^2 = E_X^2 - \vec{p}_X^{\,2} = \left\{ E_{\bar{p}} + m_p - (E_{K_S} + E_{K_S}) \right\}^2 - \left\{ \vec{p}_{\bar{p}} - (\vec{p}_{K_S} + \vec{p}_{K_S}) \right\}^2$$

where the missing mass depends only on the vertex parameters such as opening angle and vertex direction and is independent from any K_S kinematic guess and kinematic fit. In Fig.IV.D.5a and Fig.IV.D.5b are shown the $K_S K_S X$ missing mass spectra obtained from Monte-Carlo $K_S K_S$ events and $K_S K_S \pi^0$ events. While the resolution is not very good, the missing mass of the $K_S K_S \pi^0$ events can be clearly seen to peak at the π^0 mass. On the other hand, when the same missing mass method is applied to real data, an observable π^0 peak can neither be found for events under the χ^2 peak, see Fig.IV.D.5.c, nor for events belonging to the tail, see Fig.IV.D.5d. The absence of a π^0 peak for tail events implies that the major portion of the tail is not made of $K_S K_S \pi^0$ events but consists more of a combinatorial type background which passed the K_S kinematics.

Fig.IV.D.3 shows how the tail contribution is estimated. First the tail, defined as events with $5 < \chi^2 < 25$, is fitted with a straight line which is then projected under the peak to find the contribution. About 22% of the events under the χ^2 peak are then considered as background. Assuming that the raw angular distribution in the $\bar{p}\,p$ center of mass is the same for all events in the tail and for the events contributing to the background, the angular distribution of the tail events is then scaled to match the 22% events under the peak and a tail contamination cross section can be estimated as shown in Fig.IV.D.4. As in the carbon subtraction, the tail contribution is assumed independent from the antiproton momentum.

The systematic error which can be attributed to this correction can be conservatively assumed to be as big as one half of the correction itself and can then be estimated to .1 to .15 μb or 10% to 15% of the total final cross section.

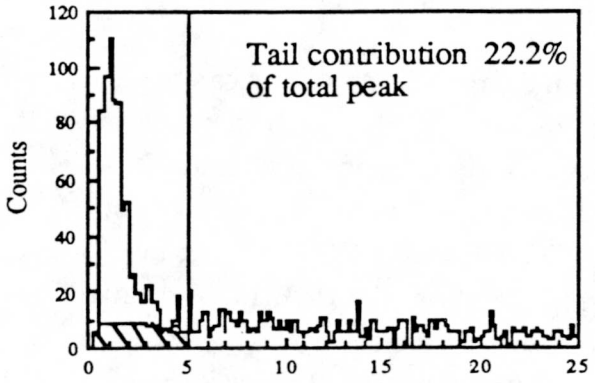

Fig.IV.D.3. K_sK_s χ^2 distribution and tail contribution to the χ^2 peak assuming a linear background.

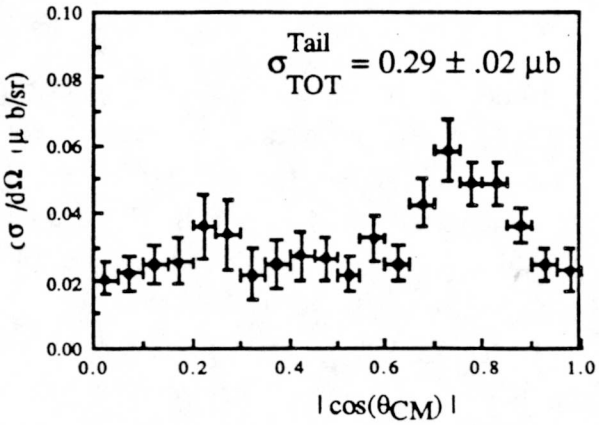

Fig.IV.D.4. Tail contribution to the K_sK_s differential cross section obtained by scaling the distribution in the center of mass of the tail.

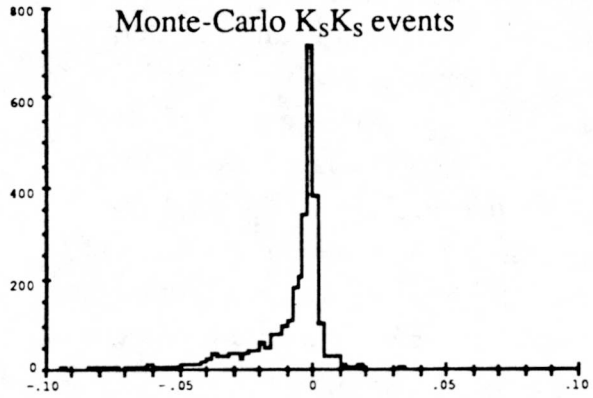

Fig.IV.D.5a. Missing mass (K_sK_s X) distribution from Monte-Carlo K_sK_s events

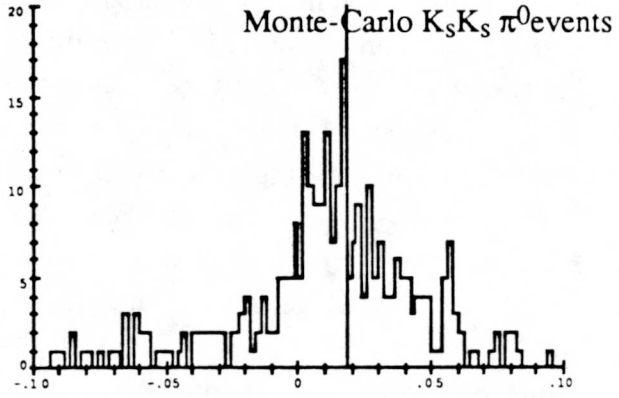

Fig.IV.D.5b. Missing mass (K_sK_s X) distribution from Monte-Carlo K_sK_s π^0 events

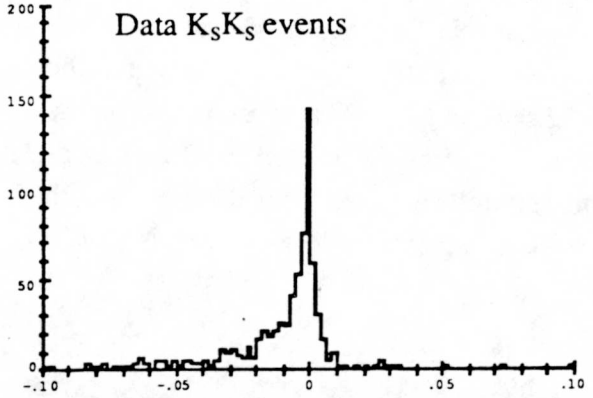

Fig.IV.D.5c. Missing mass (K_sK_s X) distribution from K_sK_s data events

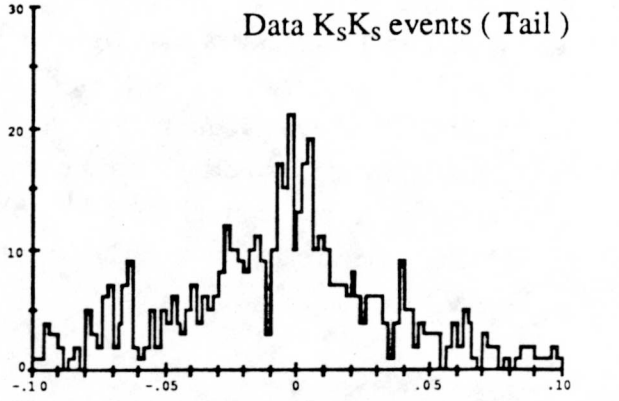

Fig.IV.D.5d. Missing mass (K_sK_s X) distribution from K_sK_s data for tail events ($5 < \chi^2 < 25$)

IV.E. K_S and Neutral Trigger.

Another source of systematic effects occurs in the target. The problem can be seen in Fig.IV.E.1a where the number of K_SK_S events normalized by the beam flux and live time (all events) is shown for each target cell. There is a significant drop (up to 25%) between the first cell and the last cell. This drop can be better understood if we look at this effect for the three different kinds of K_SK_S events defined in section IV.C.3. The events completely in the stack (stack events) show no significant drop, Fig.IV.E.1a. The same behavior is true for $\bar{\Lambda}\,\Lambda$ events. On the other hand, the drop in normalized K_SK_S becomes increasingly more pronounced for events with one shared vertex between the stack chamber and the streamer detector (shared events) and for events with one vertex entirely in the streamers (streamer events), Fig.IV.E.1b. In order to understand this effect, two extreme cases can be assumed.

In the first case, we do not lose any good K_S events, and the drop is due entirely to unwanted background such as four charged particles coming from the target and which leaked through the neutral trigger and are therefore part of the χ^2 tail. The last cell would then give a more accurate measure of the cross section. This result is unfortunately not consistent with the χ^2 tail of the streamer events being the same for the different cells.

The second more likely possibility is that we are really losing good K_S events through the neutral trigger. This cell by cell drop could then happen if pions emitted from backward K_S, which are slow and decay close to the target, could trigger the S2 photomultiplier light guide through Cerenkov light and therefore would not create a neutral trigger (only the S2 vetos upstream of the cell in which the neutral reaction takes place are used in the neutral trigger). This time, the first cell is much more likely to give a closer value to the true cross section.

A correction to this neutral trigger inefficiency is therefore applied by assigning inefficiencies in the Monte-Carlo simulation to each target cell as a function of the three kinds of K_SK_S events discussed above. The corrections are only applied to events with at least a track in the streamers and originating from the last four target cells. For example, the extracted inefficiencies in cell #2, cell #3, and cell #4 for events with only one track in the streamers (shared events) are respectively 19.4%,22.0%, and 30.0% and are based on the slope shown in Fig.IV.E.1b (shared events points). By extrapolation, an inefficiency of 38% is assumed for the graphite cell. The same procedure is also used for the events with two tracks in the streamer tubes. The detector acceptance is therefore lowered and is shown in Fig.IV.E.1c.

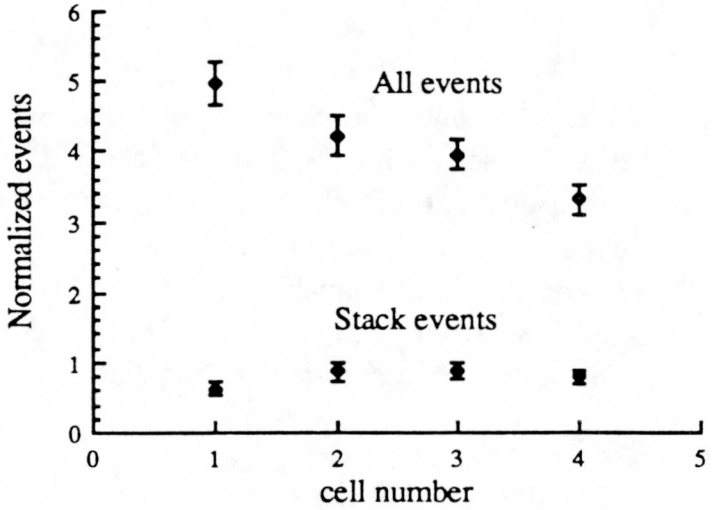

Fig.IV.E.1a. Normalized K_SK_S counts per cell for all events (TOP) and for events which are entirely in the drift chamber stack (BOTTOM).

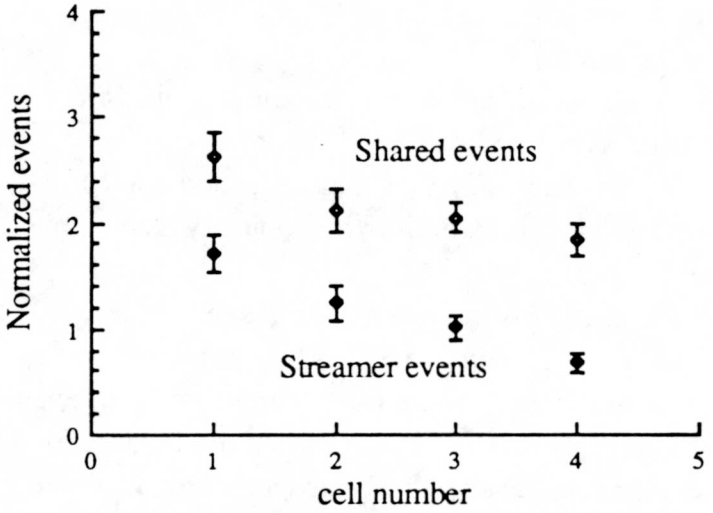

Fig.IV.E.1b. Normalized K_SK_S counts per cell for events with a shared vertex between the drift chamber stack and the streamer stack (TOP) and for events with one vertex completely in the streamers (BOTTOM).

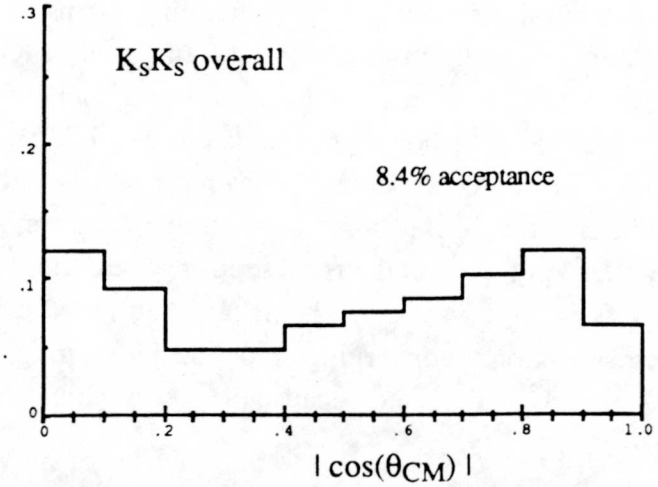

Fig.IV.E.1c. K_SK_S reconstruction efficiencies for all momenta when the neutral trigger correction is applied. This graph should be compared with Fig.IV.C.6.

However, the correction to the cross section is not as important as one would expect from the lowering of the detector acceptance. The increase in cross section of about 20% that one expects from the lowering of the acceptance, Fig.IV.E.1c and Fig.IV.C.6, is almost totally compensated by a higher carbon subtraction (because of the inefficiency assigned to the carbon cell) and amounts to only 3%. The number of normalised events decreases by about 15% between the first and second cell as shown in Fig.IV.E.1a. Half of this decrease can be taken as an estimation of the systematic error associated to this correction.

IV.F. Penalty Studies and Lifetime Distributions.

IV.F.1 Penalty Determination.

In order to keep the beam parameters within physical limits, a penalty must be applied to the χ^2, as explained in Paragraph.III.D. While the relatively loose penalty setting of five, see Table.III.D.1, is used in the kinematic fitting reduction, all the final results are determined with a tighter penalty setting of two. In trying to justify this seemingly arbitrary setting, a penalty study is necessary.

Fig.IV.F.1a shows the number of analysed K_SK_S from data and Monte-Carlo events obtained for six penalty settings where the zero setting assumes a fixed beam at its nominal parameter values. The number of Monte-Carlo simulated K_SK_S events found by the analyser does not depend strongly on the penalty setting used, suggesting that as the penalty is increased the uncertainties assigned to the beam can safely be shifted to the other, non beam related, kinematical variables such as center of mass angle of the K_S and pions.

On the other hand, by tightening the beam parameters, an increasing number of analysed K_SK_S events are lost from our data sample indicating that more and more non K_SK_S events (background) are removed. If this number of analysed K_SK_S events would converge asymptotically towards a definite value as the penalty is tightened, we would have a clear signal that we have removed all the non K_SK_S events (no χ^2 tail left) .

Unfortunately, even with a fixed beam, the background is still present. The question then becomes whether the background is subtracted correctly. Fig.IV.F.1b answers this question by showing the total cross section after the carbon and tail background subtraction as a function of penalty. The penalty setting #2 used until now is justified because the total cross section is converging at low penalty settings. At the penalty setting zero, too much background is subtracted because the χ^2 distribution starts widening beyond the χ^2 cut used ($\chi^2< 5$).

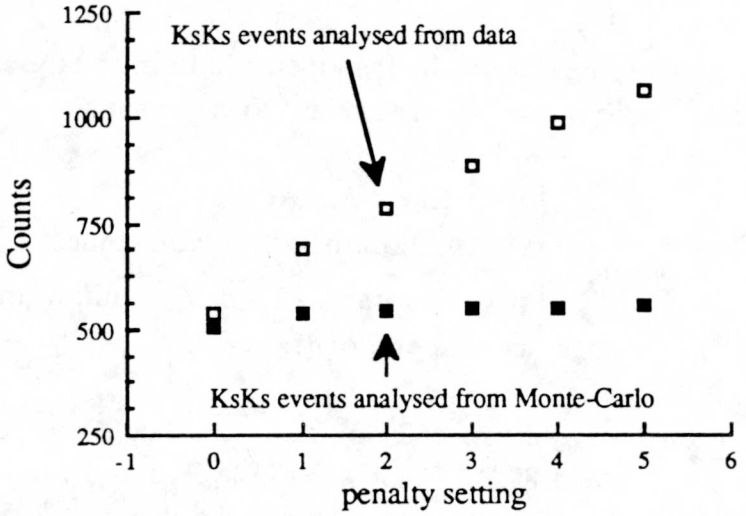

Fig.IV.F.1a. Number of K_sK_s events ($\chi^2 < 5$, no χ^2 tail and carbon subtraction) found from data and 5000 Monte-Carlo generated KsKs events as a function of penalties assigned to the beam parameters.

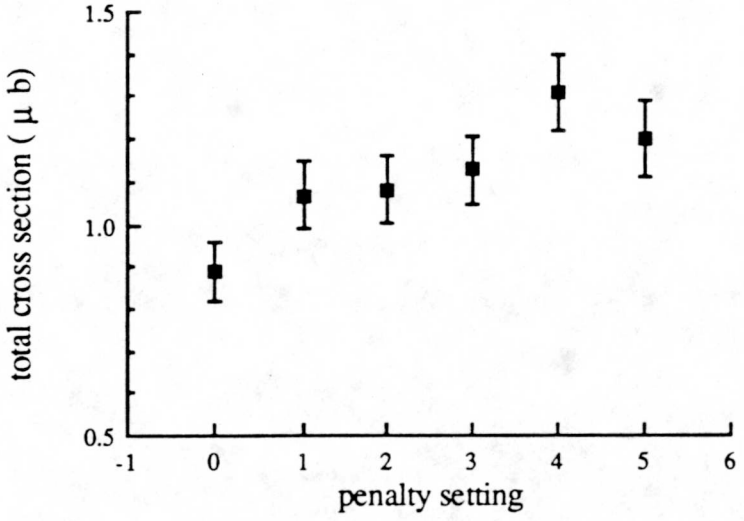

Fig.IV.F.1b. Total K_sK_s cross section obtained after tail substraction and carbon substraction as a function of penalties assigned to the beam parameters.

IV.F.2 Lifetime Distributions.

From the laboratory decay distances found by the kinematic fitting analyser, the neutral particle lifetime in their rest frame is determined according to the formula

$$\tau = \frac{m \cdot r}{p \cdot c} \qquad \text{where} \begin{cases} m & : K_S \text{ or } \Lambda \text{ rest mass} \\ r & : \text{Laboratory decay distance} \\ p & : \text{Laboratory } K_S \text{ or } \Lambda \text{ momentum} \\ c & : \text{speed of light} \end{cases}$$

The lifetime distributions when corrected by a Monte-Carlo simulation, should approximate the well known 263.2 ps for Λ and $\bar{\Lambda}$ and 89.22 ps for K_S. Fig.IV.F.2 and Fig.IV.F.3 show good agreement for the lifetimes of both particles as long as the short and very long lifetime are not considered. There is a systematic underestimation of acceptance when the decay time is long, but this effect is small on the total cross section and can be estimated as no more than 3% for both reactions.

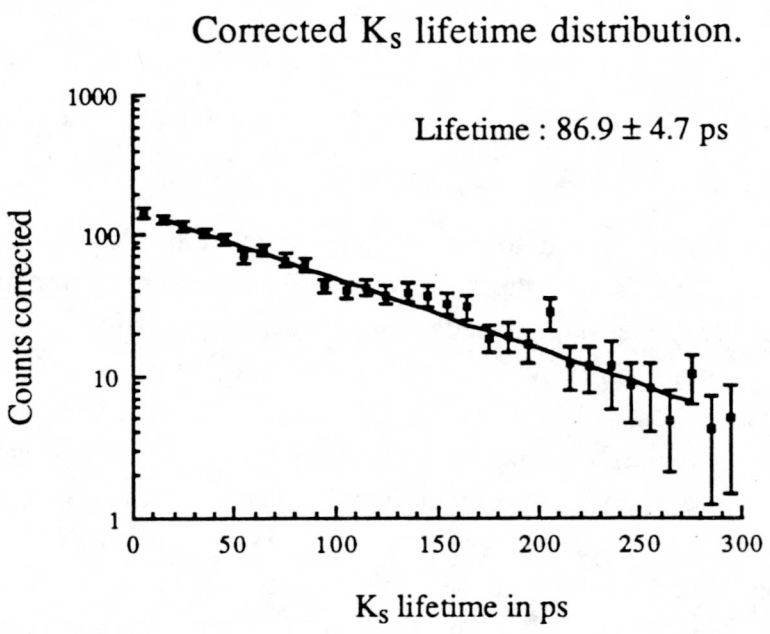

Fig.IV.F.2. K_S lifetime distribution corrected by Monte-Carlo for K_SK_S events with $\chi^2 < 5$. The K_S lifetime is 89.22 ± .002 ps.

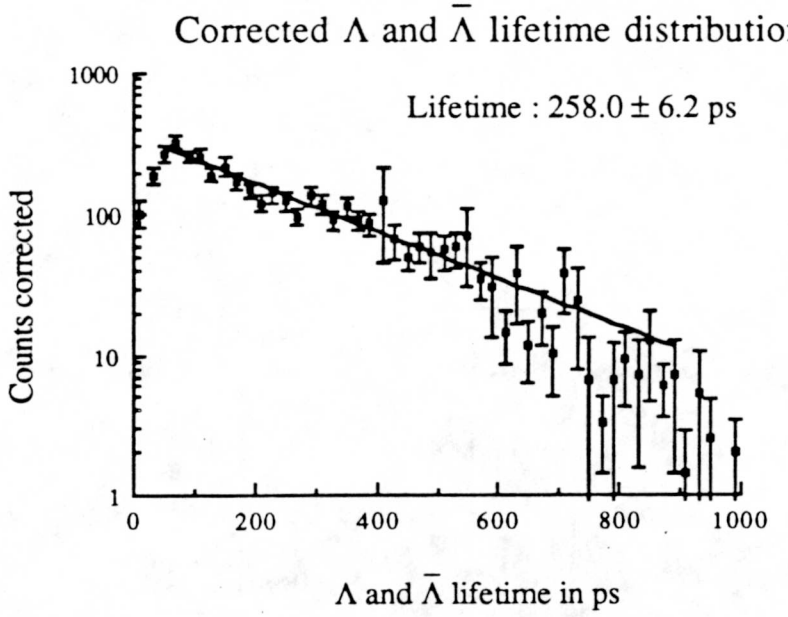

Fig.IV.F.3. Λ and $\bar{\Lambda}$ lifetime distribution corrected by Monte-Carlo for $\Lambda\bar{\Lambda}$ events with $\chi^2 < 5$. The Λ lifetime is 263.1 ± .02 ps.

V. Results.

V.A. $\bar{p}\,p \rightarrow K_s\,K_s$ Results.

The total annihilation cross section to two K_s is shown in Fig.V.A.1 for all seventeen momenta. Appendix A also shows the actual cross section numbers along with their corresponding uncorrected number of analysed events. On average, only about forty events are found at each momentum. These low statistics do not allow the use of smaller momentum bins (for example, of each individual target cell size) to search for a resonance of very narrow width. Each momentum measurement covers 3.2 MeV/c^2 in the invariant center of mass energy. The errors shown are only statistical. The systematic errors are estimated at ±25% (as discussed in the last chapter; 10% from χ^2 tail correction, 7% from the neutral trigger cell correction, 2.5% from chamber efficiencies determination and 2.5% from the carbon contamination correction) and are of the same size as the statistical errors. The absolute value of the total cross section is therefore not very accurately known but the actual determination of the resonance parameters should not suffer from that fact if we assume that the systematic corrections are fairly independent of the specific momenta.

The differential cross sections for each momentum are shown in Fig.V.A.2. Because both kaons are indistinguishable, the differential cross section is only measured as a function of the absolute value of $\cos(\theta_{CM})$. The differential cross section suffers from very low statistics (about 1 to 2 counts per bins) and strong systematic errors. The systematic uncertainty is not uniformly distributed along the center of mass angle. The main systematic error involves the trigger inefficiency explained in section IV.E. and is more pronounced in the forward part of the differential cross section.

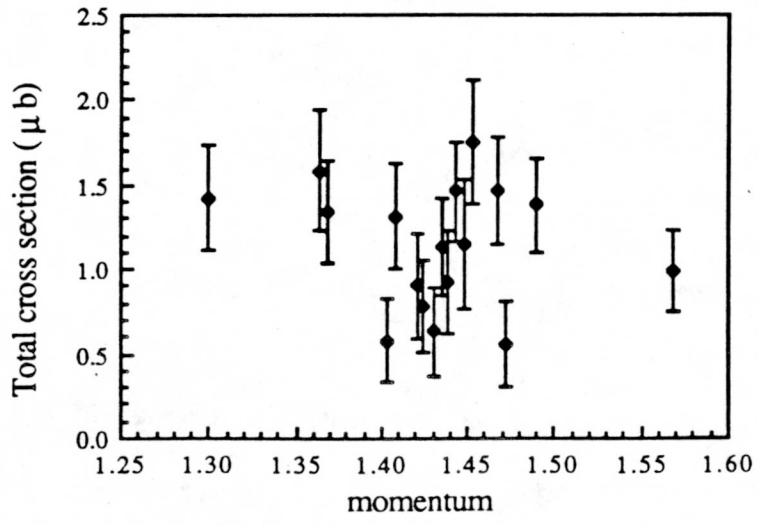

Fig.V.A.1. Total cross section of $\bar{p}\,p \rightarrow K_s\,K_s$ for all momenta

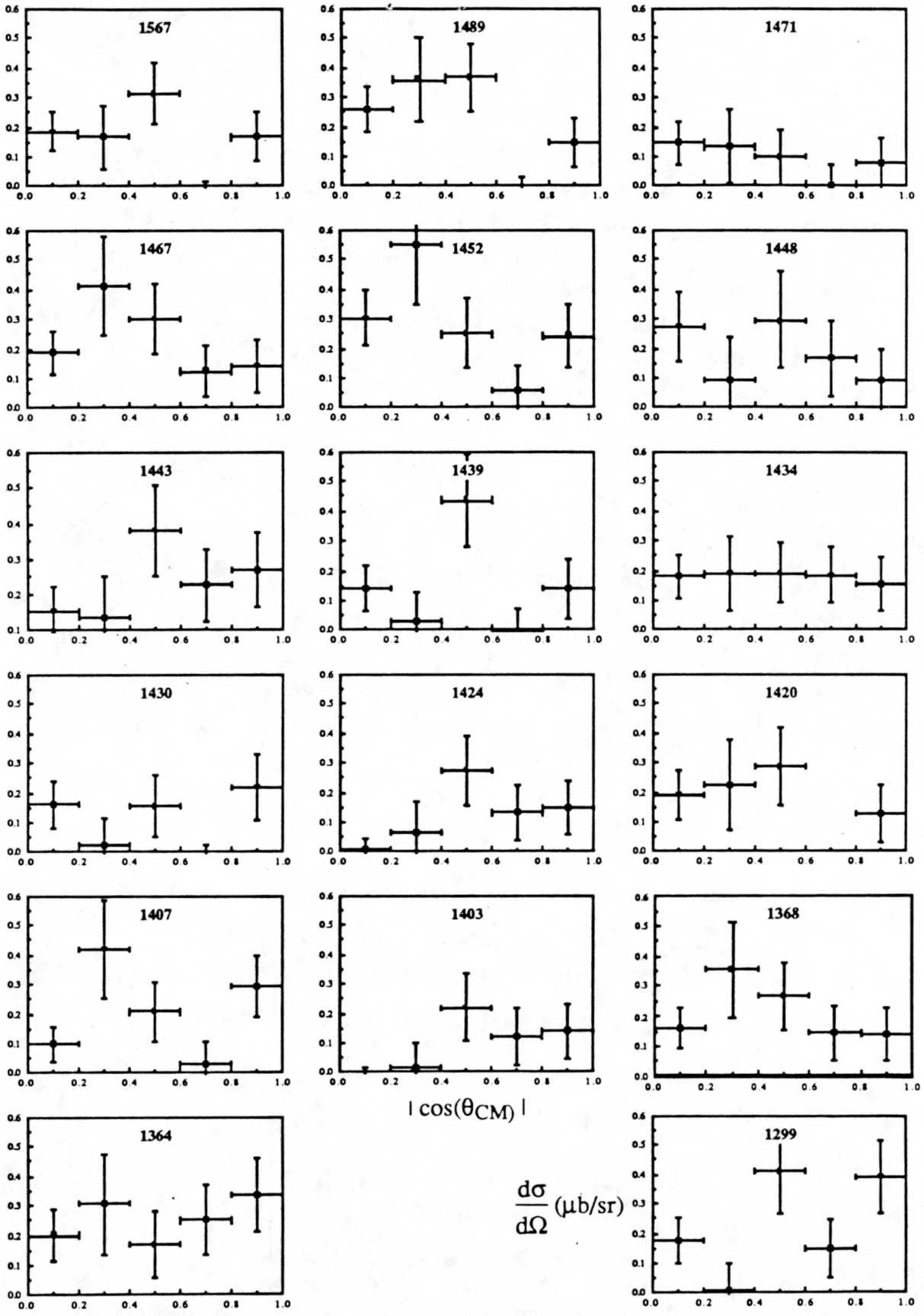

Fig.V.A.2. Differential K_sK_s cross section for all momenta in μb/sr

In order to increase statistics, the differential cross sections can be combined into three groups as shown in Fig.V.A.3 (statistic errors only). The 1435 differential cross section group contains the momenta around the supposed mass of the resonance, while the 1500 and 1360 groups cover both ends of the scan.

Finally, in Fig.V.A.4a is shown the differential cross section of all momenta with only the statistical errors while Fig.V.A.4b shows the same differential cross section with the statistical and systematic errors combined.

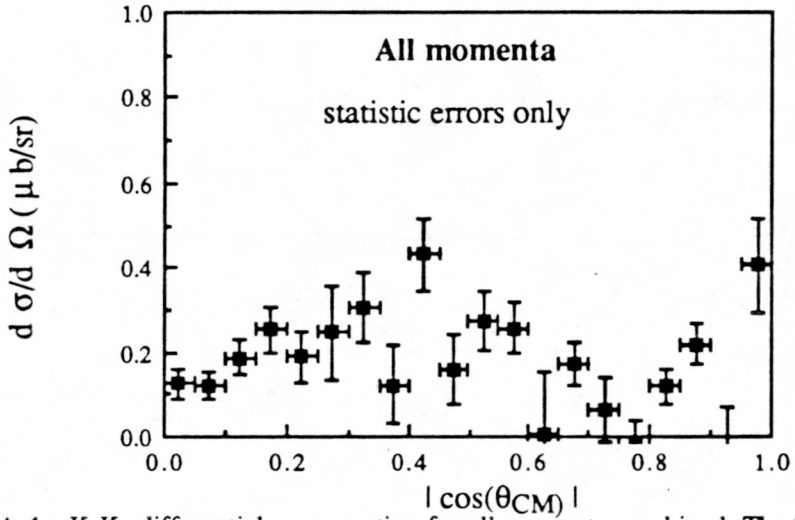

Fig.V.A.4a. K_sK_s differential cross section for all momenta combined. The 25% systematic error is not included

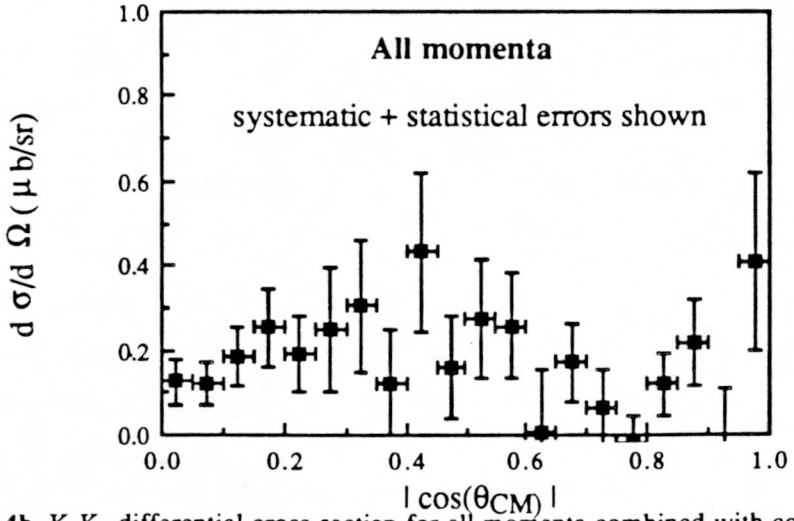

Fig.V.A.4b. K_sK_s differential cross section for all momenta combined with combined statistical and systematic errors.

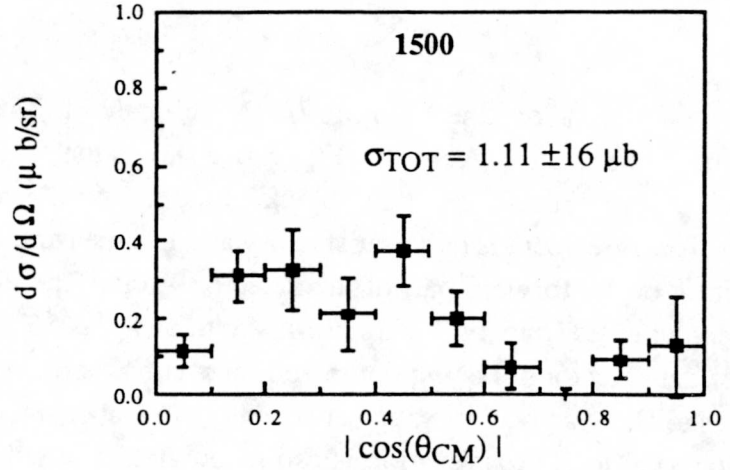

Fig.V.A.3a. K_sK_s differential cross section for the combined 1567,1489,1471, and 1467 momenta. The errors are statistical.

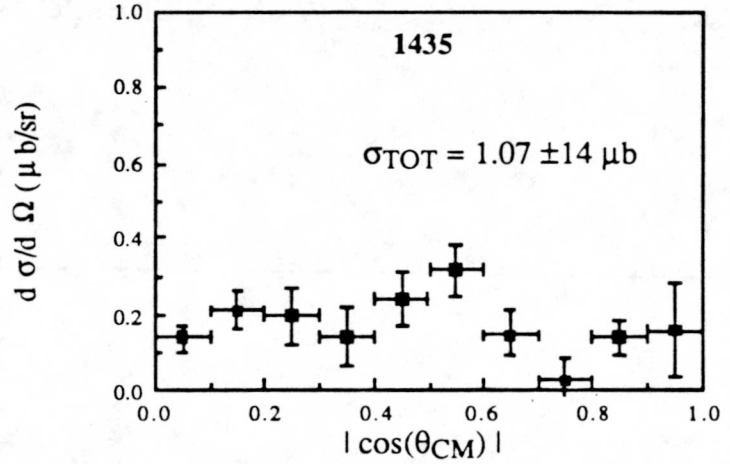

Fig.V.A.3b. K_sK_s differential cross section for the combined 1452,1448,1443,1439,1434,1430,1424, and 1420 momenta. The errors are statistical.

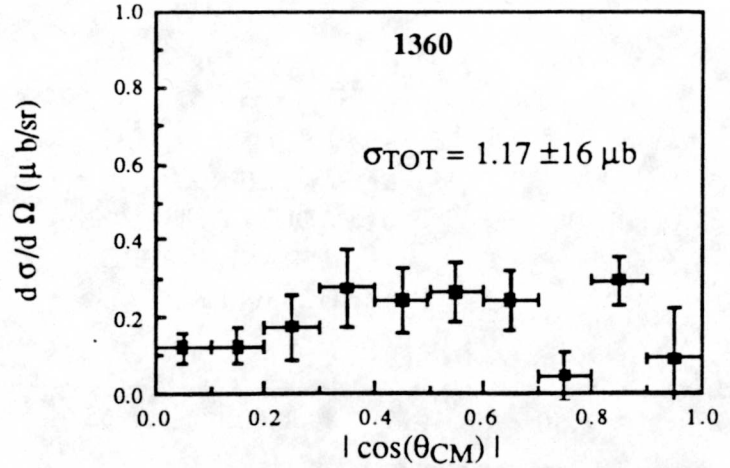

Fig.V.A.3c. K_sK_s differential cross section for the combined 1407,1403,1368,1364, and 1299 momenta. The errors are statistical.

V.B. $\bar{p}\,p \rightarrow \bar{\Lambda}\,\Lambda$ Results.

About half of the scan took place above the 1435 MeV/c $\bar{\Lambda}\,\Lambda$ threshold. The same analysis program is therefore used to extract $\bar{\Lambda}\,\Lambda$ events. Fig V.B.1 shows the total $\bar{\Lambda}\,\Lambda$ cross section obtained at eight momentum settings (black squares) with previous measurements of the reaction. The agreement is quite satisfactory and is a measure of how well the Monte-Carlo simulation of the forward part of the detector works. The detector acceptance for $\bar{\Lambda}\,\Lambda$ events, which ranges from 12% at 1437 MeV/c to 36% at 1567 MeV/c is low and is a consequence of the detector not being optimized for reconstruction of $\bar{\Lambda}\,\Lambda$ events; DC6 has too few planes to allow a good tracking between both chamber stacks. The systematic error associated with the total cross section is estimated at ±15% and comes mainly from the efficiency determinations of the drift chamber planes (±5%) and the dead spot size uncertainty (±10%). In Fig V.B.2, the total $\bar{\Lambda}\,\Lambda$ cross section in the threshold region is compared with the previous PS185 measurement (V.FRANKENBERG.88).

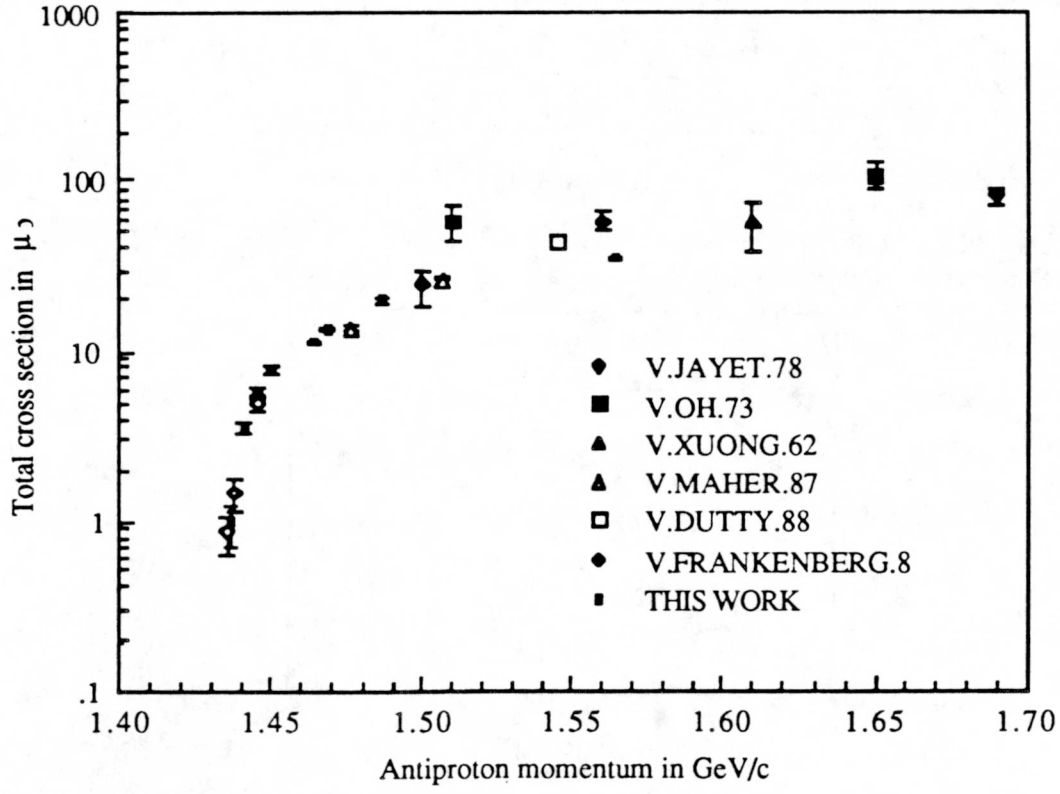

Fig.V.B.1. $\bar{\Lambda}\,\Lambda$ total cross section (small black squares) and other results.

Finally, Fig .V.3 shows the $\bar{\Lambda}\,\Lambda$ differential cross section at 1471 MeV/c for $\bar{\Lambda}$ or Λ center of mass angles of 0 to 90 degrees. No baryon number analysis is done to determine which decay particle is a $\bar{\Lambda}$ or Λ. The new data shown in Fig.V.B.1 and Fig.V.B.2 are listed in Appendix B.

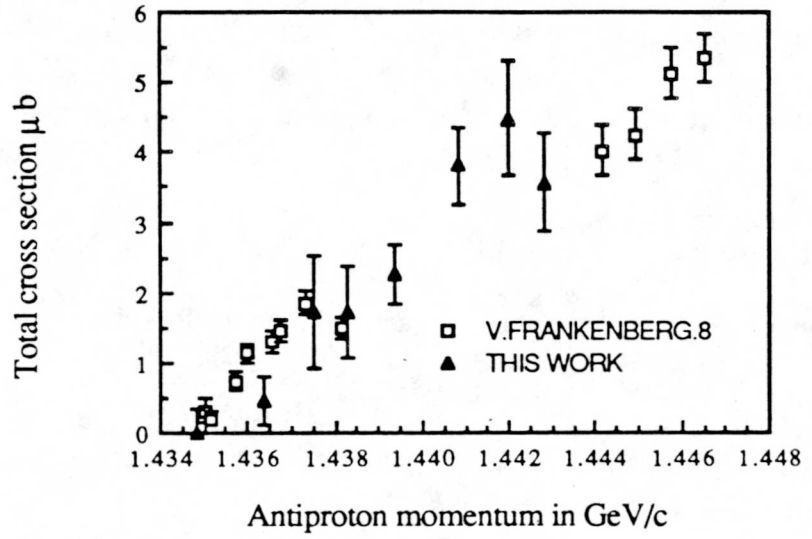

Fig.V.B.2. $\bar{\Lambda}\,\Lambda$ total cross section closed to threshold.

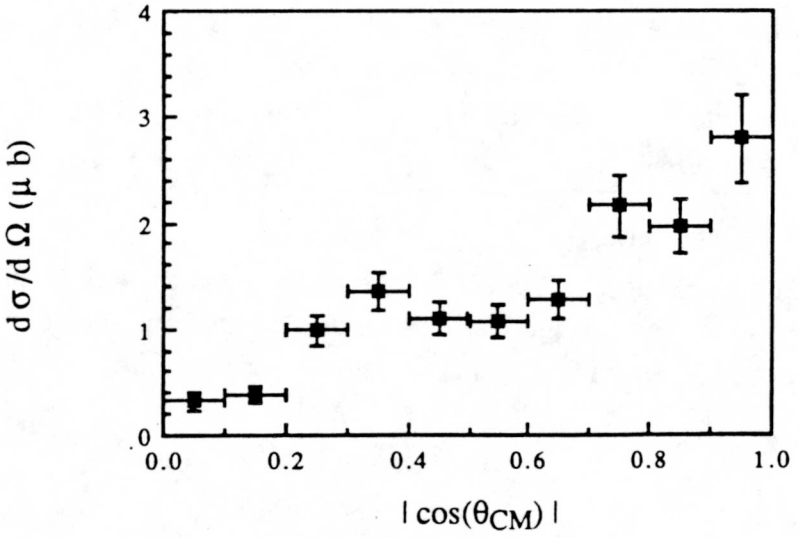

Fig.V.B.3. $\bar{\Lambda}\,\Lambda$ differential cross section at 1471 MeV/c.

VI. $\xi(2230)$ Resonance Analysis.

If the $\xi(2230)$ resonance is present in the $\bar{p}\,p \rightarrow \xi \rightarrow K_sK_s$ reaction, a very definite structure in the total cross section as function of energy should be seen. The structure of a pure Breit-Wigner resonance has the typical Lorentzian shape on top of an uncorrelated background. When the background process interferes coherently with the resonance, the Breit-Wigner shape is replaced by a more complex and general formula in which a cusp pattern is possible. Because there is a hint of a structure in the cross section, as seen in Fig.V.A.1, both resonance patterns are considered. In the first section, the parameters of both resonance types are defined. In the second section, a fit to the data is performed and an upper limit of the product of the branching ratios $BR(\bar{p}p\rightarrow\xi).BR(\xi\rightarrow K_sK_s)$ is estimated. Finally, in the last two sections, an interpretation of the results as well as a conclusion is given.

VI.A. Resonance Definitions.

A pure Breit-Wigner resonance is parametrized according to the following formula

$$\sigma_{total}(E) = \sigma_{B\text{-}W}(E) = \sigma_{non\text{-}back} + \sigma_{peak}\frac{\Gamma^2/4}{(E-E_R)^2+\Gamma^2/4}$$

where the four resonance parameters are the width (Γ), energy (E_R), strength (σ_{peak}), and the non-interacting background ($\sigma_{non\text{-}back}$) , see Fig.VI.A.1.

The resonance strength is proportional to the branching ratio product of the reaction

$$\sigma_{peak} = \frac{4\pi.(\hbar c)^2}{p_{CM}^2}\;\frac{(2J+1)}{(2s_{\bar{p}}+1).(2s_p+1)}\;BR(\bar{p}p\rightarrow\xi).BR(\xi\rightarrow K_sK_s)$$

where J is the spin of the resonance, p_{CM} is the center of mass momentum of the antiproton and $s_{\bar{p}}$ and s_p are the spins of the proton and antiproton.

When the background interacts coherently with the resonance, σ_{total} becomes

$$\sigma_{total}(E) = \frac{4\pi.(\hbar c)^2}{p_{CM}^2}\;\frac{(2J+1)}{(2s_{\bar{p}}+1).(2s_p+1)}\;\left|\frac{\sqrt{\Gamma_i/2}.\sqrt{\Gamma_f/2}}{(E - E_R) - i\,\Gamma/2} + \rho e^{i\theta b}\right|^2$$

where $\Gamma_i = BR(\bar{p}p\rightarrow\xi).\Gamma$ and $\Gamma_f = BR(\xi\rightarrow K_sK_s).\Gamma$ are the partial decay widths and the background, $\rho e^{i\theta b}$, is added to the Breit-Wigner amplitude as a complex number constant. With $\Delta\theta$ defined as $\theta_b - \pi$ and σ_{back} as the "coherent" background cross section, we obtain

$$\sigma_{total}(E) = \sigma_{B\text{-}W}(E) + \sigma_{back} - 2\sqrt{\sigma_{peak}}\sqrt{\sigma_{back}}\,\frac{\Gamma^2/4}{(E-E_R)^2+\Gamma^2/4}\left(\left(\frac{E-E_R}{\Gamma/2}\right)\cos\Delta\theta_b + \sin\Delta\theta_b\right)$$

An example of this formula at four phase angle differences, $\Delta\theta_b$, is shown in Fig.VI.A.2. The resonance is a pure Breit-Wigner type at 0°. On the other hand, we obtain a sharp minimum at 180° while the two intermediate cases, 90° and 270°, show the typical cusp pattern.

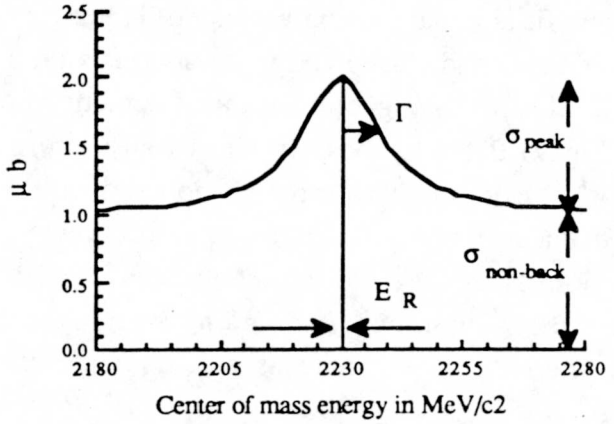

Fig.VI.A.1. Example of a pure Breit-Wigner resonance and its parameters.

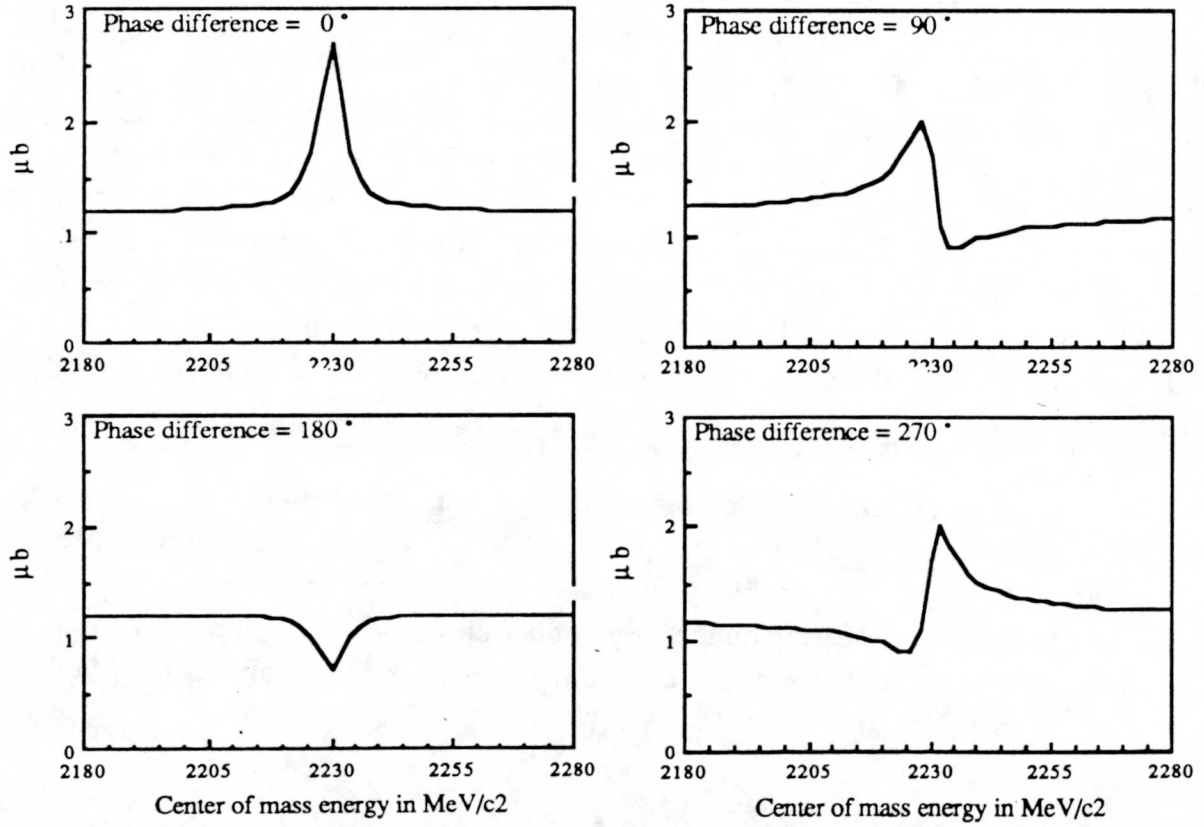

Fig.VI.A.2. Example of a Breit Wigner resonance interacting coherently with a background for four phase differences $\Delta\theta_b$. The resonance parameters are as follow : E_R=2230 MeV/c^2, Γ=6MeV/c^2, σ_{peak}= .5μb, σ_{back}=.5μb, $\sigma_{non\text{-}back}$=.7μb.

VI.B. Resonance Fits and Branching Ratio Determination.

A straight line fit to the total cross section is shown in Fig.VI.B.1a. It has a reduced χ^2 of 1.64. The fit is not extremely good and is an indication of non-negligible structure in the total cross section. The best fit to a pure Breit-Wigner resonance shape is shown in Fig.VI.B.1b. Because of the shape in the cross section data, a peak is found at 2238 MeV/c^2. The reduced χ^2 of this fit is equal to 1.63 and is not better than the χ^2 of the previous straight line fit. Appendix C and D shown the last two fits on a greater scale. Finally, the full six parameter fit of a Breit-Wigner resonance interacting coherently with the background is shown in Fig.VI.B.1c. It does not shown any improvement in the quality of the fit with a χ^2 of 1.73. Both the peak cross section and the width have large errors. It is interesting to note that a very good six parameter fit is obtained when both the 1403 and 1467 MeV/c low points are not considered (χ^2 =.75 with well defined parameters). In the last two fits, the χ^2 minimum is found by a grid search whose range and grid step size for each parameters are shown in the last column of the fit parameter table in Fig.VI.B.1b and Fig.VI.B.1c.

Only an upper limit on the resonance peak cross section and correspondingly the branching ratio product $BR(\bar{p}p\rightarrow\xi).BR(\xi\rightarrow K_sK_s)$ can be estimated. By requiring a 3σ effect or 99.7% confidence level that the production of the resonance is not seen, an upper limit is determined on the peak cross section of 2.3 μb at Γ=5 MeV/c^2 and 0.7 μb at Γ=30 MeV/c^2 for a pure Breit-Wigner. These numbers corresponds then to branching ratios of 1.4×10^{-4} and 4×10^{-5} for a J=2 resonance, as shown in Table.VI.C.1. The 3σ limit is obtained in the following way. For a fixed width Γ and peak cross section, a pure Breit-Wigner shape is minimized and the χ^2 calculated. The procedure is repeated for different values of σ_{peak} until a χ^2 of 35.4 (99.7% confidence level for 15 degrees of freedom) is found. The corresponding σ_{peak} defines the upper limit on the peak cross section and branching ratio product as discussed in section VI.A. No 3σ upper limit could be obtained from the six parameter fit.

Is the structure present in the cross section real or a statistical effect ? The structure does not depend on how the different backgrounds (tail and carbon) are subtracted, see section IV.D.1 and IV.D.2. A more likely possibility for systematic errors would be a run by run effect such as beam steering on the target or detectors not working properly. None of the seventeen measurements can be singled out as having these special effects, especially not the two low points at 1403 and 1471 MeV/c.

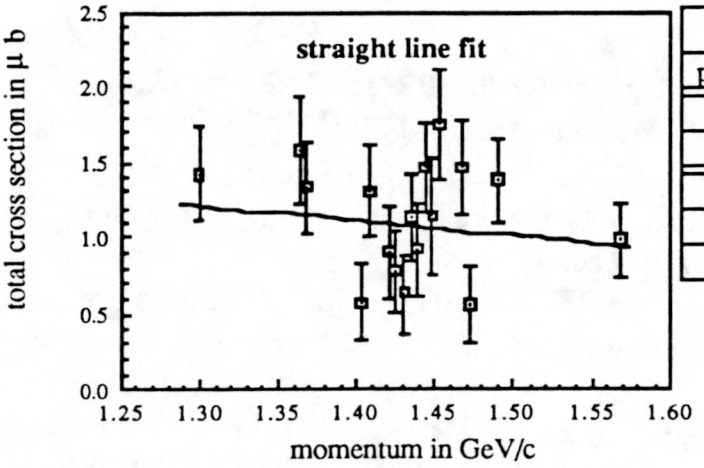

Fit parameters	
parameters	values
a	2.51 ± 1.74 μb
b	-0.99 ± 1.20 μb/MeV/c
χ^2 (unreduced)	24.54
χ^2 (reduced)	1.64
degrees of freedom	15

Fig.VI.B.1a. $\bar{p}\,p \rightarrow K_sK_s$ total cross section fitted with a straight line , $\sigma_{total}(p_{\bar{p}}) = a + b\,p_{\bar{p}}$.

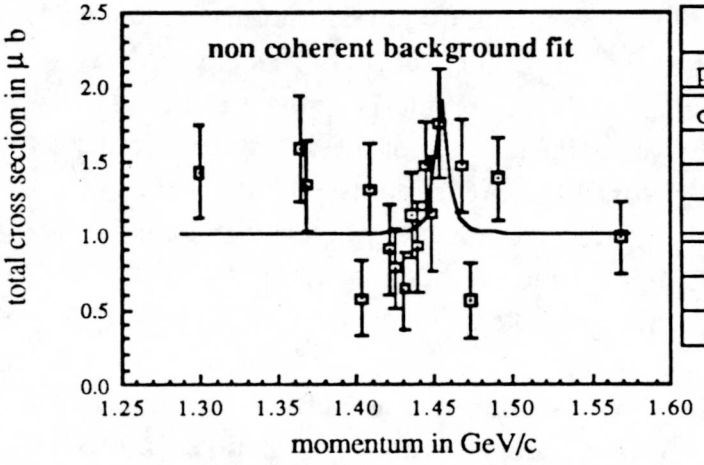

Fit parameters		
parameters	values	[range]/step size
$\sigma_{non\text{-}back}$	0.90 ± 0.21 μb	[0.60,1.20] /0.05
σ_{peak}	0.75 ± 1.20 μb	[0.50,1.00] /0.05
Γ	3 ± 7 MeV/c^2	[2,6] /1
E_R	2238 ± 5 MeV/c^2	[2225,2245] /1
χ^2 (unreduced)		21.20
χ^2 (reduced)		1.63
degrees of freedom		13

Fig.VI.B.1b. $\bar{p}\,p \rightarrow K_sK_s$ total cross section fitted with a pure Breit-Wigner resonance (non coherent background).

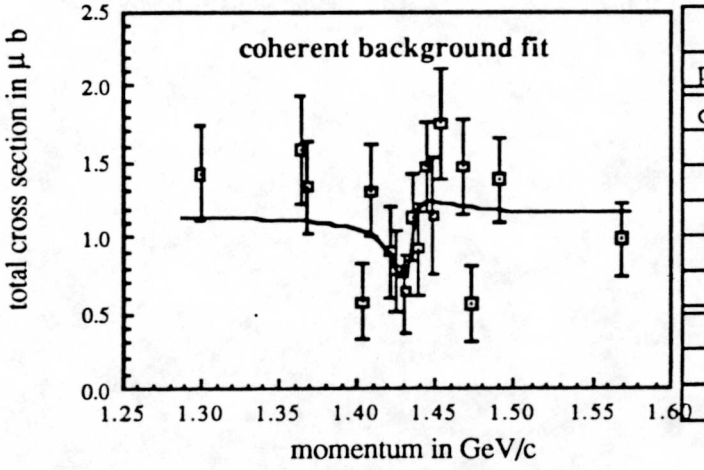

Fit parameters		
parameters	values	[range]/step size
$\sigma_{non\text{-}back}$	0.60 ± 0.24 μb	[0.40,1.00] /0.05
σ_{peak}	0.35 ± 1.45 μb	[0.20,0.60] /0.05
Γ	4 ± 19 MeV/c^2	[1,6] /1
E_R	2230 ± 5 MeV/c^2	[2225,2235] /1
σ_{back}	0.55 ± 0.26 μb	[0.20,0.60] /0.05
$\Delta\theta_b$	210 ± 47 °	[165,240] /15
χ^2 (unreduced)		19.08
χ^2 (reduced)		1.73
degrees of freedom		11

Fig.VI.B.1c. $\bar{p}\,p \rightarrow K_sK_s$ total cross section fitted with a Breit-Wigner resonance interacting coherently with background.

VI.C. Conclusion.

The upper limit obtained on the branching ratio product $BR(\bar{p}p \rightarrow \xi).BR(\xi \rightarrow K_S K_S) \sim 1 \times 10^{-4}$ is only slightly better than those obtained in the PS170[VI.SCULLY.87] and E789[VI.BARDIN.87] experiments, see table.VI.C.1. Even though the $\bar{p}p \rightarrow K_S K_S$ has a low non-resonant cross section, a better determination of the branching ratio product is not possible because of the structure in the total cross section.

In order to create the ξ resonance through the $\bar{p}p \rightarrow K_S K_S$ reaction, all quark pairs of the proton and antiproton must annihilate. The two most likely $\xi(2230)$ interpretations, the bound state $s\bar{s}$ meson and the glueball are shown schematically in Fig.VI.C.1a and Fig.VI.Cb. In the first case, a $s\bar{s}$ bound state and another $q\bar{q}$ pair are created to give the two decay kaons while in the second case, two $q\bar{q}$ pairs are directly created from the gluon bound states (glueball). Also, the normal $\bar{p}\,p \rightarrow K_S K_S$ background process is shown in Fig.VI.C.1c where only two quark pairs must annihilate. By using the Zweig (OZI) rule which suggests that disconnected quark-line diagrams are highly suppressed relative to the connected ones, we can expect that the last process, Fig.VI.C.1c, is not as suppressed as the first two diagrams. If the bound state meson diagram could be proven to be more suppressed than the glueball diagram or vice-versa, the absence of the ξ resonance in the $\bar{p}\,p \rightarrow K_S K_S$ channel could be used to favor the more suppressed interpretation. Unfortunately, no such statement can be readily made to differentiate these two possibilities and detailed calculations are necessary. The upper limit on the branching ratio obtained from this measurement is still consistent with these possible interpretations.

Even if the structure seen in the total cross section is a real effect, a resonance interacting coherently with the background is not the only possible explanation. A $\bar{\Lambda}\,\Lambda$ threshold effect is also possible if we remember that the $\bar{\Lambda}\,\Lambda$ channel opens exactly at 1435 MeV/c and that, at the threshold, both reaction cross sections are of the same order of magnitude. In both cases, a good determination of the differential cross section at each momentum point is essential.

Table.VI.C.1.

Branching Ratio Upper Limits (3 σ) at $M_\xi = 2230$ MeV/c^2 and J = 2				
Γ (MeV/c^2)	σ_{peak} (μb)	BR($\bar{p}p \to \xi$) .BR($\xi \to K^+K^-$)	BR($\bar{p}p \to \xi$) .BR($\xi \to K_SK_S$)	Experiment
7	4.4	3.8×10^{-4}	1.6×10^{-4}	E789/Brookhaven (VI.SCULLI.87)
35	1.9	1.8×10^{-4}	0.9×10^{-4}	
3	7.7	4.6×10^{-4}	2.3×10^{-4}	PS170/LEAR (VI.BARDIN.87)
30	2.1	1.3×10^{-4}	0.6×10^{-4}	
5	2.3		1.4×10^{-4}	THIS ANALYSIS
30	.7		0.4×10^{-4}	

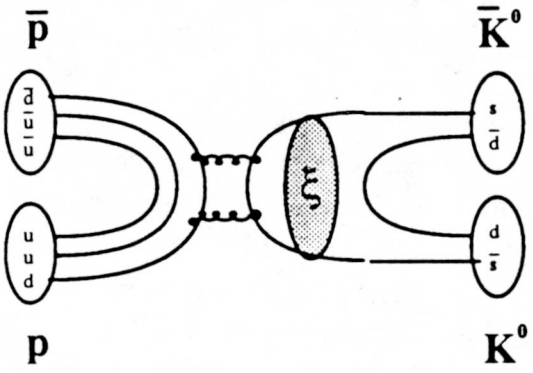

Fig.VI.C.1a. $\bar{p}p \to \xi \to \bar{K}K$ reaction. ξ resonance seen as a $s\bar{s}$ bound meson.

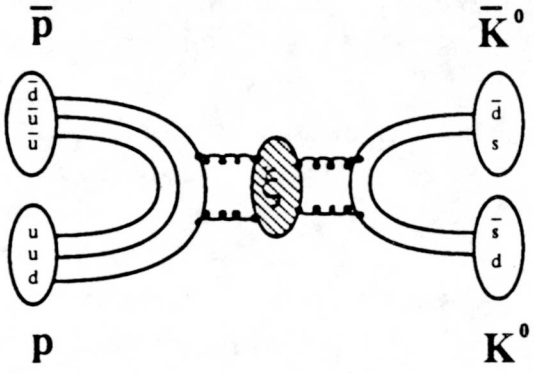

Fig.VI.C.1b. $\bar{p}p \to \xi \to \bar{K}K$ reaction. ξ resonance seen as a glueball state.

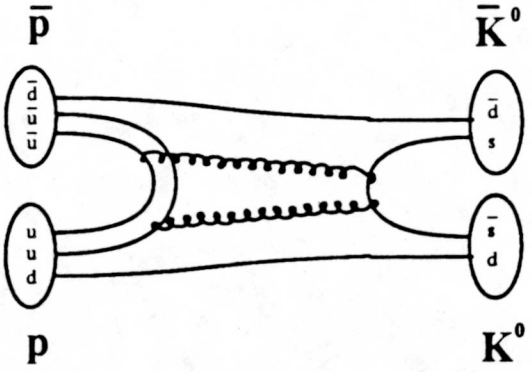

Fig.VI.C.1c. $\bar{p}p \to \bar{K}K$ non resonant background reaction or ξ resonance seen as a $q\bar{q}g$ hybrid state.

VII. Summary.

The $\bar{p}\,p \rightarrow K_S K_S$ reaction has been investigated by the experiment PS185 at LEAR to search for the $\xi(2230)$ resonance first seen in the K^+K^- and $K_S K_S$ channel of the radiative decay of the J/ψ by the MARK III collaboration at SLAC.

Unlike the $\bar{p}\,p \rightarrow \bar{\Lambda}\,\Lambda$ reaction, the $\bar{p}\,p \rightarrow K_S K_S$ reaction is not kinematically constrained in the forward direction. Therefore, the PS185 detector system, normally used to study the $\bar{p}\,p \rightarrow \bar{\Lambda}\,\Lambda$ reaction, was modified by adding twenty four Streamer Tube planes upstream of the current detector to increase the solid angle acceptance of the $\bar{p}\,p \rightarrow K_S K_S$ reaction.

Seventeen measurements in the antiproton momentum range of 1.30 GeV/c to 1.57 GeV/c were taken; most of these measurements centered around the mass of the $\xi(2230)$ resonance (antiproton momentum of 1.437 GeV/c). Of these seventeen measurements, eight were taken above the $\bar{\Lambda}\,\Lambda$ threshold and were also analysed for a $\bar{\Lambda}\,\Lambda$ final state.

Of the 36×10^6 events recorded, about 820 events were found to satisfy the required kinematical constraints of the $\bar{p}\,p \rightarrow K_S K_S$ reaction. In addition,about 10000 $\bar{\Lambda}\,\Lambda$ were found. These 820 events increased the "world" number of $K_S K_S$ events by a factor of ten and yielded an average total cross section of 1.05 ± 0.10 μb with a systematic error of 25%. The new "world" total cross section is shown in Fig.VII.1. The differential cross section has been measured for the first time with fairly large systematic uncertainties.

No conclusive evidence of the $\xi(2230)$ resonance has been found, although the total $\bar{p}\,p \rightarrow K_S K_S$ cross section shows some structure. An upper limit on the branching ratio product $BR(\bar{p}p \rightarrow \xi).BR(\xi \rightarrow K_S K_S)$ has been set to 1.4×10^{-4} and 4×10^{-5} for a resonance width of 5 and 35 MeV/c^2. These branching ratios are consistent with those obtained by the PS170 and E789 experiments which investigated the $\bar{p}\,p \rightarrow K^+K^-$ channel.

Because of low statistics and possible run by run systematic variations, the structure found in the total $\bar{p}\,p \rightarrow K_S K_S$ cross section could not be satisfactorily resolved, but is a hint for more beam time and more analysis.

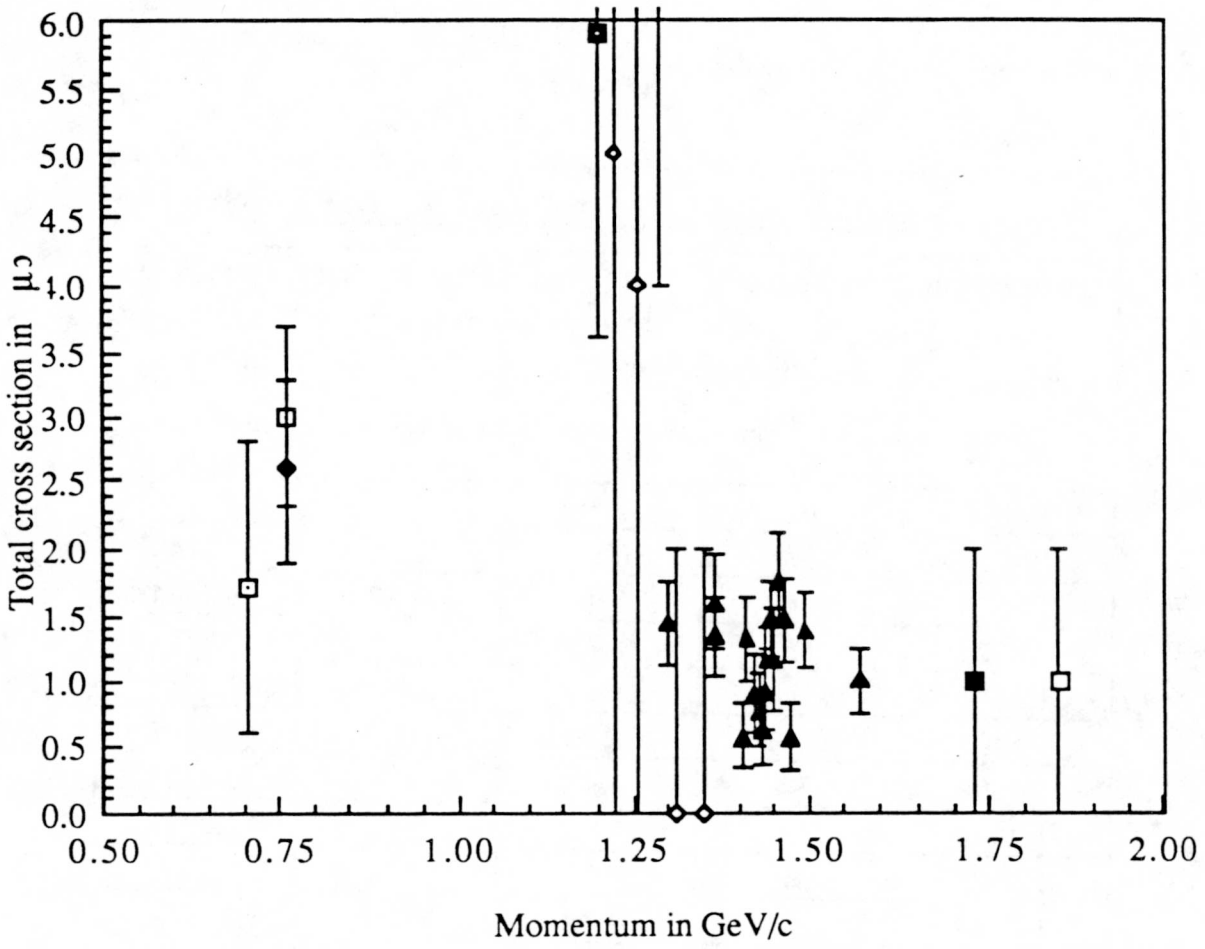

Fig.VII.1. New "world" $\bar{p}\,p \rightarrow K_s K_s$ total cross section. The cross section obtained by this analysis is shown with black triangles. The other measurements references are given in Fig.I.D.1.

Appendix A

$\bar{p}\,p \rightarrow K_S K_S$ Total Cross Section				
$\bar{p}$ momentum in GeV/c	Number of $K_S K_S$ analysed with $\chi^2 < 5$	Total cross section in μb	Error on total cross section in μb	$\bar{p}$ p center of mass energy in GeV/c^2
1.5674	60	0.99	0.24	2.2779
1.4899	66	1.38	0.28	2.2505
1.4715	30	0.56	0.26	2.2440
1.4670	56	1.46	0.32	2.2424
1.4525	55	1.75	0.36	2.2373
1.4480	27	1.15	0.38	2.2350
1.4438	64	1.46	0.29	2.2343
1.4393	34	0.92	0.30	2.2327
1.4348	53	1.13	0.28	2.2311
1.4303	31	0.63	0.26	2.2295
1.4249	37	0.78	0.27	2.2276
1.4204	33	0.90	0.31	2.2260
1.4075	51	1.31	0.31	2.2215
1.4030	31	0.58	0.25	2.2199
1.3685	54	1.34	0.30	2.2078
1.3640	48	1.58	0.36	2.2062
1.2996	53	1.42	0.31	2.1837

$\bar{p}\,p \rightarrow K_S K_S$ Differential Cross Sections						
	1500		1435		1360	
$\lvert\cos(\theta_{CM})\rvert$	Differential cross section in μb/sr	Error on differential cross secrion in μb/sr	Differential cross section in μb/sr	Error on differential cross secrion in μb/sr	Differential cross section in μb/sr	Error on differential cross secrion in μb/sr
0.05	0.115	0.041	0.140	0.036	0.122	0.041
0.15	0.305	0.069	0.208	0.048	0.121	0.047
0.25	0.274	0.099	0.160	0.070	0.140	0.079
0.35	0.174	0.078	0.116	0.060	0.223	0.084
0.45	0.351	0.083	0.234	0.059	0.235	0.070
0.55	0.156	0.055	0.249	0.055	0.209	0.061
0.65	0.078	0.042	0.139	0.041	0.210	0.056
0.75	0.003	0.035	0.057	0.035	0.070	0.043
0.85	0.069	0.031	0.102	0.029	0.208	0.043
0.95	0.189	0.054	0.209	0.047	0.167	0.052

$\bar{p}\,p \rightarrow K_S K_S$ Differential Cross Section all momenta			
$\lvert\cos(\theta_{CM})\rvert$	Differential cross section in μb	Statistical error in differential cross section in μb	Statistical and systematic error in differential cross section in μb
0.025	0.1250	0.0357	0.055
0.075	0.1227	0.0330	0.051
0.125	0.1854	0.0409	0.069
0.175	0.2542	0.0542	0.092
0.225	0.1890	0.0615	0.090
0.275	0.2467	0.1100	0.147
0.325	0.3035	0.0823	0.155
0.375	0.1242	0.0925	0.123
0.425	0.4305	0.0842	0.187
0.475	0.1593	0.0807	0.119
0.525	0.2737	0.0717	0.138
0.575	0.2572	0.0596	0.122
0.625	0.0034	0.1474	0.148
0.675	0.1702	0.0498	0.091
0.725	0.0616	0.0760	0.091
0.775	-0.0174	0.0550	0.059
0.825	0.1182	0.0440	0.072
0.875	0.2186	0.0497	0.102
0.925	-0.1318	0.2047	0.237
0.975	0.4057	0.1118	0.209

Appendix B

$\bar{p}\,p \rightarrow \bar{\Lambda}\,\Lambda$ Total Cross Section				
$\bar{p}$ momentum in GeV/c	$\bar{\Lambda}\,\Lambda$ analysed with $\chi^2 < 5$	Total cross section in μb	Error on total cross section in μb	Energy from threshold in MeV/c^2
1.56445	4982	35.10	0.51	46.69
1.48695	2111	20.09	0.44	19.32
1.46855	868	13.37	0.41	12.83
1.46405	841	11.19	0.40	11.24
1.44955	411	7.76	0.35	6.13
1.44505	176	5.80	0.36	4.55
1.44085	185	3.53	0.28	3.07
1.43635	25	0.97	0.27	1.48

$\bar{p}\,p \rightarrow \bar{\Lambda}\,\Lambda$ Total Cross Section at Threshold			
$\bar{p}$ momentum in GeV/c	$\bar{\Lambda}\,\Lambda$ analysed with $\chi^2 < 5$	Total cross section in μb	Error on total cross section in μb
1.44280	35	3.57	0.71
1.44200	44	4.49	0.81
1.44085	65	3.81	0.56
1.43935	41	2.25	0.41
1.43830	12	1.72	0.64
1.43750	9	1.72	0.81
1.43635	4	0.46	0.35
1.43485	0	0.00	0.34

$\bar{p}\,p \rightarrow \bar{\Lambda}\,\Lambda$ Total Cross Section at Threshold (previous measurements)			
$\bar{p}$ momentum in GeV/c	Total cross section in μb	Error on total cross section in μb	References
1.4356	0.84	0.20	V.FRANKENBERG.88
1.4370	1.44	0.32	V.FRANKENBERG.88
1.4454	4.86	0.42	V.FRANKENBERG.88
1.4765	13.77	0.50	V.MAHER.86
1.5000	24.6	5.9	V.JAYET.78
1.5075	26.6	0.7	V.MAHER.86
1.5100	58	14	V.OH.73
1.5460	44.6	0.7	V.DUTTY.88
1.5600	58.3	8.4	V.JAYET.78
1.6100	57	18	V.XUONG.62
1.6500	108	17	V.OH.73
1.6900	81	10	V.JAYET.78

Blank Page

Appendix C

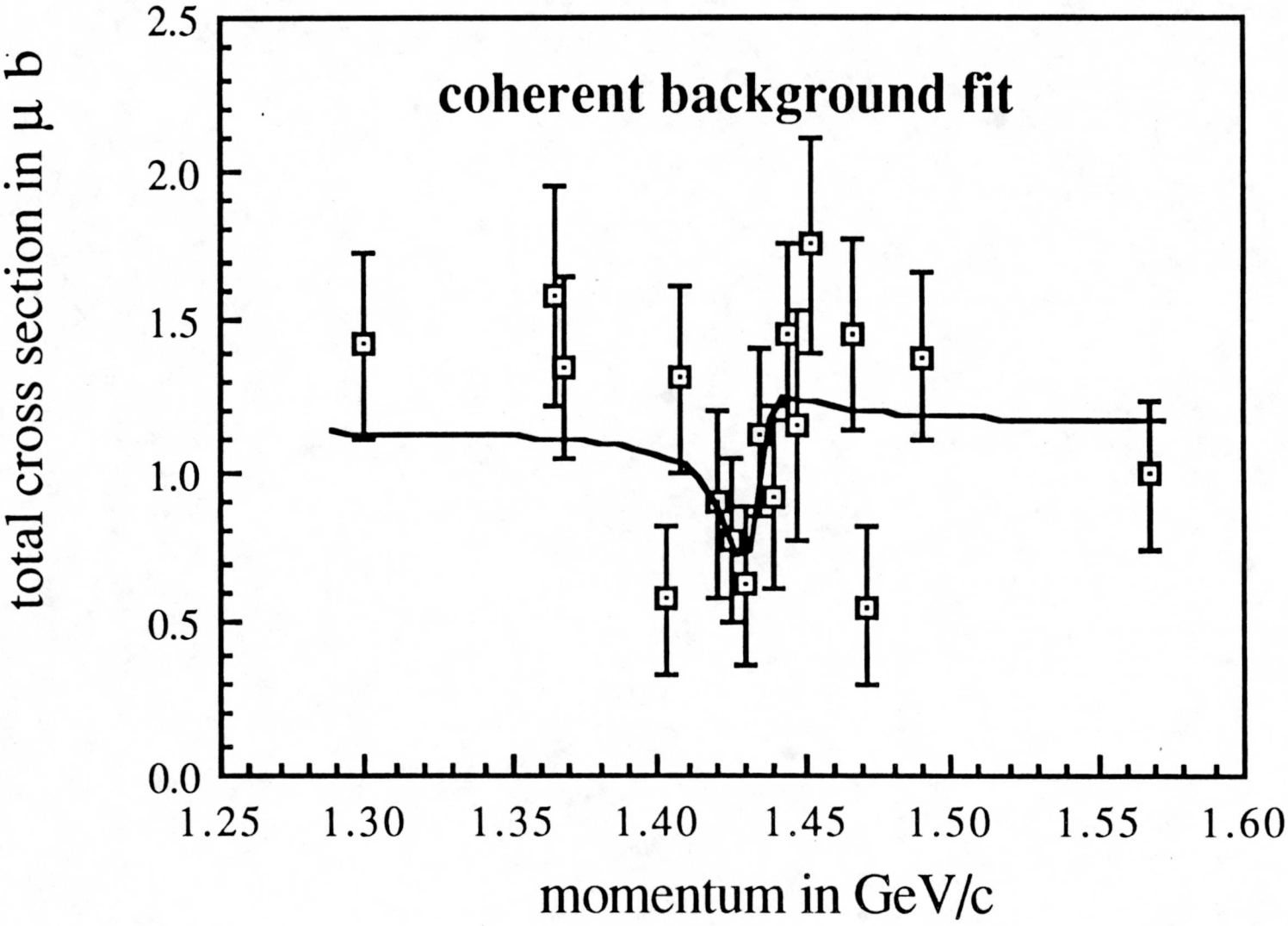
coherent background fit
total cross section in μ b
momentum in GeV/c
2.5
2.0
1.5
1.0
0.5
0.0
1.25
1.30
1.35
1.40
1.45
1.50
1.55
1.60

Blank Page

Appendix D

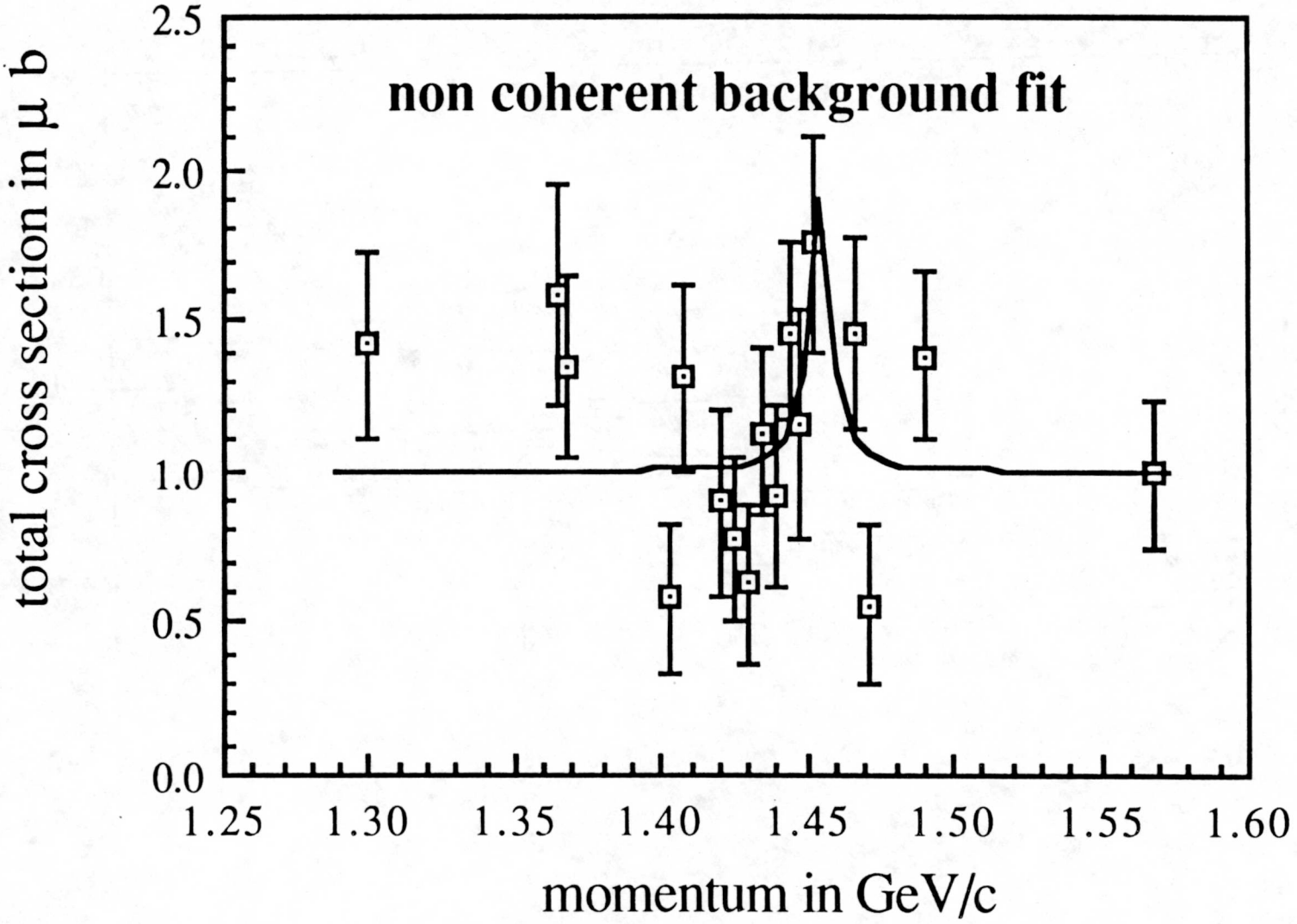
non coherent background fit
total cross section in μ b
momentum in GeV/c
2.5
2.0
1.5
1.0
0.5
0.0
1.25
1.30
1.35
1.40
1.45
1.50
1.55
1.60

Appendix E

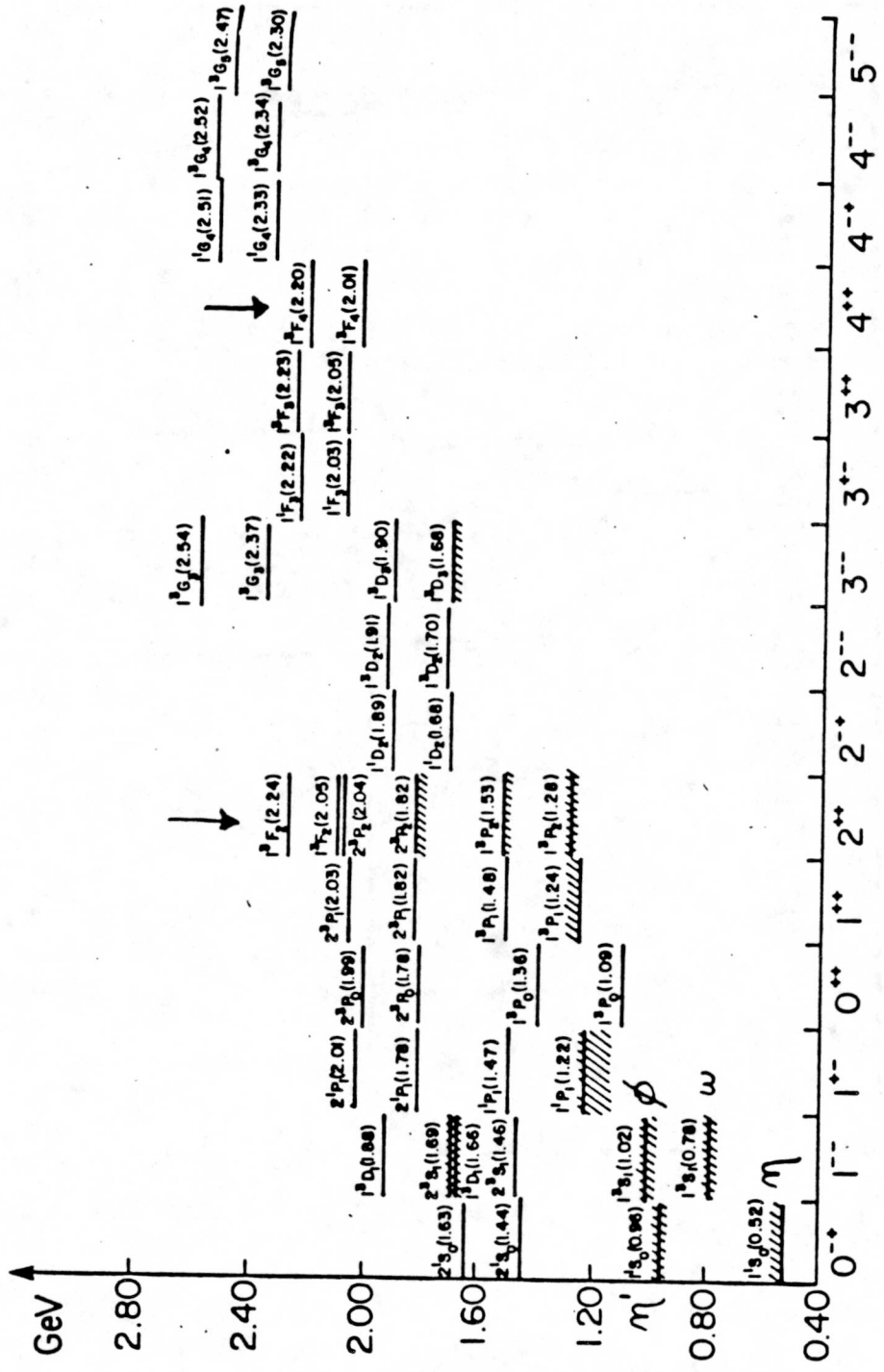

Isoscalar mesons (mainly $u\bar{u}$, $d\bar{d}$, $s\bar{s}$) calculated in a unified quark model with chromodynamics (one gluon exchange plus linear confinement potential plus relativistic effect) (I.GODFREY.85). The dominant spectral composition and predicted masses of states in GeV are shown near solid bars representing their masses. Shaded areas correspond to the experimental masses and their uncertainties, taken from the Particle Data Group (1984). The $\xi(2230)$ possible candidates are the $1^3F_2(2.24)$ and $1^3F_4(2.20)$ states.

Appendix F

Data Analysis and Computing.

The results obtained in this thesis required a very extensive data processing effort and could only be efficiently done on the CRAY X-MP/48 and Cray Y-MP/832 of the Pittsburgh Supercomputing Center. To that purpose, 180 Cray hours were necessary to complete the major part of this analysis (except for the first reduction which was done on the CERN IBM). Besides its "crunching" power, the CRAY supercomputer provided a fast "analysis" response especially in the final part of the analysis where kinematic cuts had to be refined.

In order to use the CRAY computer with a maximum of efficiency, a completely new analysis program (standard FORTRAN 77) had to be written which had to be fully compatible with the CRAY and VAX system. The machine specific decoding part of the analysis had to be taylored to the CRAY 64 bit machine. An important gain in speed for both the VAX and CRAY computers was obtained by rewriting the kinematic fitting algorithm so that the χ^2 minimization was not done numerically but analytically. This program was developed and tested on our μVAX II and μVAX III workstations and then implemented on the CRAY supercomputer.

The most time consuming part of the analysis is the kinematic fitting where a 13 by 13 matrix must be inverted on average ten to fifteen times for each vertex combination. By taking advantage of the vectorized CRAY specific matrix inversion subroutines, a speed up factor of 80 with respect to the μVAX III was obtained in this part of the analysis.

A greater speed up could be obtained if the presently essentially scalar (sequential) tracking and kinematic fitting algorithms could be replaced by completely new algorithms which take fully advantage of the parallelization possible on these supercomputers. This is not only true to this anlysis but to particle physics in general where the increasing amount of data available requires an even greater processing effort.

References

Chapter I

I.ALDE.86	D. Alde et al., Phys. Lett. **177B** (1986) 120.
I.ASTON.87	D. Aston et al., Nucl. Phys. **B103** (1988) 525.
I.AUGUSTIN.88	J.E. Augustin et al., Phys. Rev.Lett. **60** (1988) 2238.
I.BALTRUSA.86	R.M. Baltrusaitis et al., Phys. Rev.Lett. **56** (1986) 107.
I.BARDIN.87	G. Bardin et al.,Phys. Lett. **195B** (1987) 292.
I.BARLOW.67	J. Barlow et al., Nuovo Cimento **50A** (1967) 701.
I.BARNES.87A	P.D.Barnes et al., Phys. Lett. **189B** (1987) 249.
I.BARNES.87B	P.D.Barnes et al., Phys. Lett. **199B** (1987) 147.
I.BEHRENDS.84	S. Behrends et al., Phys. Lett. **137B** (1984) 277.
I.BOLONKIN.87	B.V.Bolonkin et al., Sov. J. Nucl. Phys. **46** (3) (1987) 451..
I.CHANOWITZ.83	M.S. Chanowitz and S.R.Sharpe, Phys. Lett. **132B** (1983) 413.
I.CHAO.88	K.T.Chao, Phys. Rev. Lett. **60** (1988) 2579.
I.CHAPMAN.72	Chapman, Nucl. Phys. **B42** (1972) 1.
I.COOPER.78	Cooper, Nucl. Phys. **B136** (1978) 365.
I.DOVER.84	C.B. Dover, P.M. Fishbane, Nucl. Phys. **B244** (1984) 349.
I.DUTTY.88	W. Dutty, Thesis, Freiburg 1988.
I.FRANKENBERG.87	R. v. Frankenberg, Thesis, Erlangen 1987.
I.GANGULI.81	Ganguli, Nucl. Phys. **B183** (1981) 295.
I.GIRIJA.86	V. Girija, F. Tabakin, Phys. Rev. **C34** (1986) 1798.
I.GODFREY.84	S. Godfrey, R. Kokoski, N. Isgur, Phys. Lett. **141B** (1984) 439.
I.GODFREY.85	S. Godfrey, N. Isgur, Phys. Rev. **D32** (1985) 189.
I.GREEN.84	A. M. Green, J. A. Niskanen, S. Wycech, Phys. Lett.**139B** (1984) 15.
I.HABER.84	H. Haber, G. L. Kane, Phys. Lett. **135** (1984) 196.
I.HANDLER.76	Handler, Nucl. Phys. **B110** (1976) 173.
I.HENLEY.86	E. M. Henley, T. Oka, J. Vergados, Phys. Lett. **166B** (1986) 274.
I.KOHNO.85	M. Kohno, W. Weise, Phys. Lett. **152B** (1985) 303.
I.KOHNO.86	M. Kohno, W. Weise, Nucl. Phys. , **A454** (1986) 429.
I.MAHER.87	C. Maher, Thesis CMU 1986.
I.MARUYAMA.87	M. Maruyama, S. Furui, A. Faessler, Nucl. Phys. **A472** (1987) 643.
I.MOUSSALAM.83	B. Moussalam, Nucl. Phys. **A407** (1983) 413.
I.NISKANEN.85	J. Niskanen, F. Myhrer, Phys. Lett. **157B** (1985) 247.

I.OH.73	Oh, Nucl. Phys. **B51** (1973) 57.
I.ONO.87	S. Ono, Phys. Rev. **D35** (1987) 944.
I.PAKVASA.84	S. Pakvasa, M. Suzuki, S. F. Tuan, Phys. Lett. **145B** (1984) 135.
I.RUBINSTEIN.66	H. Rubinstein, H. Stern, Phys. Lett. **21** (1966) 447.
I.SCULLI.87	J. Sculli et al., Phys. Rev. Lett. **58** (1987) 1715.
I.SHATZ.84	M. P. Shatz, Phys. Lett. **138** (1984) 209.
I.WARD.85	B. Ward, Phys. Rev. **D31** (1985) 2849.
I.WEINBERG.76	S. Weinberg, Phys. Rev. Lett., **19** (1967) 1264.
I.WILLEY.84	R. Willey, Phys. Rev. Lett. , **52** (1984) 585.
Chapter II	
II.BATTISTONI.80	G. Battistoni et al, Nucl. Inst. and Meth. **176** (1980) 297.
II.BATTISTONI.83	G. Battistoni et al, Nucl. Inst. and Meth. **217** (1983) 433.
II.DEWULF.86	J. P. DeWulf, Nucl. Inst. and Meth. **A252** (1986) 443.
II.MAHER.87	C. Maher, Thesis CMU 1986.
II.FRANKENBERG.88	R. v. Frankenberg, Thesis, Erlangen 1987.
II.ULMER.87	H. Ulmer, Diplomarbeit Freiburg 1987.
Chapter III	
III.DUTTY.88	W. Dutty, Thesis, Freiburg 1988.
Chapter IV	
IV.STINZIG.88	F. Stinzig, internal report 1988.
Chapter V	
V.JAYET.78	Jayet, Nuovo Cimento, **45A** (1978) 371.
V.OH.73	Oh, Nucl. Phys. , **B51** (1973) 57.
V.XUONG.62	Xuong, Phys. Rev. **128** (1962) 1849.
V.MAHER.87	C. Maher, Thesis CMU 1986.
V.DUTTY.88	W. Dutty, Thesis, Freiburg 1988.
V.FRANKENBERG.88	R.v. Frankenberg, Thesis, Erlangen 1987.
Chapter VI	
VI.BARDIN.87	G. Bardin et al.,Phys. Lett. **195B** (1987) 292.
VI.SCULLI.87	J. Sculli et al., Phys. Rev. Lett. **58** (1987) 1715.

Acknowledgements

I am grateful to Professor Peter Barnes who as my thesis adviser provided insight, encouragements, and made our interaction both pleasant and professional.

I would also like to thank

Gregg Frankin, Brian Quinn, Chris Maher, Reinhard Schumacher, Val Zeps, Marty Rozon, and Guy Diebold of the CMU Medium Energy Group for their support and useful discussions.

Chris Maher for his help in dealing with the Pittsburgh Supercomputing Center.

Dave Hertzog who made this measurement possible.

John Szymanski for his companionship during the course of our graduate studies.

Heiko Schledermann for his friendship and his help in developing the analysis code.

The PS185 collaboration for their team work.

My wife whose shared these times of ordeal with impatience.

Schlumberger Laboratories who by offering me a position certainly greatly shortened the length of my graduate studies.